

ABSTRACT

Lappeenranta University of Technology
LUT School of Energy Systems
Degree Programme in Energy Technology

Joni Paulasalo

CFD Modelling of Industrial Scale Gas Flame with OpenFOAM software

Master's Thesis

2019

98 pages, 53 figures, 22 tables and 3 appendices

Examiners: Professor, D.Sc.(Tech.) Timo Hyppänen
 D.Sc.(Tech.) Markku Nikku

Keywords: combustion, process furnace, CFD modelling, OpenFOAM

In this Master's Thesis OpenFOAM software was used to perform CFD modelling of an industrial scale gas fired process furnace. Goal was to evaluate the performance of open source tool OpenFOAM in modelling non-premixed turbulent combustion and compare the results with commercial tool ANSYS Fluent and available experimental data.

Selection of combustion simulation methods in OpenFOAM was done based on literature sources and a small scale validation case was used to evaluate the performance of different combustion and radiation models by comparing results to measurements prior to the actual process furnace simulations. Combustion solver reactingFoam was used with realizable $k - \epsilon$ turbulence model, EDC combustion model and P1 radiation model to simulate combustion inside the process furnace.

This work demonstrates that combustion models available in OpenFOAM can be used to model gaseous combustion in large-scale process furnace. Some inaccuracies were observed with mass balance, conservation of O_2 at outlet, temperature level inside the domain and heat transfer to the tubes. Mass imbalance and O_2 conservation were investigated with two different cases where air inlet boundary conditions were adjusted. Issues related to temperature and heat transfer were caused by the radiation model P1.

ACKNOWLEDGEMENTS

I want to thank Neste Engineering Solutions Oy for this opportunity to work and learn more about CFD modelling for industrial purposes. I am grateful for the support and teachings from the members of the Flow Dynamics team during my time in the company. Special thanks to D.Sc. Johanna Vaittinen for offering me this work and D.Sc. Emmanuel Ory for technical support with OpenFOAM.

I want to also thank Professor D.Sc. Timo Hyppänen and D.Sc. Markku Nikku for their instructions and comments to my work that guided me forward.

TABLE OF CONTENTS

NOMENCLATURE	7
1 INTRODUCTION	11
2 COMBUSTION MODELLING OF PROCESS FURNACE	13
2.1 Combustion	13
2.2 Fuel types	15
2.3 Gas combustion	16
2.3.1 Flame types	16
2.3.2 Burner types	18
2.4 Mathematical modelling	20
2.5 Computational Fluid Dynamics (CFD)	20
2.6 Process furnace	23
2.6.1 Basic function and structure	23
2.6.2 Operational risks	25
2.6.3 CFD modelling of process furnaces	25
3 COMBUSTION MODELLING IN OPENFOAM	26
3.1 Current combustion models in OpenFOAM	26
3.2 Conservation equations for laminar reacting flow	27
3.3 Turbulence modelling	30
3.3.1 Standard $k - \epsilon$ turbulence model	31
3.3.2 Realizable $k - \epsilon$ turbulence model	32
3.4 Reaction modelling	33
3.4.1 Eddy Dissipation Model (EDM)	33
3.4.2 Eddy Dissipation Concept (EDC)	34
3.4.3 Partially Stirred Reactor (PaSR)	35
3.5 Radiation modelling	36
3.5.1 P1	37
3.5.2 Discrete Ordinates Method (DOM)	37
3.6 Literature study about OpenFOAM combustion studies	38
3.7 Chosen sub-models for this work	40
4 CFD SIMULATIONS OF SANDIA FLAME D	42
4.1 Combustion model testing with Sandia Flame D	42
4.2 Sandia Flame D: Boundary conditions	44
4.3 Sandia Flame D: Simulations results	45
5 DESCRIPTION OF THE CFD MODEL FOR THE PROCESS FURNACE	57
5.1 Computational domain of the process furnace	57
5.2 Computational mesh of the furnace	59
5.3 Boundary conditions and used models in the furnace simulation	61
5.4 Running the simulation	63
5.5 Simulation cases	64
6 SIMULATION RESULTS	67
6.1 Base case simulation results	68

6.1.1	Convergence.....	68
6.1.2	Duration	72
6.1.3	Results.....	73
6.2	Comparison of detailed reaction scheme results.....	76
6.2.1	Convergence.....	76
6.2.2	Duration	79
6.2.3	Results.....	79
6.3	Simplified reaction scheme results.....	82
6.3.1	Convergence.....	83
6.3.2	Duration	85
6.3.3	Results.....	85
6.4	Comparison with Fluent results and measurements.....	87
6.4.1	Velocity field.....	89
6.4.2	Temperature field and heat transfer.....	90
6.4.3	Oxygen field.....	94
7	CONCLUSIONS	96
7.1	Mass balance.....	96
7.2	Flue gas composition and elemental balance.....	96
7.3	Flame size and shape	97
7.4	Heat duty and flue gas outlet temperature	97
7.5	Simulation duration	97
7.6	Recommendations	98
	REFERENCES	99
	Appendix I: Combustion studies with OpenFOAM in the literature	104
	Appendix II: Calculations of stoichiometric reactions	107
	Appendix III: Process furnace simulation results: Contour plots	108

NOMENCLATURE

Roman Letters

<i>A</i>	coefficient	-
<i>a</i>	reaction order	-
<i>B</i>	coefficient	-
<i>b</i>	reaction order	-
<i>C</i>	Courant number	-
	Coefficient	-
c_p	specific heat capacity	J/kgK
<i>D</i>	diffusion coefficient	m ² /s
<i>D</i>	hydraulic mean depth	m
E_a	activation energy	J/mol
Fr	Froude number	-
<i>g</i>	gravitational constant	9.81 m/s ²
<i>G</i>	incident radiation	W/m ²
<i>h</i>	specific enthalpy	J/kg
I_λ	spectral radiative intensity	W/mSr
<i>k</i>	reaction rate constant	1/s
<i>k</i>	thermal conductivity	W/mK
<i>k</i>	turbulent kinetic energy	m ² /s ²
<i>M</i>	molar mass	g/mol
<i>p</i>	pressure	Pa, atm
Pr	Prandtl number	-
<i>q</i>	heat flux	W/m ²
<i>r</i>	reaction rate	mol/L·s
<i>R</i>	universal gas constant	8.314 J/molK
<i>s</i>	direction	-
<i>S</i>	source term	J/m ³ s
Sc	Schimidt number	-
<i>T</i>	temperature	K, °C
<i>t</i>	time	s
<i>u</i>	velocity	m/s

w	weight factor	-
x	length	m
X	mole concentration	mol/L
Y	mass fraction	-
Z	mole concentration	mol/L

Greek Letters

α	elemental ratio	-
γ	mass fraction of fine structures	-
δ	Kronecker delta	-
ϵ	dissipation rate of turbulent energy	m^2/s^3
κ	absorption coefficient	1/m
κ	mass fraction of reacting cell region	-
λ	wavelength	m
μ	dynamic viscosity	Pa·s
ν	kinematic viscosity	m^2/s
	reaction stoichiometric coefficient	-
ρ	density	kg/m^3
σ	Stefan-Boltzmann constant	$5.67 \cdot 10^{-8} \text{ W}/\text{m}^2\text{K}^4$
τ	residence time	s
ω	reaction rate	1/s
Ω	solid angle	sr

Superscripts

"	Favre fluctuation
'	Reynolds fluctuation
*	fine structures
~	Favre average
-	Reynolds average
t	turbulent

Subscripts

a	activation
avg	average
b	blackbody

c	chemical
comb	combustion
eff	effective
i	Cartesian component
j	Cartesian component
k	Cartesian component
mix	mixing
p	constant pressure
P	products
R	reactants
rad	radiation
ref	reference
sens	sensible
s	specie
surf	surface
tot	total

Abbreviations

C_3H_8	propane
CFD	computational fluid dynamics
CH_4	methane
CO_2	carbon dioxide
DCS	distributed control system
EDC	eddy dissipation concept
EDM	eddy dissipation model
fvDOM	finite volume discrete ordinates method
FVM	finite volume method
H_2O	water
HHV	higher heating value
LES	Large Eddy Simulation
LHV	lower heating value
LTS	local time stepping
N_2	nitrogen
O_2	oxygen

PaSR	partially stirred reactor
PDE	partial differential equation
PIMPLE	combined PISO and SIMPLE
PISO	pressure implicit split operator
RANS	Reynolds-averaged-Navier-Stokes
RTE	radiative transfer equation
SD	standard deviation
SIMPLE	semi implicit method of pressure linked equations
TCI	turbulence-chemistry interaction
WSGGM	weighted sum of gray gases model

1 INTRODUCTION

Process furnaces are a crucial part of oil refining process. The furnaces combust the leftover gases from the refinery process to heat the process hydrocarbon streams. Heating of the hydrocarbon streams is necessary for the oil refining process: the hydrocarbon streams are fed to distillers and reactors, for example for reforming and cracking of hydrocarbons, and must therefore be heated to maximize yields of different hydrocarbon fractions produced in the process. Typical feed temperatures to distillation columns are in the range of 347–385 °C for atmospheric distillation and 400–413 °C for vacuum distillation (Hsu 2017, 545-546). Heating of the hydrocarbons into higher temperatures in process furnace tubes involves potential risks. Breakdown or malfunction of critical equipment in the furnace can have serious consequences due to combination of highly flammable hydrocarbons and high temperatures. Understanding the combustion and heat transfer inside the furnace is necessary for safe and optimized operation.

Computational Fluid Dynamics (CFD) can offer detailed information about the flow, the chemical reactions and the heat transfer within any process equipment. Combustion is a complex phenomenon that couples turbulent and compressible flow, and chemical reactions.

Commercial CFD software offer combustion modelling solutions that can be implemented relatively quickly and simulation results are likely to be obtained within a reasonable computational time. Commercial software are licensed for a limited amount of time and a limited number of computational cores. The use of a large number of cores helps to reduce the computational time of simulations. However, the cost of the licenses can significantly rise when trying to solve large industrial scale furnaces requiring large computational meshes in parallel, or the simulation time might become unbearably long. On the other hand, open source software can offer cost effective and modifiable tools without licensing costs. Open source software can be more difficult or laborious to operate and more unstable to run. Providing a thorough investigation of usable tools and understanding of the program, open source tools may offer similar simulation capabilities than commercial software with reduced operating costs.

The main objective of this work is to create a combustion model for a specific process furnace using an open source CFD modelling software OpenFOAM. The work will be based on a combustion solvers and files existing in OpenFOAM 6 tutorials. The CFD model should eventually be able to predict accurately enough

1. heat transfer from the flame to tubes
2. flame size and length
3. flue gas outlet temperature and O₂ concentration

within the given boundary conditions and scarce experimental data for validation. The same case has previously been modelled with the commercial software ANSYS Fluent 17.0, with which stability and quality of the results are also compared. Purpose is not to make direct comparison with Fluent results but to evaluate the capabilities of OpenFOAM for simulating a similar case of industrial scale combustion.

This thesis begins with an introduction to combustion (sections 2.1-2.3) and mathematical modelling (section 2.4). Process furnaces in oil refining are introduced in the following section. The third chapter will introduce OpenFOAM software and its available combustion modelling methods. A review of previous studies is presented section 3.6 in order to select suitable combustion model and sub-models for the current case. Validity of models will be tested with small scale validation case by comparing simulation results with measurements in the beginning of experimental part (chapter 4). The process furnace simulation case specific details are explained in chapter 5 by describing the computational domain, calculation mesh, boundary conditions, actions needed to complete the simulation and different simulation cases. Results are presented and discussed in chapter 6 and evaluated by comparing them to both the measurements and ANSYS Fluent simulation results. Results of the thesis are summed up in chapter 7 together with future recommendations.

2 COMBUSTION MODELLING OF PROCESS FURNACE

This chapter introduces the fundamentals of combustion in the process furnace and key CFD modelling aspects. The following aspects of combustion are covered in this chapter: general combustion process, different fuels and details of gaseous combustion with different flames and burners. The basics of mathematical modelling and its subcategory, CFD modelling, are explained. Finally, the basic function of the process furnace is explained and how CFD can be used to model the process furnace operation.

2.1 Combustion

Combustion is a term that is reserved for reactions that convert chemical energy to sensible energy. Formation of the sensible energy can be observed by higher temperature of the reaction products compared to the reactants. Combustion releases energy bounded in the chemical bonds of molecular specie and occurs when fuel and oxidizer meet at sufficiently high temperature. (Borman 1998, 3-4.) Fuel is a material that reacts with oxidizer, oxidizer is needed to react with fuel to form new product species and sufficient temperature is required to overcome the activation energy. Activation energy acts as a barrier between reactants and products that needs to be surpassed to bring reactants to reactive state (Borman 1998, 110).

A combustion reaction includes high temperatures, fast reactions and a visible sign of highly reactive region known as flame with gas combustion. These characteristics exclude slower oxidizing reactions such as rusting of metal and living cells producing energy from the combustion reaction definition. Also explosions are excluded from the combustion category since they have faster reaction speeds that create large pressure differences. (Borman 1998, 3-4.) An example of combustion reaction can be given with a simple reaction equation of methane combustion, where reactants are methane as fuel and oxygen as oxidizer. Products formed in the reaction are carbon dioxide and water. The reaction equation is written as



Reaction equation for methane oxidation is written as stoichiometric which means that theoretical amount of oxygen is considered to complete reaction perfectly. In a

stoichiometric reaction all of the reactants are converted to products. In reality, air is in most cases used to provide oxygen and with air there are also other species involved in combustion reactions other than oxygen (mainly nitrogen). Usually excess air is used to make sure that all of the fuel burns. This is called lean combustion and reaction with less than theoretical amount of oxygen is called rich combustion. (Borman 1998, 67-68.) Process furnaces with gas burners are usually operated in range of 15-25 % of excess air resulting in 2-5 % of excess oxygen (Treese 2015, 1606). However, balancing between NO_x emissions that tend to rise with higher excess air (up to a point where excess air flow is high enough to cool down the flame) and CO emissions that occur when supplied oxygen is not enough to complete the combustion results in excess air of 10-15 % with excess oxygen of 2-3 % (Treese 2015, 1235-1236). Usually fuels are also mixture of different species so reactions can occur with multiple species and different reaction paths. Multiple reaction equations are needed to describe the combustion in detail when reactions produce new species and consume others. (Borman 1998, 114-117.)

Heat released from combustion at constant pressure (open system) is calculated as change in enthalpy. Enthalpy change can be divided to sensible and chemical parts. Sensible enthalpy change accounts for temperature change of species and chemical enthalpy change for the chemical energy released from the species or energy bound to formation of specie. Enthalpy of the mixture can be calculated from individual properties of each specie. Heat from combustion can be calculated as

$$m[(h_2 - h_1)_{sens} + (h_2 - h_1)_c] = Q_p \quad (2.2)$$

where m is mass, h specific enthalpy and Q_p is the heat released at constant pressure. Subscripts *sens* and *c* refer to sensible and chemical respectively. (Borman 1998, 73.)

Most common way to estimate amount of energy release in combustion is with fuel heating value. Higher heating value (HHV) tells how much energy is released per unit in combustion when reaction begins and ends at state of 25 °C and 1 atm. The latent heat from condensation of water vapor is included in the HHV, because water condenses when reaction products are brought to 25 °C. Heat extracted between start and end of reaction is reaction heat. Lower heating value (LHV) assumes that water vapor is not condensed

after combustion (reaction products remain in higher temperature than in HHV). As names suggests, HHV is higher than LHV for same reaction. (Borman 1998, 28-29.)

2.2 Fuel types

Fuels used in combustion can be categorized as gaseous, liquid and solid.

- Gaseous fuels are for example natural gas and biogas. Natural gas can be found in natural reserves underground and biogas can be produced by heating wood or agricultural residues with less than stoichiometric amount of air. Gaseous fuels may contain different hydrocarbons species and also varying amounts of CO₂, N₂ and H₂O. (Borman 1998, 27-29.)
- Liquid fuels, such as gasoline and diesel, are refined mostly from crude oil but nowadays there are also biomass/waste based fuels available. Liquid fuels contain multiple different hydrocarbons with varying properties. Liquid fuels refined from crude oil are generally ash-free but heavier fractions contain minerals that increase ash content. (Borman 1998, 30.)
- Solid fuels are for example biomass, peat, coal and municipal solid waste. In addition to hydrocarbons, solid fuels contain varying amounts of ash, water, oxygen, nitrogen, sulfur and minerals. Wood and peat have high moisture contents lowering the combustion efficiency. (Borman 1998, 47-48.) Examples of common fuels and their properties have been listed in Table 2.1.

Table 2.1. Common fuel properties. (Moilanen et al. 1995, 105)

Fuel		Natural gas	Black coal	Peat	Wood
Lower heating value	(MJ/kg, dry)	49.2*	28.7	20.4	19.5
Moisture	(w-%)	0	10	40-55	30-45
Volatiles	(w-%, dry)	0	10	40-55	84-88
Ash	(w-%, dry)	0	14	4-7	0.4-0.5

*(Barrow 1998, 29)

Characteristics of the fuel and fuel type have major effect on the combustion reaction. Gaseous fuels contain minimal amounts of moisture and they are ready to mix and react with oxygen as they are injected to the combustion chamber. Liquid fuels are fed to the combustion chamber through an atomizer. The atomizer breaks the liquid into small

droplets and increases the overall surface area of the fuel. Small droplets vaporize more easily and vapor mixes with air. With high temperature source (high air temperature, existing flame or other source), mixture of air and vapor ignites. (Borman 1998, 289.) Solid fuels are usually crushed, chipped or pulverized to increase reactive surface area and homogenize the properties of fuel (such as particle shape and size). Combustion of solid fuels includes three stages: drying, pyrolysis and char combustion. Drying means evaporation of moisture in the solid fuel. Volatiles (volatile matter, light hydrocarbons that are released from the fuel in high temperature) start to be released from the fuel after the moisture is gone and solid fuels starts to decompose. As the volatiles travel towards the surface of the solid fuel they prevent the flow of oxygen into solid fuel. Oxygen-lean conditions at elevated temperature lead to pyrolysis of the solid fuel. Pyrolysis products are dependent on fuel type but common products are water, tars, carbon monoxide and dioxide with hydrocarbon vapor and liquids. (Borman 1998, 463-464.) After pyrolysis is complete, only char and ash remain in the solid fuel. Vaporization of the volatiles leaves char highly porous and oxygen can enter through diffusion into the solid particle surface. Char burns at the surface of the solid fuel until only ash remains. (Borman 1998, 468.)

2.3 Gas combustion

This thesis focuses on gas combustion in process furnace and this section shortly describes different flame types and burner equipment.

2.3.1 Flame types

Flames can be categorized as premixed and diffusion flames. Premixed flames have fuel and air mixed before combustion. Diffusion flames have separate air and fuel inlet streams that have to mix before combustion can occur. Both premixed and diffusion flames can be laminar or turbulent. Laminar flames have constant flame shape and lower burning velocity than turbulent flames. Turbulence increases the mixing and burning velocity which increases energy density of the flame. (Borman 1998, 145.)

Laminar premixed flame can be found in Bunsen burners, a common laboratory equipment, and laminar diffusion flame from candles. Turbulent flames are used in commercial applications to produce compact and efficient flames (Borman 1998, 145). Gas-fired furnaces can have both turbulent premixed and turbulent diffusion flames

depending on the burner type. International Flame Research Foundation (IFRF) has categorized flames into four different types, shown in Figure 2.1.

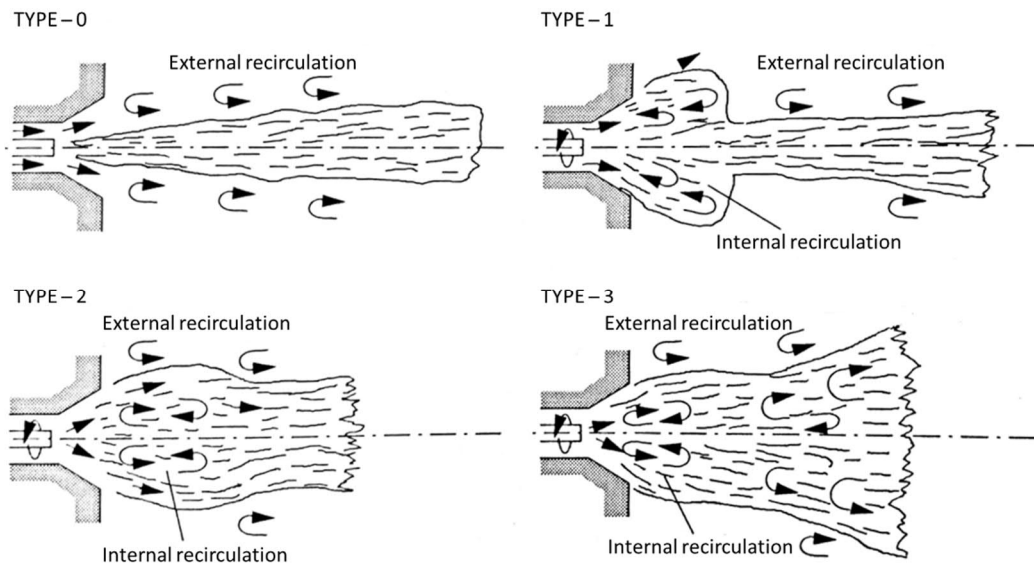


Figure 2.1. IFRF flame types. (Kjälldman 1995, 336.)

In Figure 2.1,

- Type – 0 flame represents a jet flame where air and fuel are injected axially without swirl at the inlet. Flow recirculates only at flame's external surface.
- Type – 1 flame is a jet flame where air and fuel are fed axially with swirl at inlet, which creates internal recirculation near the burner and helps to stabilize the flame. Swirl increases mixing and spreads flame radially. External recirculation occurs further away from the burner where fuel stream has penetrated the internal recirculation zone.
- Type – 2 flame uses a conical feed for fuel and swirling air flow to create short and intensive flame.
- Type – 3 flame is also as intensive as type – 2, but it is longer and has a second recirculation zone further away from the burner. Type – 3 flame needs strong swirl in narrow combustion chamber compared to the size of the flame. (Kjälldman 1995, 335-336.)

2.3.2 Burner types

A burner mixes combustion air and fuel and feeds them into a combustion chamber. The detailed burner design and location of burners in the furnace influence combustion stability, reliability, safety, efficiency and emissions. Burner types presented here are premixed burners with entrained air or pressurized air and nozzle-mixed burners. (Borman 1998, 204.)

Example of premixed with entrained air burner is shown in Figure 2.2. Premixed burners with entrained air (also known as atmospheric burners) do not use air blower to supply combustion air, instead low pressure and high velocity fuel stream draws the combustion air to venturi tubes. Venturi effect increases flow velocity and decreases pressure as flow area decreases. Air mixes with fuel as the tube cross sectional area increases and mixture moves to the burner nozzle. Burner nozzles release the mixture to the combustion chamber where combustion occurs. Secondary air is supplied at the burner nozzle where a mixture flow entrains more air to the flow. Flow velocity must be greater than burning velocity in order to prevent flashback, where the flame front moves inside the burner. (Borman 1998, 204-205, 208.)

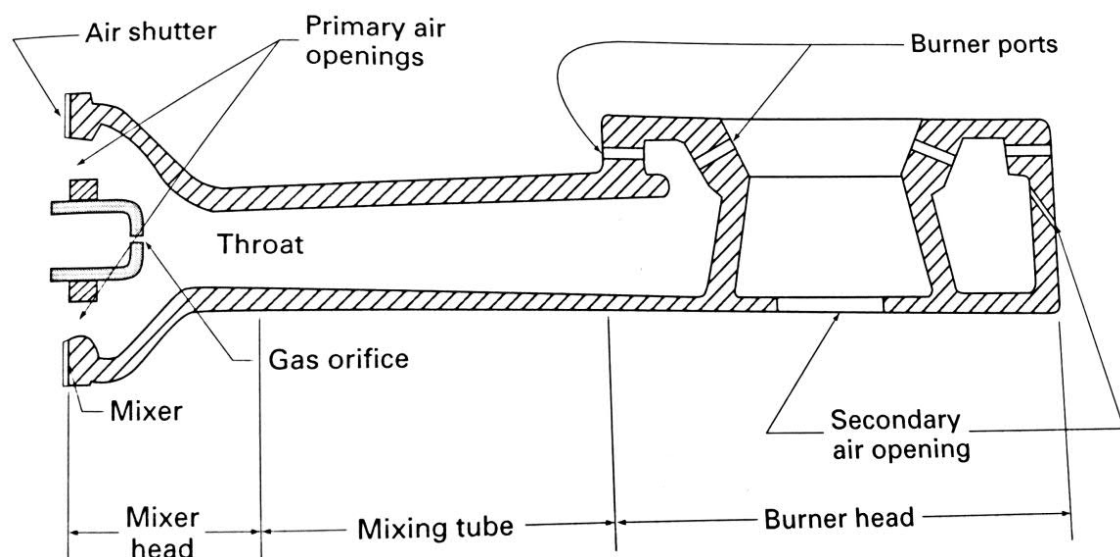


Figure 2.2. Premixed gas burner with entrained air. (Borman 1998, 207)

Premixed burners where both air and fuel are pressurized, can achieve higher energy density and better control of the flame. Higher flow rate can be achieved for air/fuel mixture but a too high velocity might lead to blow-off. In a blow-off, the mixture velocity

is greater than the burning velocity and the flame separates from the burner nozzle and might possibly be extinguished. To prevent possible flashbacks, pressurized air burner surfaces have to be cooled so that the mixture temperature does not rise too much and increase flame speed. Preheating of air is therefore impossible when considering the risks of flashback. (Borman 1998, 208.)

With larger scale applications it is possible to mix air and fuel outside the burner. Example of nozzle-mixed burner is shown in Figure 2.3. In Figure 2.3, fuel gas and air are fed in different channels and air feed is separated into primary and secondary air in the nozzle-mixed burner. Separation of flows eliminates risk of flashback. The air flow, primary or secondary, is led to a swirl motion so that the flame has swirl. Mixing (seen as recirculation in Figure 2.1) is important to reduce demand for excess air and preheating of combustion air can be done to increase the efficiency of the furnace. The furnace walls can be covered with refractory material that protects the metal structure from mechanical and thermal stresses. The refractory material is shaped as cone to guide the flow after the burner nozzle and maintain stability of the flame. (Borman 1998, 209.)

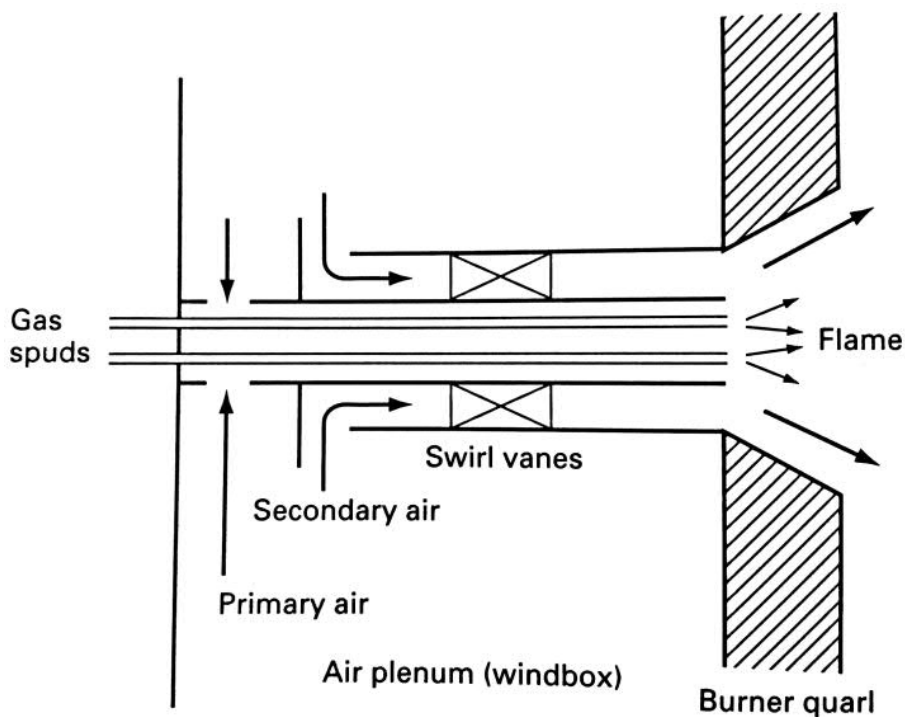


Figure 2.3. Nozzle-mix gas burner. (Borman 1998, 210)

2.4 Mathematical modelling

In this thesis, words “model” and “modelling” refer to mathematical models and mathematical modelling. Mathematical model aims to describe reality by means of mathematics. Mathematics offers a way to formulate problems and solutions in a precise manner. Language of mathematics is universal and gives possibility for modifications. Mathematical problems can be calculated with computers that can solve complex problems with high computational speed. (Bender 1978, 1)

Situations that require modeling are usually complex and to achieve results in timely manner approximations and neglecting unnecessary effects are often essential. The person responsible of the model creation needs to understand the governing phenomena. Several different models can be formulated to solve one problem. Each model can have different levels of complexity based on both the assumptions and the simplifications made. More general models are issued from further assumptions but can be applied to several different applications while more specific models are usually restricted for a narrower field of applications. (Bender 1978, 2-4)

Mathematical modelling can be done analytically and numerically. Analytical models aim to obtain exact solution for an equation or a set of equations. Sometimes, an equation does not have an exact solution or deriving an exact solution is difficult. Numerical models aim to approximate the solution with discretized equations. Discretization means dividing continuous functions into separate and discrete parts. Discretization includes always an error when changing continuous functions into discrete form. Errors need to be minimized in order to reach credible results. On the other hand, analytical solutions can be found for simple systems and geometries. When multiple different physical effects have to be considered with complex geometries, it is more efficient to use numerical methods. (Bender 1978, 140.)

2.5 Computational Fluid Dynamics (CFD)

Computational Fluid Dynamics aims to solve fluid (gas, liquid and particles) flows by numerical methods. Problem solving with CFD includes the following steps:

- Defining modelling objectives, which determine the model scope and complexity
- Collecting initial data about flow boundary conditions and system geometry
- Creating 3D or 2D geometry of the system under investigation
- Creating calculation mesh by dividing the geometry into small elements
- Setting up boundary conditions based on available data on the flow conditions
- Running simulations until convergence is reached
- Processing the results into format that is easy to understand (tables, figures and graphs)

Fundamentals of fluid flows can be described by partial differential equations (PDE), which express the conservation of mass, momentum and energy. Conservation equations are presented in section 3.2. PDEs are discretized into algebraic equations using numerical methods. In CFD, the Finite Volume Method (FVM) is widely used discretization method and it is also used in OpenFOAM. The FVM uses boundaries to create non-overlapping control volumes and divide the computational domain into calculation cells. The PDEs related to the simulation are solved in every cell. (Ferziger 1997, 67-71.) Example of control volume is shown in Figure 2.4.

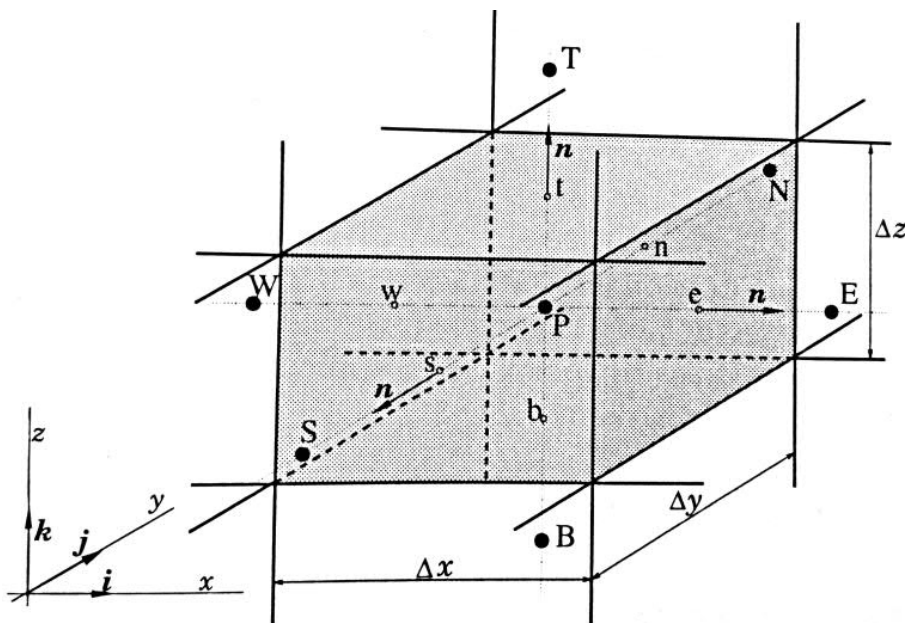


Figure 2.4. Example of control volume in Cartesian coordinate system. (Ferziger 1997, 69.)

In Figure 2.4, point P refers to center of the control volume. Uppercase letter of N, E, S, W, T and B refer to centers of surrounding control volumes in north, east, south, west, top and bottom respectively. Values at the boundaries, between the control volumes, are marked with same lowercase letters.

Terms in the PDEs are integrated over the boundary surface or over the whole control volume. Vector variables are evaluated as fluxes at control volume boundaries and scalar variables inside the boundaries over the control volume. Since values are stored inside the control volumes, values at the boundaries have to be interpolated. (Ferziger 1997, 67-71.)

Each variable has its own equation that needs to be solved in every control volume. Equations of one variable are gathered to a matrix, which can be solved by numerical methods. The PDE problem is solved by iterating the matrixes: starting from initial conditions for variables such as pressure, temperature etc. set at the beginning of the simulation calculations, then proceed with stepping forwards in space and time. Stepping forwards in space means going through the whole calculation domain and exchanging variable information between neighboring elements. If the simulation is transient, several iterations can be done during a single time step. Convergence is measured with residuals, which are calculated from sum of the terms in the solved algebraic equations. Residuals represent the error that exists in the solution of the algebraic equations. When residuals are small enough or they do not change, it can be said that system has reached convergence. Next time step can be calculated after previous time step has converged. (Ferziger 1997, 23)

Algorithms, needed to reach solution in such an iterative process, are complex and different depending on the physics of the model. Therefore CFD is commonly used with software packages which have ready-made solvers that can be used without need for major modifications. The solvers include problem specific method to solve a set of required PDEs. As a starting point for a simulation, computational mesh, initial and boundary conditions, variable properties and settings for simulation duration and accuracy are required. Results given by the solver needs to be post-processed to summarize the main findings from the simulation and to give an overview of the flow conditions. Post-processing includes calculation of important process variables (such as

temperature or specie concentration) at locations where they can be compared to measurements. Flow patterns are illustrated with figures to visualize the results and give background to the quantitative results.

2.6 Process furnace

Process furnaces are used to heat the hydrocarbons streams in oil refineries. Different refinery processes, such as distillation or cracking of the hydrocarbons, operate in high temperatures which require high temperature hydrocarbon inlet streams. Process furnaces are major energy consumers in the oil refineries and even small efficiency improvements can lead to significant savings. Efficiency in process furnaces means a portion of energy that is transferred from the chemical energy of the fuel gas to sensible heat of the hydrocarbon stream in the tubes. High tube surface (tube skin) temperatures with hydrocarbons involve potential high risk situations and therefore requires precise controls for safe operation.

2.6.1 Basic function and structure

In oil refining, process furnaces are used for heating hydrocarbons flowing in tubes usually located around the furnace walls. The main duty of the furnace is to heat hydrocarbon stream to desired temperature for other process equipment such as distillers and reactors. For example, temperature determines the pressure of vaporization which is critical for distillation process.

Figure 2.5 shows configuration example of a process furnace. Pressurized hydrocarbon stream flows inside the tubes and the tube surfaces are directly exposed to radiation and convection heat transfer from hot exhaust gases and flame.

The furnaces have two common forms;

- Long rectangular cabin heater with burners at floor
- Cylindrical heaters with one central burner in the base or ring of multiple burners.

The process furnaces in petrochemical industry differ from boilers used e.g. for power generation with larger and fewer tubes. (Mullinger 2014, 26-27.)

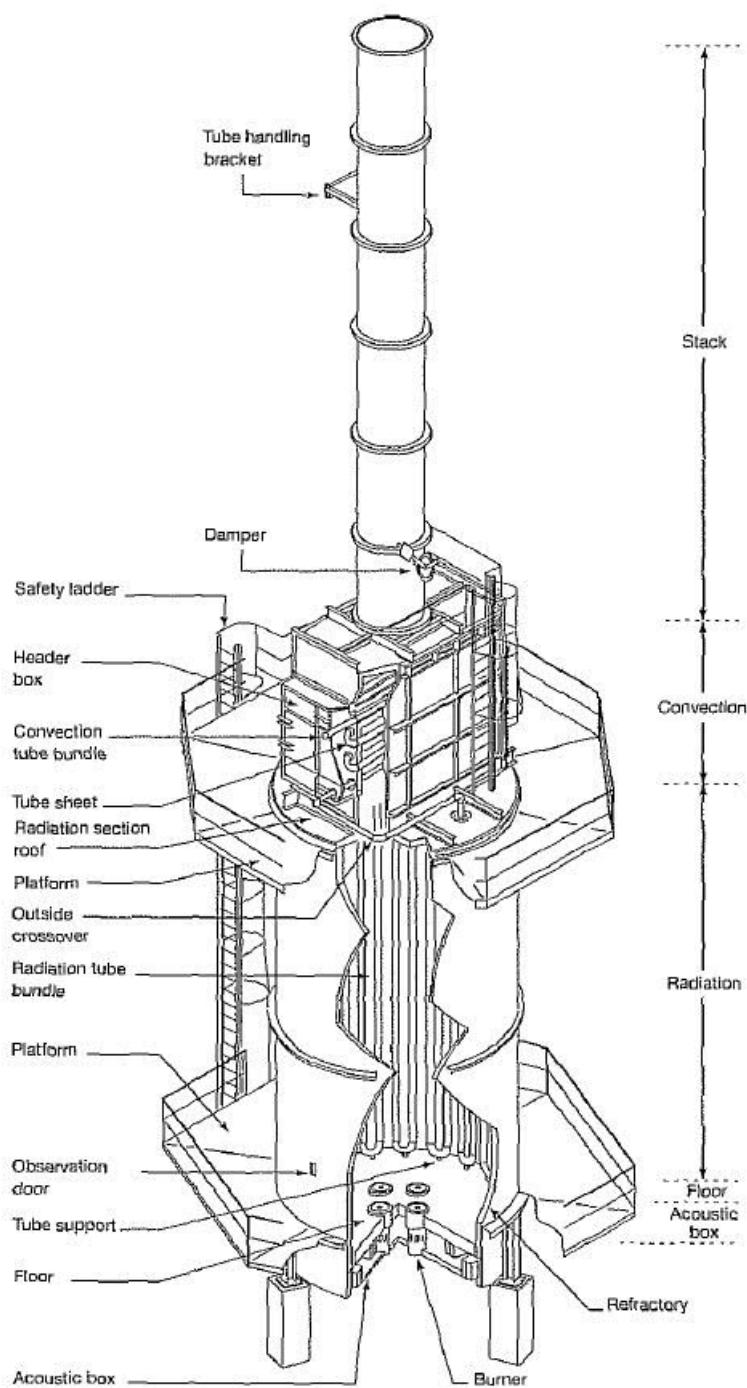


Figure 2.5. Example of vertical cylindrical process furnace (Trambouze 2000, 162).

As shown in Figure 2.5, burners are attached to the furnace floor. Flame from the burners radiate heat to the tube bundle in the radiation section of the furnace. Hot flue gases rise to the convection section to preheat the fluid in the tubes that lead to radiation section. The tube flow hence flows first through the convection part and then to the radiation part, out of which the flow is feed e.g. to a distillation column.

2.6.2 Operational risks

Heating of the fluids inside the tubes has to be precisely controlled. If the heat released from combustion is too high, the flame can create local hot spots on the tube surfaces. High tube skin temperatures lead to coke formation inside the tube. Coke layers decrease heat transfer from the tube to the fluid and increase pressure loss. These losses in the system need to be compensated with added fuel consumption and pumping power to achieve desired output conditions. When effectiveness of heat transfer falls, tube skin temperature can raise so much that the tube will break and leak the hydrocarbons inside the combustion chamber. This destroys the heater and will most likely lead to a catastrophic explosion that can cause major casualties. (Mullinger 2014, 27.)

2.6.3 CFD modelling of process furnaces

Common engineering methods with using simple mass/heat balances and correlations are suitable for general design of fired heaters. Critical factors such as tube skin temperatures or flame length are difficult or expensive to either continuously measure or estimate with traditional methods, such as 0D or 1D balance calculations.

Using available data from measurements in the process and design specifications CFD simulation can provide detailed information about flow structure, heat transfer and reaction phenomena inside process equipment. CFD is a tool to investigate performance of burners, distribution of heat rate on tube surfaces and flame shape, size and stability. CFD is a numerical method to gain insight to process equipment that cannot be achieved with conventional design tools. Once the model is completed and validated with measurements it can be used to test different constructions, components and operating conditions to find improvements to the system.

3 COMBUSTION MODELLING IN OPENFOAM

OpenFOAM refers to Open Source Field Operation and Manipulation. OpenFOAM is based on C++ programming language and the source code libraries hold approximately 250 applications which include the means for pre-processing, solving and post-processing of fluid dynamics problems. These applications are divided into solver and utilities. Solvers are built to solve certain problems in fluid and continuum mechanics. Utilities are designed to perform data manipulation tasks. (CFD Direct 2018.)

OpenFOAM offers multiple solvers for combustion, but only some of those are suitable for non-premixed combustion. Without any previous experience in combustion simulations with OpenFOAM it can be difficult to find suitable solver for desired case study. Therefore investigation about current models, their capabilities and use in other combustion studies was conducted and is presented in section 3.6. Literature research gives an overview of current state of combustion studies with OpenFOAM. Findings of the literature research guide the solver selection for this work and offer some insight to best practices in combustion modelling.

This chapter introduces governing equations of reacting flow for selected sub-models in section 3.2. Section 3.2 includes transport equations for continuity, momentum, energy and specie transport. Simulations are often ran for average quantities and there different averaging methods are described for transport equations.

Turbulence, reaction and radiation modelling have their own sections 3.3, 3.4 and 3.5 respectively. The sub-models discussed in the following section were selected based on the literature review in section 3.6 and those will be applied on the Sandia Flame D in chapter 4.1 to test their applicability and evaluate performance.

3.1 Current combustion models in OpenFOAM

In OpenFOAM version 6, ready-made solvers for non-premixed combustion are reactingFoam, rhoReactingFoam, rhoReactingBuoyantFoam and fireFoam. ReactingFoam solver is the base version of combustion solver with chemical reactions.

- RhoReactingFoam is based on reactingFoam solver but has density based thermodynamics package instead of pressure based.
- RhoReactingBuoyantFoam is based on rhoReactingFoam solver and has buoyancy effects enhanced by implementing gravity.
- FireFoam is combustion solver for non-premixed combustion.

Additional models exist for pyrolysis and Lagrangian sprays for fire suspension but those are not applicable in the current work. Several turbulence, combustion and radiation models are available for all of the solvers. (CFD Direct 2018.) These sub-models are explained in Sections 3.3-3.5.

3.2 Conservation equations for laminar reacting flow

Species are reacting during simulation and therefore fluid composition changes over time inside the domain. Reactions lead to formation and consumption of different species which causes changes in the mixture molecular mass. Pressure and temperature are also changing which cause the density variation with compressible gases. Continuity and momentum equations with varying density are defined as (Biswas 2002, 437-438) (Khadar 2015, 18-28)

$$\frac{\partial \rho}{\partial t} + \frac{\partial(\rho u_j)}{\partial x_j} = 0 \quad (3.1)$$

$$\frac{\partial(\rho u_i)}{\partial t} + \frac{\partial(\rho u_i u_j)}{\partial x_j} = \frac{\partial p}{\partial x_i} + \frac{\partial}{\partial x_j} \left[\mu \left(\frac{\partial u_i}{\partial x_j} + \frac{\partial u_j}{\partial x_i} - \frac{2}{3} \delta_{ij} \frac{\partial u_k}{\partial x_k} \right) \right] \quad (3.2)$$

where u_j is Cartesian velocity component, x_j is Cartesian direction, ρ is density, p is pressure, μ is dynamic viscosity and δ_{ij} is Kronecker delta. Density of mixture in reacting flows is determined as

$$\rho = \frac{p M_{avg}}{RT} \quad (3.3)$$

where $M_{avg} = \frac{1}{\sum_s \frac{Y_s}{M_s}}$ is average molar mass of the mixture, Y_s is mass fraction of chemical species, M_s is specie molar mass, R is universal gas constant and T is temperature.

Laminar dynamic viscosity is calculated based on Sutherland's law

$$\mu = A_s \frac{T^{\frac{3}{2}}}{T+T_s} \quad (3.4)$$

where A_s and T_s are constants of specie.

Reactions depend on temperature which requires computation of energy transport inside the domain. Temperature levels need to be known also for thermodynamic properties of different variables. Energy transport equation is defined as

$$\frac{\partial(\rho h)}{\partial t} + \frac{\partial(\rho h u_j)}{\partial x_j} = \frac{\partial}{\partial x_j} \left[\frac{\mu}{Pr_h} \frac{\partial h}{\partial x_j} + \mu \left(\frac{1}{Sc_s} - \frac{1}{Pr_h} \right) \sum_s h_s \frac{\partial Y_s}{\partial x_j} \right] + \frac{\partial p}{\partial t} + S_{rad} + S_{comb} \quad (3.5)$$

where Pr_h the Prandtl number of the mixture, Sc_s is the species Schmidt number, S_{rad} is the radiation source term and S_{comb} the combustion source term. Mixture enthalpy is defined as mass-weighted sum of species

$$h = \sum_s Y_s h_s \quad h_s = h_s^0 + \int_{T_0}^T c_{p,s}(T) dT \quad (3.6)$$

where $c_{p,s}$ is the specific heat capacity of specie s at constant pressure and temperature. h_s^0 is the formation enthalpy of specie s . The mixture Prandtl number is calculated as

$$Pr_h = \frac{\mu c_p}{k_c} \quad (3.7)$$

where k_c is the mixture average thermal conductivity. The species Schmidt number is calculated as

$$Sc_s = \frac{\mu}{\rho D_s} \quad (3.8)$$

where D_s is the diffusion coefficient of specie.

The temperature field is updated based on calculated enthalpy as follows

$$T = \frac{h - Y_{fuel} h_{fuel}}{\bar{c}_p} \quad (3.9)$$

$$\bar{c}_p = \frac{1}{T - T_{ref}} \int_{T_0}^T c_p dT \quad (3.10)$$

where h_{fuel} is the combustion enthalpy of the fuel.

Species transport is described by

$$\frac{\partial(\rho Y_s)}{\partial t} + \frac{\partial(\rho u_j Y_s)}{\partial x_j} = \frac{\partial}{\partial x_j} \left[\rho D_s \frac{\partial Y_s}{\partial x_j} \right] + \dot{\omega}_s \quad (3.11)$$

where $\dot{\omega}_s$ is reaction rate i.e. source term that includes production and consumption of the specie.

Simulations in this work are performed for averaged values of quantities and variables. Therefore all of the transport equations have to be averaged. First averaging method is Reynolds averaging that is performed over time difference. Instantaneous value is separated into time-averaged term and fluctuating term. Example of Reynolds averaging is shown below

$$u = \bar{u} + u' \quad \bar{u} = \lim_{T \rightarrow \infty} \frac{1}{T} \int_0^T u(x, t) dt \quad (3.12)$$

where \bar{u} denotes the time-average term and u' the fluctuating term. Since density is also changing, it is part of averaging. This leads into complex transport equations if every term has two different components. Therefore second method, called Favre averaging, is used to simplify transport equations by taking density changes into consideration while averaging. Example is shown below

$$u = \tilde{u} + u'' \quad \tilde{u} = \frac{\bar{\rho} u}{\bar{\rho}} \quad (3.13)$$

where \tilde{u} denotes the density- and time-averaged term and u'' term that includes density and time fluctuations. Favre-averaged continuity equation becomes

$$\frac{\partial \bar{\rho}}{\partial t} + \frac{\partial(\bar{\rho} \tilde{u}_j)}{\partial x_j} = 0 \quad (3.14)$$

Favre-averaged momentum equation

$$\frac{\partial(\bar{\rho} \tilde{u}_i)}{\partial t} + \frac{\partial(\bar{\rho} \tilde{u}_i \tilde{u}_j)}{\partial x_j} = \frac{\partial \bar{p}}{\partial x_i} + \frac{\partial}{\partial x_j} \left[\mu \left(\frac{\partial \tilde{u}_i}{\partial x_j} + \frac{\partial \tilde{u}_j}{\partial x_i} - \frac{2}{3} \delta_{ij} \frac{\partial \tilde{u}_k}{\partial x_k} \right) - \overline{\rho u_i'' u_j''} \right] \quad (3.15)$$

where $\overline{\rho u_i'' u_j''}$ is the Reynolds stress. Modelling of Reynolds stresses is discussed more in chapter 3.3.

Favre-averaged energy equation

$$\frac{\partial(\bar{\rho} \tilde{h})}{\partial t} + \frac{\partial(\bar{\rho} \tilde{h} \tilde{u}_j)}{\partial x_j} = \frac{\partial}{\partial x_j} \left[\bar{\rho} \alpha \frac{\partial \tilde{h}}{\partial x_j} - \overline{\rho h'' u_j''} \right] + \overline{S_{rad}} + \overline{S_{comb}} \quad (3.16)$$

in which modelling of $-\overline{\rho h'' u_j''}$ term is simplified with gradient diffusion assumption

$$-\overline{\rho h'' u_j''} = \frac{\mu_t}{Pr_s^t} \frac{\partial \tilde{h}}{\partial x_j} \quad (3.17)$$

When applying diffusion assumption to the energy transport equation

$$\frac{\partial(\overline{\rho \tilde{h}})}{\partial t} + \frac{\partial(\overline{\rho \tilde{h} u_j})}{\partial x_j} = \frac{\partial}{\partial x_j} \left[\left(\frac{\mu}{Pr_h} + \frac{\mu_t}{Pr_h^t} \right) \frac{\partial \tilde{h}}{\partial x_j} \right] + \overline{S_{rad}} + \overline{S_{comb}} \quad (3.18)$$

where μ_t is the turbulent eddy viscosity and Pr_h^t the turbulent Prandtl number for enthalpy.

Favre-averaged species transport equation

$$\frac{\partial(\overline{\rho \tilde{Y}_s})}{\partial t} + \frac{\partial(\overline{\rho \tilde{u}_j \tilde{Y}_s})}{\partial x_j} = \frac{\partial}{\partial x_j} \left[\overline{\rho D_s} \frac{\partial \tilde{Y}_s}{\partial x_j} - \overline{\rho Y_s'' u_j''} \right] + \overline{\tilde{\omega}_s} \quad (3.19)$$

which modelling of $-\overline{\rho Y_s'' u_j''}$ term is simplified with the gradient diffusion assumption

$$-\overline{\rho Y_s'' u_j''} = \frac{\mu_t}{Sc_s^t} \frac{\partial \tilde{Y}_s}{\partial x_j} \quad (3.20)$$

When applying the diffusion assumption to specie transport equation result becomes

$$\frac{\partial(\overline{\rho \tilde{Y}_s})}{\partial t} + \frac{\partial(\overline{\rho \tilde{u}_j \tilde{Y}_s})}{\partial x_j} = \frac{\partial}{\partial x_j} \left[\left(\frac{\mu}{Sc_s} + \frac{\mu_t}{Sc_s^t} \right) \frac{\partial \tilde{Y}_s}{\partial x_j} \right] + \overline{\tilde{\omega}_s} \quad (3.21)$$

where Sc_s^t is the turbulent Schmidt number for specie. (Khadar 2015, 18-28.)

3.3 Turbulence modelling

Reynolds stress accounts for the momentum transfer which is caused by fluctuating velocities in turbulent flow. Turbulence modelling aims to solve closure problem related to Reynolds stresses in Favre-averaged momentum equation. There are in total six different Reynolds stress tensor elements which increase number unknown variables. The mathematical problem is not closed when there are more variables than equations to solve them. To close the equations, the Reynolds stresses need to be approximated with models that reduce the number of variables or increase the number of solvable equations. Reynolds-Averaged Navier-Stokes (RANS) models define effect of turbulence as an increase in viscosity. The effect that turbulence has on the fluid viscosity is a variable called eddy viscosity. Turbulence equilibrium is treated with production of turbulence called turbulent kinetic energy and loss of turbulent energy with dissipation rate of turbulence. (Ferziger 1997, 273-275.)

Two different turbulence models are used in this thesis. Standard $k - \epsilon$ model is used for Sandia Flame D simulations (see section 4.1) as it is the default turbulence model in the tutorial. Without any extended knowledge about turbulence models which are best suited for combustion modelling, $k - \epsilon$ model is also used in the process furnace simulations. One of the main differences in the between Sandia Flame D and the process furnace simulations is the swirling flow at the primary air inlet of the process furnace burner. Standard $k - \epsilon$ model is not well suited for swirling flows and therefore improved version is used, called realizable $k - \epsilon$ model.

3.3.1 Standard $k - \epsilon$ turbulence model

Modelling of Reynolds Stresses with RANS models is done with Boussinesq eddy-viscosity concept (Marzaouk 2010)

$$-\overline{\rho u_i'' u_j''} = \mu_t \left(\frac{\partial \bar{u}_i}{\partial x_j} + \frac{\partial \bar{u}_j}{\partial x_i} - \frac{2}{3} \delta_{ij} \frac{\partial \bar{u}_k}{\partial x_k} \right) - \frac{2}{3} \bar{\rho} \tilde{k} \delta_{ij} \quad (3.22)$$

where k is the turbulent kinetic energy. Eddy viscosity μ_t is defined as follows

$$\mu_t = \frac{C_\mu \bar{\rho} \tilde{k}^2}{\tilde{\epsilon}} \quad (3.23)$$

where C_μ is a constant and ϵ the dissipation rate of turbulent energy.

Turbulent kinetic energy is evaluated with the following transport equation

$$\frac{\partial (\bar{\rho} \tilde{k})}{\partial t} + \frac{\partial \bar{\rho} \tilde{k} \bar{u}_j}{\partial x_j} = \frac{\partial}{\partial x_j} \left[\left(\mu + \frac{\mu_t}{Pr_k^t} \right) \frac{\partial \tilde{k}}{\partial x_j} \right] + P - \bar{\rho} \tilde{\epsilon} \quad (3.24)$$

Rate of turbulent energy dissipation is evaluated as

$$\frac{\partial \bar{\rho} \tilde{\epsilon}}{\partial t} + \frac{\partial \bar{\rho} \tilde{\epsilon} \bar{u}_j}{\partial x_j} = \frac{\partial}{\partial x_j} \left[\left(\mu + \frac{\mu_t}{Pr_\epsilon^t} \right) \frac{\partial \tilde{\epsilon}}{\partial x_j} \right] + \frac{\tilde{\epsilon}}{\tilde{k}} (C_{\epsilon 1} G - C_{\epsilon 2} \bar{\rho} \tilde{\epsilon}) - \left(\frac{2}{3} C_{\epsilon 1} + C_{\epsilon 3} \right) \bar{\rho} \tilde{\epsilon} \frac{\partial \bar{u}_k}{\partial x_k} \quad (3.25)$$

where Pr_k^t and Pr_ϵ^t are turbulent Prandtl numbers for k and ϵ . $C_{\epsilon 1}$, $C_{\epsilon 2}$ and $C_{\epsilon 3}$ are model constants. P is the rate of turbulent kinetic energy production and is defined as

$$P = G - \frac{2}{3} \bar{\rho} \tilde{k} \frac{\partial \bar{u}_k}{\partial x_k} \quad G = 2\mu_t \left(S_{ij} S_{ij} - \frac{1}{3} \left[\frac{\partial \bar{u}_k}{\partial x_k} \right]^2 \right) \quad S_{ij} = \frac{1}{2} \left(\frac{\partial u_i}{\partial x_j} + \frac{\partial u_j}{\partial x_i} \right) \quad (3.26)$$

Model constants are given as

$$Pr_k^t = 1 \quad Pr_\epsilon^t = 1.3 \quad C_\mu = 0.09 \quad C_{\epsilon 1} = 1.44 \quad C_{\epsilon 2} = 1.92 \quad C_{\epsilon 3} = -0.33$$

The standard $k - \epsilon$ model is widely used in engineering applications due to its robustness and relatively wide applicability but there are still some fundamental problems with the model. Use of Boussinesq eddy-viscosity assumes that turbulence is isotropic i.e. uniform in all directions. Therefore model only gives equal values for normal Reynolds stresses. This leaves model incapable of predicting secondary flows which are created by non-uniform normal Reynolds stresses. The standard $k - \epsilon$ model cannot be used for swirling flows without modification. Realizability is not completely satisfied in the standard $k - \epsilon$ model. (Biswas 2002 ,336)

3.3.2 Realizable $k - \epsilon$ turbulence model

Standard $k - \epsilon$ model assumes the coefficient C_μ to be constant which can cause normal stresses to become negative with large mean strain rate. Failure to reach mathematical constraints of Schwarz' inequality ($\overline{u_i^2} \geq 0$, $\overline{u_i u_j^2} \leq \overline{u_i^2} \overline{u_j^2}$) in turbulent flows leads to non-realizable model. (Shih 1995, 228, 232.) In realizable $k - \epsilon$ model, the coefficient C_μ has its own equation to avoid realizability issues. C_μ is defined as (Marzaouk 2010)

$$C_\mu = \frac{1}{A_0 + A_s U^* \frac{k}{\epsilon}} \quad (3.27)$$

where A_0 is constant. Term A_s is defined as

$$A_s = \sqrt{6} \cos(\phi) \quad \phi = \frac{1}{3} \arccos(\sqrt{6}W) \quad W = 2\sqrt{2} \frac{S_{ij} S_{jk} S_{ki}}{S^3} \quad S = \sqrt{S_{ij} S_{ij}} \quad (3.28)$$

Term U^* is calculated as

$$U^* = \sqrt{S_{ij} S_{ij} + \Omega_{ij} \Omega_{ij}} \quad \Omega_{ij} = \frac{1}{2} \left(\frac{\partial U_i}{\partial x_j} - \frac{\partial U_j}{\partial x_i} \right) \quad (3.29)$$

Equation for kinetic energy remains the same compared to standard $k - \epsilon$ model but dissipation rate equation has a new form as

$$\frac{\partial \bar{\rho} \tilde{\epsilon}}{\partial t} + \frac{\partial \bar{\rho} \tilde{\epsilon} \bar{u}_j}{\partial x_j} = \frac{\partial}{\partial x_j} \left[\left(\mu + \frac{\mu_t}{Pr_\epsilon^t} \right) \frac{\partial \tilde{\epsilon}}{\partial x_j} \right] + C_1 \frac{\tilde{\epsilon}}{k} S - C_{\epsilon 2} \bar{\rho} \frac{\tilde{\epsilon}^2}{k + \sqrt{(\mu/\bar{\rho}) \tilde{\epsilon}}} \quad (3.30)$$

where $C_{\epsilon 2}$ is constant but C_1 is defined as

$$C_1 = \max\left(0.43, \frac{\eta}{\eta+5}\right) \quad \eta = \frac{k}{\epsilon} \sqrt{2S_{ij}S_{ij}} \quad (3.31)$$

Model constants are

$$Pr_k^t = 1 \quad Pr_\epsilon^t = 1.2 \quad C_{\epsilon 2} = 1.9 \quad A_0 = 4.0$$

Realizable $k - \epsilon$ model is an improved method compared with the standard version. The realizable version fulfills all the necessary mathematical constraints and does not produce non-physical results as easily as the standard model. The downside is that an increased number of equations increases the computational time. It is also important to keep in mind that the realizable model is still based on same Boussinesq approximation and is suffers from the same isotropy as the standard model.

3.4 Reaction modelling

Reaction modelling addresses turbulence-chemistry interaction. Both turbulence (i.e. mixing of reactants) and chemical kinetics have an effect on reaction rates. Models differ based on assumptions about more dominant timescale. If the turbulent time scale is assumed short and chemical reactions complex or slow, the chemical timescale controls the reaction speed. If the reactions are considered fast or simple, mixing is in control of the reaction speed. In more detailed models, both timescales can be taken into account and the minimum of the two used as the limiting factor.

3.4.1 Eddy Dissipation Model (EDM)

Eddy Dissipation Model (EDM) assumes that chemical reactions are faster than mixing which means that when species have achieved sufficient mixture of fuel and air, combustion begins immediately. Therefore, turbulence controls reaction rate as it is responsible of the mixing of gases. EDM assumes that all mixed reactants form products immediately and only factor limiting the reactions is the sufficient mixing of fuel and oxidizer. Reaction rate is defined as

$$\tilde{\omega}_s = Av_s M_s \rho \frac{\tilde{\epsilon}}{\bar{k}} \min\left(\frac{\tilde{Y}_R}{v_s M_s}, B \frac{\sum_P \tilde{Y}_P}{\sum^N v_s M_s}\right) \quad (3.32)$$

where $A = 4$ and $B = 0.5$ are model constants, v_s is the reaction stoichiometric coefficient for specie and subscripts R and P refer to reactant and product respectively.

(Halouane 2017, 21993.) EDM is not readily available in the current open OpenFOAM release 6.0, but Fluent simulations, that are used for comparison of results in this work, were made using the EDM.

3.4.2 Eddy Dissipation Concept (EDC)

Eddy Dissipation Concept is a detailed chemistry model which can be used while either mixing or chemical kinetics are dominating the reaction rates. This means that EDC calculates the effect of reaction kinetics and mixing to combustion, and uses the smaller value to determine reaction rate. Turbulent energy is dissipated in fine structures of smallest eddies that convert the turbulent kinetic energy to heat by molecular movement. EDC model considers these fine structures to be the place where chemical reactions occur while sufficient mixing and temperature has been achieved. These regions can be determined with fast chemistry approach which assumes equilibrium in fine structures or detailed chemistry approach which assumes fine structures as well as stirred reactors. (Kadar 2015, 32-33.)

EDC model calculates the mass fraction of fine structures as

$$\gamma = 2.1377 \left(\frac{\nu \tilde{\epsilon}}{\bar{k}^2} \right)^{\frac{1}{4}} \quad (3.33)$$

where ν is kinematic viscosity. Residence time inside the fine structures is defined as

$$\tau^* = 0.4083 \sqrt{\frac{\nu}{\tilde{\epsilon}}} \quad (3.34)$$

Reaction rate for certain species can be calculated as

$$\widetilde{\omega}_s = - \frac{\gamma^2}{1-\gamma^2} \frac{\bar{\rho}(\tilde{Y}_s - \tilde{Y}_s^*)}{\tau^*} \quad (3.35)$$

where \tilde{Y}_s is species mass fraction that is solved from the individual specie transport equation. \tilde{Y}_s^* is the specie fraction in the reacting region and has to be calculated with fast or detailed chemistry approach.

3.4.3 Partially Stirred Reactor (PaSR)

Partially stirred reactor combustion model assumes that flames are thinner and reactions occur in smaller regions than mesh cell size. Therefore calculation cells are divided into reacting and non-reacting regions. The reacting region is assumed to behave as perfectly stirred reactor meaning that species are mixed and react fully. After reactions turbulence mixes the species between reacting and non-reacting regions inside the cell. This gives a partially stirred cell as final result. (Li 2018, 639-640.) The reaction rate is calculated in PaSR model as

$$\widetilde{\omega}_s = -\kappa \frac{\bar{\rho}(\widetilde{Y}_s - \widetilde{Y}_s^*)}{\tau_{mix}} \quad (3.36)$$

where κ is the mass fraction of the reacting cell region. Mass fraction is defined as

$$\kappa = \frac{\tau_c}{\tau_c + \tau_{mix}} \quad (3.37)$$

where τ_c is the chemical time scale and τ_{mix} the turbulent mixing time scale. The turbulent mixing time is evaluated as

$$\tau_{mix} = C_{mix} \sqrt{\frac{\mu_{eff}}{\bar{\rho}\bar{\epsilon}}} \quad (3.38)$$

where C_{mix} is a coefficient used to adjust the turbulent mixing time scale and $\mu_{eff} = \mu + \mu_t$, the effective dynamic viscosity. The chemical time scale can be calculated from the reaction rates as follows

$$\tau_c = \frac{n_r \cdot Y_{tot}^*}{\sum_{n=1}^{n_r} \left(\frac{dY_{n_r,forward}^*}{dt} \nu_{n_r,sum} \right)} \quad (3.39)$$

where n_r is the number of reactions, Y_{tot}^* the total concentration from ideal gas law. $\frac{dY_{n_r,forward}^*}{dt}$ is the reaction rate forwards and $\nu_{n_r,sum}$ the sum of product stoichiometric coefficients. (Li 2018, 639-642.)

3.5 Radiation modelling

Radiative heat transfer becomes dominant in high temperature applications. This can be seen in Stefan-Boltzmann law of blackbody radiation. Blackbody is an ideal radiator that can emit and absorb all of the possible radiation.

$$E_b = \sigma T_{surf}^4 \quad (3.40)$$

where E_b is the rate of released energy per area, σ is the Stefan-Boltzmann constant ($5.67 \cdot 10^{-8} \text{ W/m}^2\text{K}$) and T_s the surface temperature. A low value of the Stefan-Boltzmann constant limits the radiative heat transfer with low temperatures. The rate of released energy grows rapidly as temperature rises and has significant effect to the energy balance. (Incropera 2007, 738-739.)

The Radiative Transfer Equation (RTE) describes the radiative heat transfer in participating medium. The RTE calculates the change of spectral radiation intensity (I_λ) as radiation travels inside the medium. The RTE can be expressed in general form as

$$\frac{dI_\lambda(\mathbf{s})}{ds} = -\kappa_\lambda I_\lambda(\mathbf{s}) + \kappa_\lambda I_{b\lambda} - \sigma_{s\lambda} I_\lambda(\mathbf{s}) + \frac{\sigma_{s\lambda}}{4\pi} \int_{4\pi} I_\lambda(\mathbf{s}^*) \Omega(\mathbf{s}, \mathbf{s}^*) d\Omega^* \quad (3.41)$$

where κ_λ is the absorption coefficient, $\sigma_{s\lambda}$ is the scattering coefficient, \mathbf{s} is the traveling direction of the spectral intensity and $\Omega(\mathbf{s}, \mathbf{s}^*)$, the scattering phase function. The scattering phase function considers the probability of radiation scattering from direction \mathbf{s}^* to direction \mathbf{s} . The first term on the right hand side of RTE is absorption, the second emission and the last scattering. The effect of scattering is neglected and only absorption and emission are considered in the present calculations. A simplified version of the RTE is then

$$\frac{dI_\lambda(\mathbf{s})}{ds} = -\kappa_\lambda I_\lambda(\mathbf{s}) + \kappa_\lambda I_{b\lambda} \quad (3.42)$$

Radiation is included as a source term (S_{rad}) in the energy transport equation. The source term is calculated as the divergence of the radiative heat flux vector (\mathbf{q}). Divergence means volume flux outwards from the computational volume. The equation for heat flux can therefore be obtained by integrating RTE across all possible wavelengths and over all directions of a solid angle. If the medium is considered grey i.e. the wavelength does not have effect on the radiation properties, the result of integration is

$$S_{rad} = -\nabla \cdot \mathbf{q} = \kappa G - 4\kappa\sigma T^4 \quad (3.43)$$

where G is the total incident radiation intensity. On the right hand side, the first term represents heat gain, and the second one heat loss. The total radiation intensity is not known beforehand and it needs to be calculated. Following sections will presented two different radiation models that are used in this work and are both available in Fluent and in OpenFOAM.

3.5.1 P1

P1-approximation method uses spherical harmonics for calculation of incident radiation. Thermal radiation is considered to be a diffusive phenomenon and the transport equation becomes (Garten 2015, 70)

$$-\nabla \cdot (\Gamma \nabla G) = \kappa G - 4\kappa\sigma T^4 \quad \Gamma = \frac{1}{3\kappa} \quad (3.44)$$

P1-approximation does not predict heat transfer correctly if the transport media is optically thin (Modest 2013, 509). Optically thin is term that is used for describe medias that have low transmissivity τ . Transmissivity indicates how much radiation energy is absorbed into gaseous medium. Therefore, an optically thin media absorbs less radiation than an optically thick one. (Modest 2013, 24.)

3.5.2 Discrete Ordinates Method (DOM)

The Discrete Ordinates Method approximates the incident radiation by dividing the solid angle into discrete sections. The simplified RTE is written for DOM as follows (Garten 2015, 71)

$$\mu_k \frac{dI_{\lambda,k}}{dx} + \xi_k \frac{dI_{\lambda,k}}{dx} + \eta_k \frac{dI_{\lambda,k}}{dx} = -\kappa_\lambda I_\lambda(\mathbf{s}) + \kappa_\lambda I_{b\lambda} \quad (3.45)$$

where μ , ξ and η are directional cosines which are calculated as scalar products of discrete directional vector and unit vector of Cartesian coordinate system. Incident radiation is calculated as follows

$$G = \int_{4\pi} I d\Omega \approx \sum_{k=1}^K w_k I_k \quad (3.46)$$

where weight factors w_k are used to approximate the integration over the solid angle.

3.6 Literature study about OpenFOAM combustion studies

Table I in Appendix I lists recent combustion studies in open literature. Focus of literature review was on most recent studies, since OpenFOAM has been under major development since 2011. Therefore only the most recent studies would be more likely to use models similar than in the current version of OpenFOAM 6 used in this work. References listed in Table I include studies about non-premixed combustion with OpenFOAM software. Information about most important sub-models are listed along with general information about authors and simple description of study. Not all of the sources report information concerning every modelling aspect, but overall Table I shows the most important features among different studies.

Most literature studies were done with reactingFoam or fireFoam solvers. Different versions of reactingFoam (such as rhoReactingFoam) were not popular. In the reactingFoam cases flame was probably seen as momentum driven rather than buoyancy driven. Momentum driven flame refers to high inlet velocity of the fuel and buoyancy driven to lower inlet velocity. With high velocity buoyancy has no time to have significant effect to the flame shape. Momentum and buoyancy forces can be evaluated with Froude's number

$$Fr = \frac{u_{f,0}}{\sqrt{gD}} = \frac{\text{momentum forces}}{\text{gravity forces}} \quad (3.47)$$

where Fr is Froude number, $u_{f,0}$ the fuel inlet velocity, g the gravitational constant and D is the hydraulic mean depth. The hydraulic mean depth is calculated by dividing flow cross sectional area by the width of the cross section. With Froude number close to 1 both forces have effect in same magnitude. Values below 1 would suggest buoyancy dominated flow and above 1 momentum dominant flow. (Wu 2010, 408) Froude numbers of some the literature studies are presented in Table 3.1. Process furnace case in this thesis has Froude number of 412 i.e. the momentum forces dominate over the buoyancy forces.

Table 3.1. Froude number of some cases from literature review.

Authors	Year	Case Description	Combustion Solver	Froude number
Xia, Duran, Morgans, Han	2017	Gas turbine combustor	reactingFoam,	13.3
Li, Xia, Morgans Han	2017	Combustor with long flame	reactingFoam	9.1
Han, Li, Morgans	2015	Combustor injector	reactingFoam	14.6
Han, Yang, Mao	2016	Combustor	reactingFoam	14.6
Endres, Sattelmayer	2018	Turbulent boundary layer flashback, hydrogen-air flame	reactingFoam	10.8
Sedano, Lopez, Ladino, Munoz	2017	Small-scale pool fire	fireFoam	0.01
Vilfayeau, White, Sunderland, Marshall, Trouve	2016	Flame extinction with air-nitrogen co-flow	fireFoam	0.09

In Table 3.1, reactingFoam cases have high Froude numbers and fireFoam cases low ones. Listed cases for reactingFoam involve combustor simulations where fuel is injected to the combustion chamber with high velocity. High inlet velocity leads to high Froude numbers and momentum dominated flow. FireFoam cases simulated as natural fires or buoyant flame experiments without forced injection of fuel. Froude number remains low and buoyancy dominates the flow.

Cases based on reactingFoam solver were mainly dedicated to combustion inside process equipment and focused on investigating combustion characteristics and flame shape. With fireFoam solver, studies were focused on uncontrolled combustion in accident or emergency situations. Solver was used to simulate the ignition and early phases of combustion along fire suppression with different methods. Therefore, as the solver naming already suggests, it can be said that fireFoam solver is mainly used to examine and prevent destructive fires whereas reactingFoam solver is used for simulating intentional combustion in furnaces and burners.

To solve pressure velocity coupling, most studies use PIMPLE method, combined from PISO (Pressure Implicit Split Operator) and SIMPLE (Semi Implicit Method of Pressure

Linked Equations) methods. In OpenFOAM, SIMPLE method is used for steady-state analysis and PISO for transient calculation. Merging these two methods results in more robust transient solver PIMPLE that can handle larger Courant numbers than PISO alone. (Holtmann 2016, 112.)

Majority of the studies preferred Large Eddy Simulations (LES) for turbulence modelling. LES model solves the large scales of turbulence but leaves smaller scales for modelling. LES method is more accurate in capturing turbulent eddies than RANS modelling (see section 3.3 for RANS modelling). RANS models provide a time-averaged solution for predicting mean flow conditions. RANS models are more commonly used in industrial application for their robustness and faster computational time compared to LES models. LES simulations are carried out for academic and research purposes where more detailed solution is preferred.

Radiation models were rarely mention with reactingFoam solver but are more consistently described with fireFoam solver. Only finite volume discrete ordinates method (fvDOM) was mentioned from all of the radiation models in OpenFOAM (viewFactor, P1 model). Some studies used simpler loss coefficient method to simulate radiation. In addition to radiation model selection, some sources mentioned use of Weighted Sum of Gray Gases Model (WSGGM) to calculate total emissivity and absorptivity of gas.

3.7 Chosen sub-models for this work

Simulations in this thesis focus on modelling of single gas flame in an industrial-scale process furnace and this section serves as a basis for the sub-models selected for this work. The suitability of OpenFOAM on industrial scale simulation is judged based on the ability to properly predict heat transfer and flame shape in the process furnace.

- Solver: Based on literature studies discussed in the previous section, reactingFoam is the most used solver type for controlled non-premixed combustion problems.

- Pressure-velocity coupling: PIMPLE method is used for robust calculation of the pressure-velocity coupling in the simulation, since it is able to model large variety of time scales which are present in combustion simulation.
- Turbulence: Turbulence models have significant effect on simulation computational time. It is important to consider the emphasis of accuracy and time consumption. Often in industrial applications quantities of mean flow are considered detailed enough. RANS models are widely used in industrial application and $k-\epsilon$ turbulence model is common for combustion simulations. $k-\epsilon$ model has ability to evaluate effect of turbulence in wide range of scales and realizable $k-\epsilon$ model has better ability to capture effect of turbulence in rotating flows (Shih 1995, 235).

Therefore models for combustion and radiation are most crucial for successful completion of simulations. To clarify the differences in combustion and radiation models available in OpenFOAM 6, most common options mentioned in Table I will be tested in chapter 4.1 for the process furnace studied in this thesis.

- Turbulence-chemistry interaction: The eddy dissipation concept (EDC) and partially stirred reactor (PaSR) are tested in work.
- Radiation: For radiation model options are P1 and finite volume discrete ordinates method (fvDOM). Absorption and emission of gas mixture are modelled with greyMeanAbsorptionEmission model in OpenFOAM which uses temperature dependent polynomials to estimate radiation properties of gas.

Sandia test cases combined with literature review of the models should give necessary understanding for final model selections for combustion and radiation modelling for the process furnace simulation.

4 CFD SIMULATIONS OF SANDIA FLAME D

This chapter starts the experimental part of the thesis. Work will include testing of different combustion and radiation models with Sandia Flame D. Boundary conditions and simulation domains will be presented for Sandia cases and results of the tests with Sandia Flame D are presented and compared to measurement data. Based on the Sandia flame results sub-models are chosen for the process furnace case.

4.1 Combustion model testing with Sandia Flame D

Sandia Flame D is a widely used validation case for turbulent combustion models and is also used in this work as a first test case before the actual simulations for a process furnace. Sandia National Laboratories performed experiments with CH₄/air flow ignited with a pilot jet. A fuel-air mixture was injected from a round nozzle (diameter $d = 7.2$ mm) surrounded by a high temperature pilot flame. Scalar quantities (for example temperature, N₂, O₂, H₂O and CO₂) and velocity were measured along axis ($x/d = 5, 10, 15, \dots, 80$) as well as radially ($x/d = 1, 2, 3, 7.5, 15, 30, 45, 60, 75$). (Barlow 2007.) Figure 4.1 shows the burner used in the experiment with main and pilot jet.



Figure 4.1. Burner used in Sandia Flame experiments (Barlow 2007).

In Figure 4.1, pilot flames can be seen as blue triangles surrounding the main jet inlet. Tall flame from the main jet has blue boundary that raises upwards from the main jet inlet. Pilot and main jet are separated by wall and there is also outer wall surrounding the pilot jet.

The measurements can be compared to simulation data and therefore allow us to evaluate the model accuracy. The system is axisymmetric and computational costs are reduced by simulating only a small 3D wedge of the whole domain. The computational mesh was obtained from reactingFoam combustion tutorial case. It is shown below in Figure 4.2. Measurement locations are shown on the left side of the figure while the right side shows a close up of the inlet region.

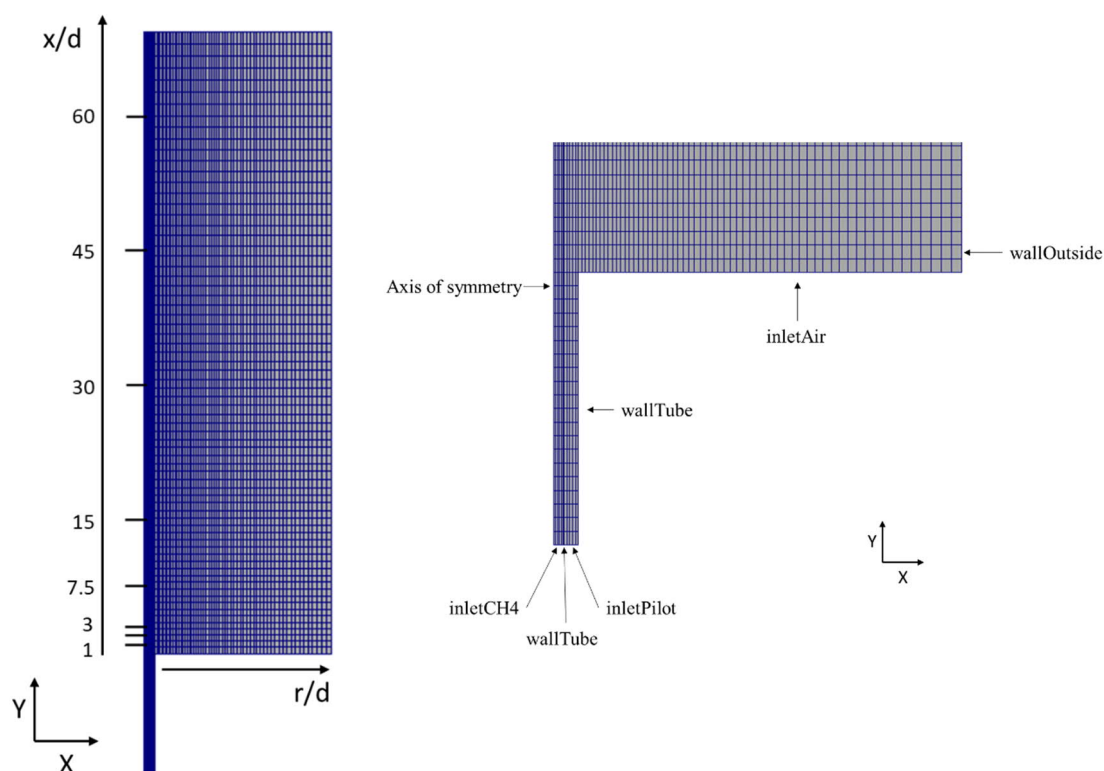


Figure 4.2. Mesh shown with measurement locations (left) and close up from inlet region (right).

In Figure 4.2, left side picture shows the measurement locations for the radial profile from $x/d=1$ to $x/d=60$. The mesh has 5170 cells in total with minimum edge length of 0.25 mm and maximum of 10 mm. The right side picture shows the boundaries of the mesh. Nearest to the axis of symmetry in y -direction is the CH_4 /air mixture inlet and beside it is the pilot

jet inlet. Between the two inlets is a tube wall that keeps the gas streams separate up to air inlet. Similar wall is placed at the outer boundary of the pilot jet inlet. Both of these walls are grouped under the same boundary condition. The boundary furthest away from the symmetry axis is named outside wall but is in reality only boundary of air volume and not an actual wall. The boundary between tube and outside wall is air inlet. Outlet boundary is not shown but it is located at the other end of the domain. The maximum height of the domain is 0.6 m and the maximum width is 0.15 m.

4.2 Sandia Flame D: Boundary conditions

Model settings were based on the reactingFoam combustion tutorial with only some small modifications when the model is changed to radiation or combustion. The main boundary conditions are listed in Table 4.1. Gas compositions at inlets are presented in mole percentages since results are also viewed with same units and temperature is also changed to Celsius. The internal volume was initialized with temperature of 18 °C and pressure of 100 kPa. Domain was filled with air which consisted 79 % of N₂ and 21 % of O₂ in mole percentages. Wall functions and fixed turbulent intensity at the inlets were used as boundary conditions for the kinetic energy transport, while dissipation rate used standard wall function for walls and mixing length for inlets. Radiation models used Marshaks boundary condition for radiation for all boundaries. Reactions and thermodynamic data are based on simplified GRI 3.0 library (36 species and 219 reactions) for methane combustion where all of the reactions with nitrogen have been neglected.

Table 4.1. Boundary condition for Sandia Flame D.

Variable Unit	U (x, y, z) [m/s]	p [kPa]	T [°C]	CH4 [mol-%]	O2 [mol-%]	CO2 [mol-%]	N2 [mol-%]	H2O [mol-%]
inletPilot	(0 0 11.4)	zG	1607	0	4.92	7.28	76.49	15.25
inletAir	(0 0 0.9)	zG	18	0	20.73	0	79.27	0
inletCH4	(0 0 49.6)	zG	21	24.96	15.76	0	59.28	0
outlet	pressureInlet OutletVelocity	100	zG	zG	zG	zG	zG	zG
wallOutside	zG	zG	zG	zG	zG	zG	zG	zG
wallTube	noSlip	zG	zG	zG	zG	zG	zG	zG

zG = zeroGradient

In Table 4.1, zeroGradient is boundary condition that sets gradient normal to the boundary as zero. This means that variable value at the boundary is the same as in the cell

neighboring the boundary in normal direction. NoSlip boundary condition sets velocity at the boundary to zero. PressureInletOutletVelocity boundary condition is used for boundaries with fixed pressure condition. It uses zeroGradient condition for outflow and inflow velocity is based on internal cell normal value. (OpenCFD 2018.) The original tutorial case utilizes EDC for combustion and P1 for radiation modelling. In this work, a total of four different combinations were tested as listed in Table 4.2.

Table 4.2. Tested model combinations for Sandia Flame D.

Combination name	Combustion model	Radiation model
EDC_P1 (original tutorial)	EDC	P1
EDC_fvDOM	EDC	fvDOM
PaSR_P1	PaSR	P1
PaSR_fvDOM	PaSR	fvDOM

The simulations used the PISO algorithm that requires stabilization by restricting a global time step. The global time step of the simulation is restricted by the Courant number which is defined as

$$C = \frac{u\Delta t}{\Delta x} \quad (4.1)$$

where u is the local velocity, Δx the mesh size of the computational cell and Δt is the global time step. The smallest cell size determines the maximum time step and this increases the computational time of the simulation. Larger cells could be calculated with a larger time step to save time. Using a Local Time Stepping (LTS) method in OpenFOAM enables the calculation of an individual time step for each cell. LTS method uses the Courant number as the maximum limit for the time step and includes both flow time scale and temperature source time scale in the calculations of the individual time step. LTS method calculates steady-state solution. (Pang 2013)

4.3 Sandia Flame D: Simulations results

All of the Sandia cases were first ran for 1500 LTS iterations with chemistry off to achieve cold flow profile. After that chemistry was turned on and iterations continued up to 5000. Due to small mesh size, there were no significant differences in computational time when 14 minutes of real time were required for one simulation with 16 computational cores.

Combinations with EDC model reached convergence down to $10^{-4} - 10^{-3}$ region in residuals of pressure and velocity components. Combinations with PaSR model convergence was $10^{-3} - 10^{-2}$ with the same residuals. Convergence in turbulence and energy was similar in all of the combinations in the $10^{-6} - 10^{-5}$ region.

Favre averaged experimental data from measurements is used to illustrate accuracy of the models and compare them with each other. It should be noted that the chosen sub-models were operated in their default settings and that might affect the results. Results are presented from the last iteration step without time-averaging. Example of how the burner nozzle geometry is related to radial profiles is shown in Figure 4.3.

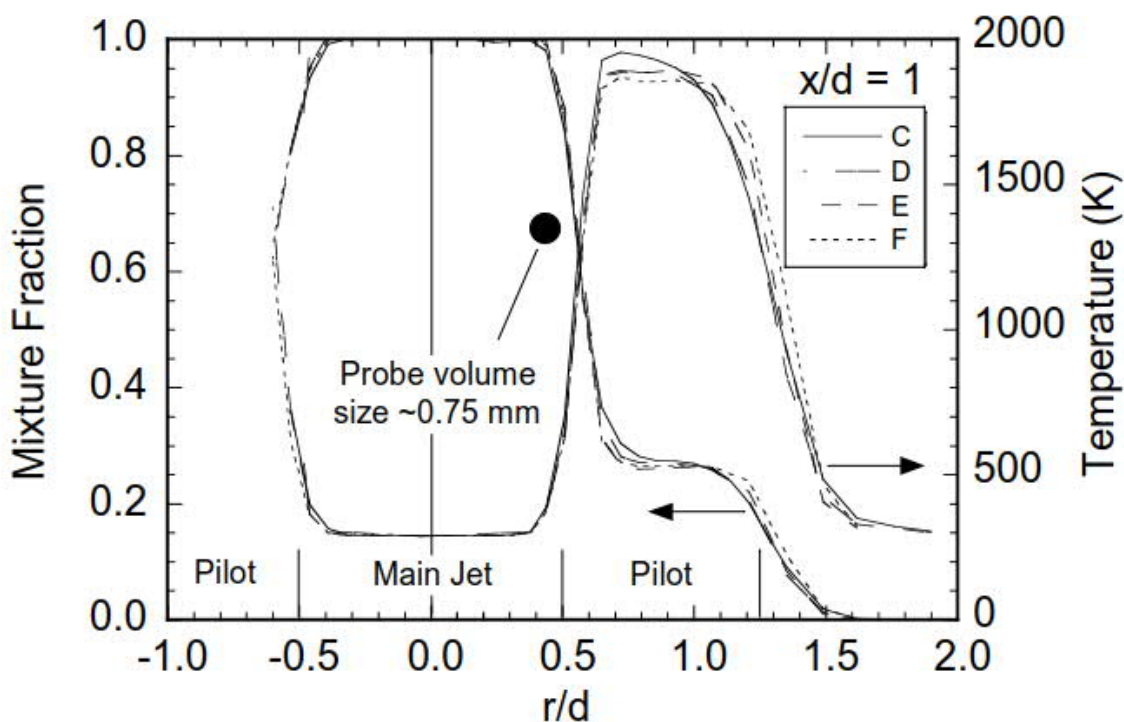


Figure 4.3. Sandia Flame D: Example of geometry position in radial profile at $x/d = 1$. (Barlow 2007, 5)

Figure 4.3 shows the temperature and mixture fraction distributions near the inlet at $x/d=1$. Legend of the Figure 4.3 shows the different case names for different main jet inlet velocities. Inlet velocities are 29.7 m/s, 49.6 m/s, 74.4 m/s and 99.2 m/s for flames C, D, E and F respectively. In Figure 4.3, main jet, which contains the mixture of CH_4 and air, is located at $r/d=0$. Main jet nozzle is between $-0.5 < r/d < 0.5$ surrounded by tube wall

that separates the main jet and the pilot jet. Pilot jet feeds the hot flue gases to ignite the main jet.

Results are compared with temperature and O₂ mole fraction radial profiles at locations $x/d = 3, 15$ and 45 . Temperature and O₂ mole fraction profiles in Figure 4.4 and Figure 4.5 show that all models predict flow behavior accurately near the burner nozzle at $x/d = 3$. Slight error between measurements and simulation results can be observed at boundary between main jet and pilot jet at $r/d = 0.5-1.0$.

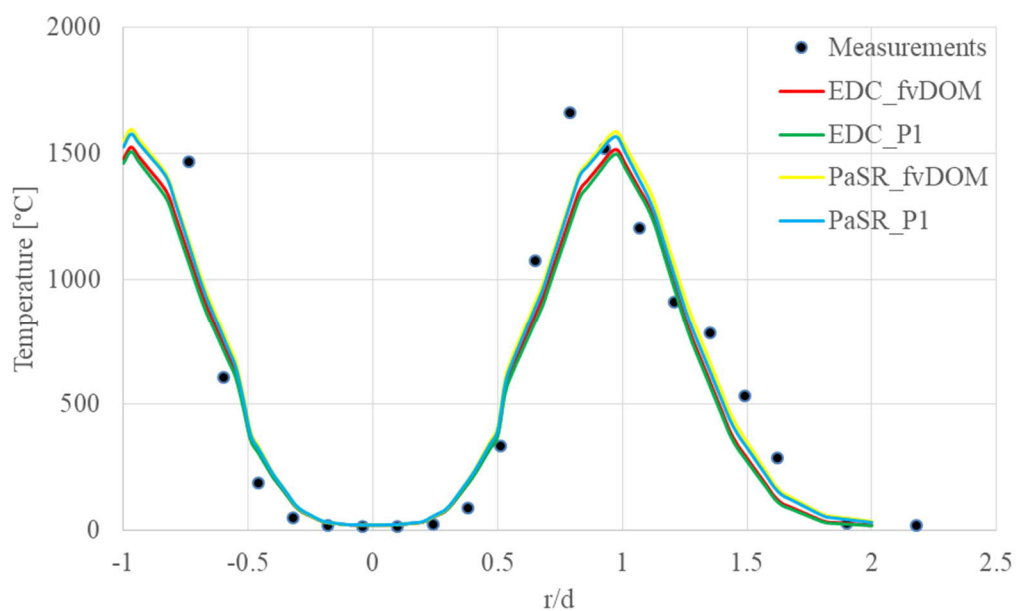


Figure 4.4. Sandia Flame D: Radial profile of temperature at $x/d = 3$.

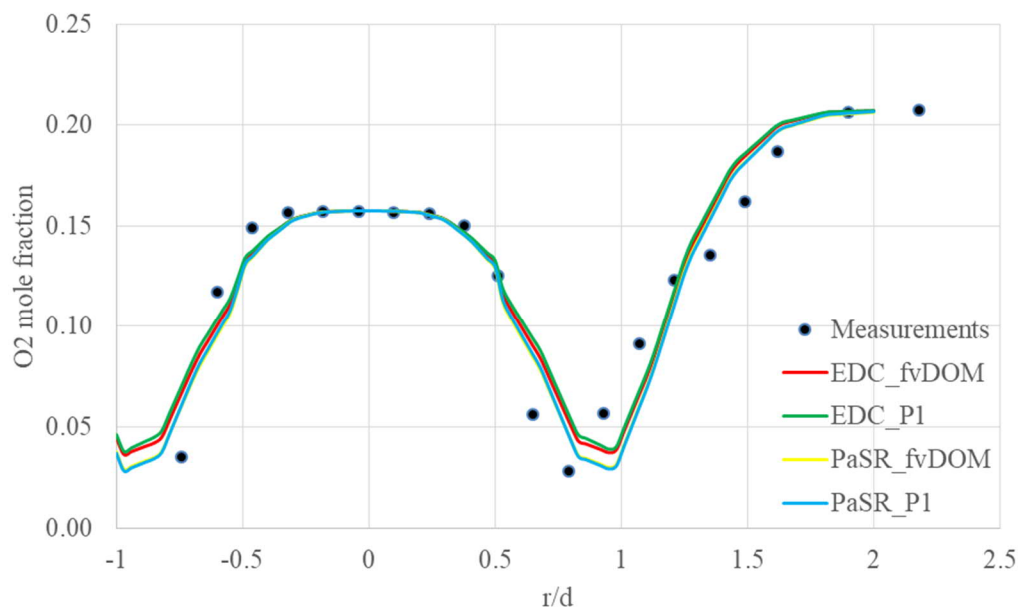


Figure 4.5. Sandia Flame D: Radial profile of O_2 mole fraction at $x/d = 3$.

Figure 4.6 and Figure 4.7 at further away from the burner ($x/d = 15$) show that differences between simulations and measurements begin to grow when moving radially outwards from center of main jet. Width of main jet in temperature and O_2 mole fraction profiles is narrower in the experiments than the models predict. Mixing of main jet is over predicted in all of the model combinations. Maximum temperature is highest at $1750\text{ }^\circ\text{C}$ with PaSR combustion model and lower at roughly $1600\text{ }^\circ\text{C}$ with EDC model. Both temperatures are overestimated compared to measurement at roughly $1300\text{ }^\circ\text{C}$. Fractions of O_2 are lower in simulation results than measurements which would indicate that reactions begin to occur earlier in the simulations than in reality.

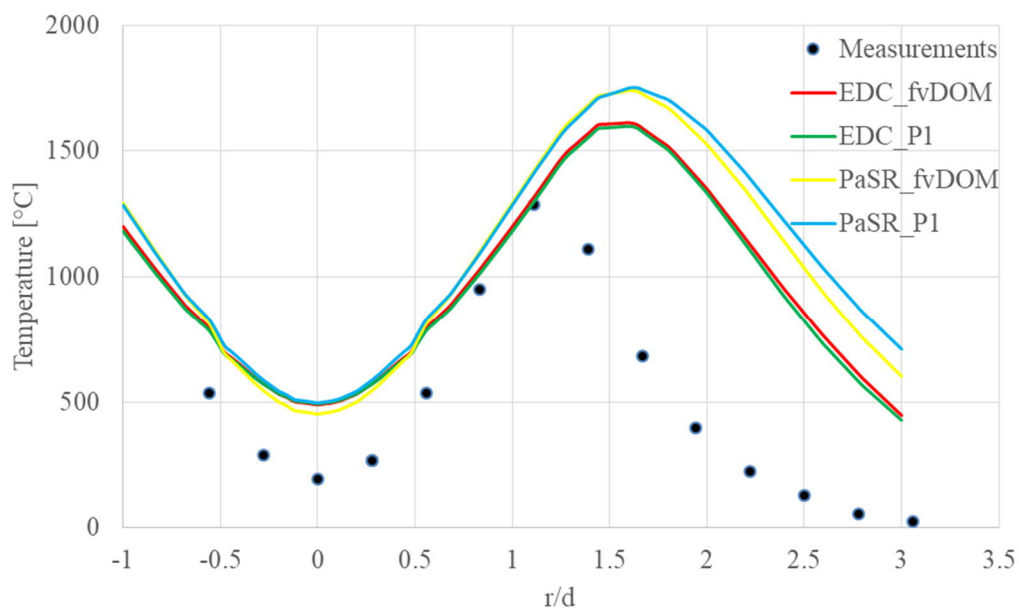


Figure 4.6. Sandia Flame D: Radial profile of temperature at $x/d = 15$.

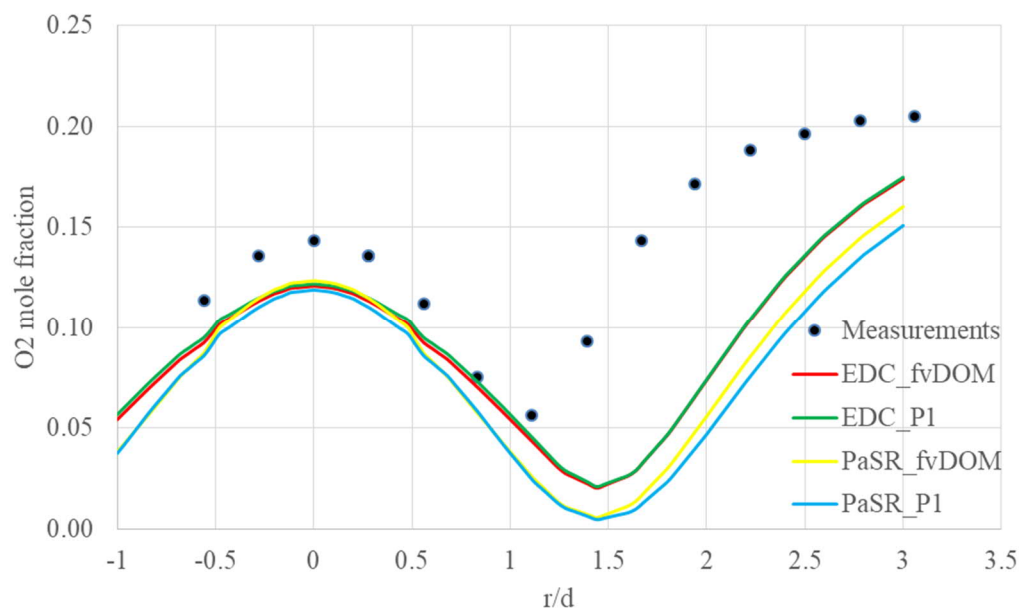


Figure 4.7. Sandia Flame D: Radial profile of O_2 mole fraction at $x/d = 15$.

Further away at $x/d = 45$ Figure 4.8 and Figure 4.9 show that as fuel-air mixture combusts maximum of temperature field moves to location of main jet. O_2 mole fraction is also lowest at main jet's path. Results from EDC model combinations are more in line with measurements while PaSR model gives higher temperature and lower O_2 fractions.

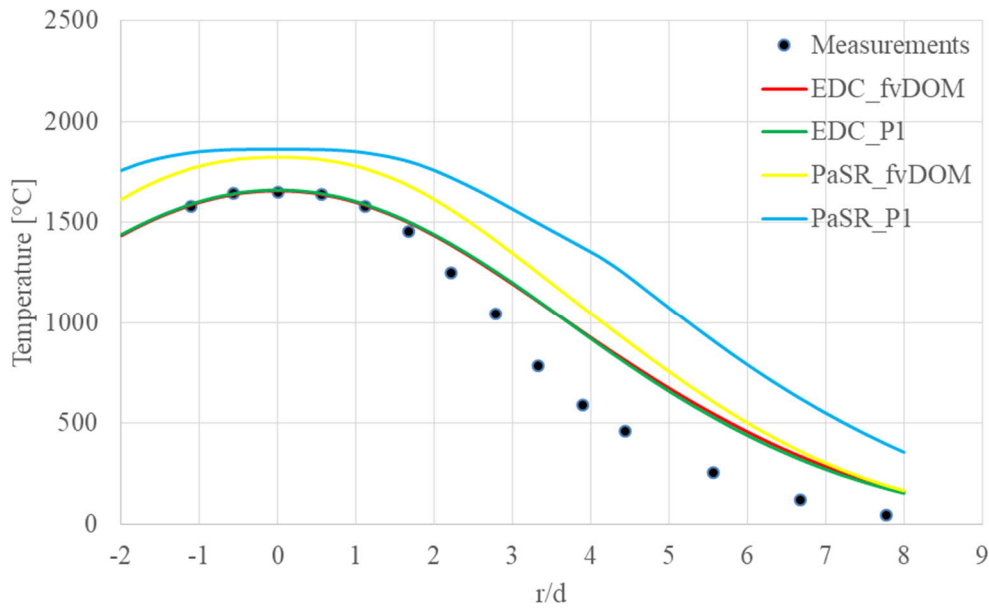


Figure 4.8. Sandia Flame D: Radial profile of temperature at $x/d = 45$.

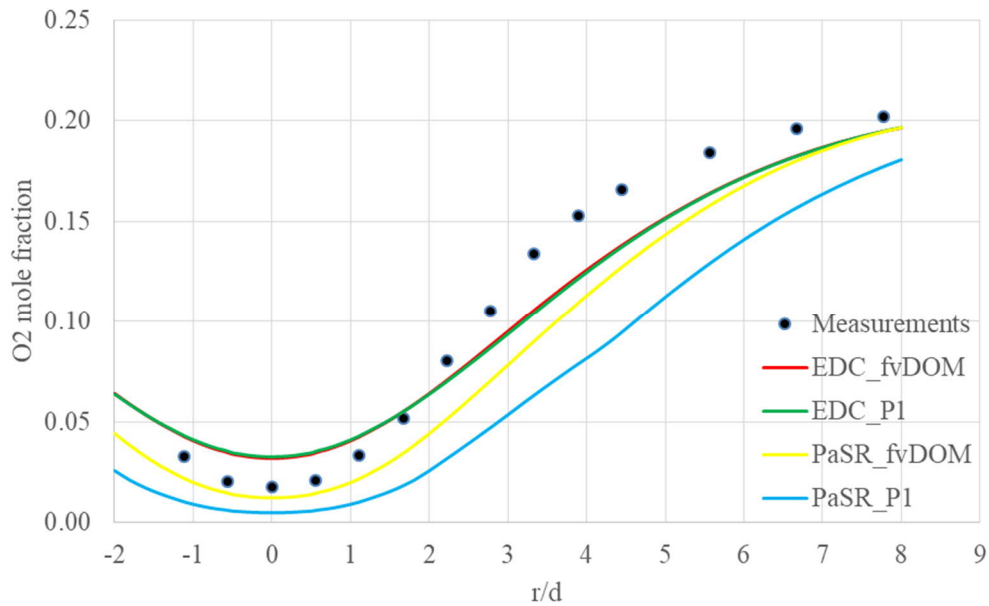


Figure 4.9. Sandia Flame D: Radial profile of O_2 mole fraction at $x/d = 45$.

EDC model results from different radiation model combinations did not change significantly. On the other hand radiation models had effect on PaSR model results, P1 giving worse results than fvDOM. All of the combinations tested were quite accurate near the burner. Errors begin to appear further away from the burner. Far away from the burner EDC model results are closer to the measurements than results with PaSR model.

Errors in the simulation results are calculated as relative error. Relative error is calculated by dividing absolute error between the simulation result and measurement with the measurement value. Relative error is modified to percentage value by multiplying by 100. Error values are calculated between measurement points and the closest possible simulation result values without interpolation. Errors are presented in Figure 4.10 and Figure 4.11 for temperature and O₂ mole fraction at $x/d = 3$.

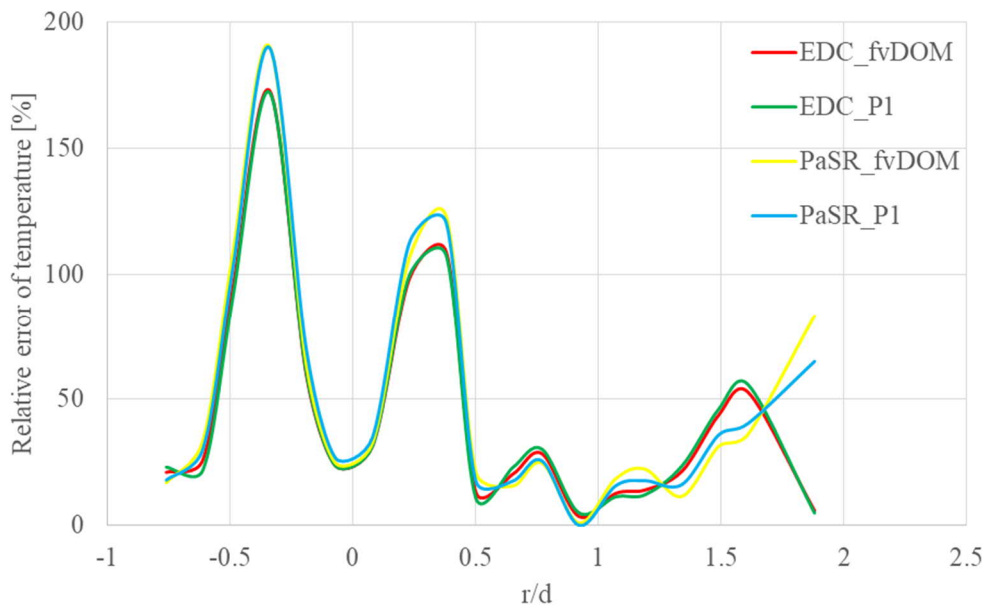


Figure 4.10. Sandia Flame D: Relative error of temperature at $x/d=3$.

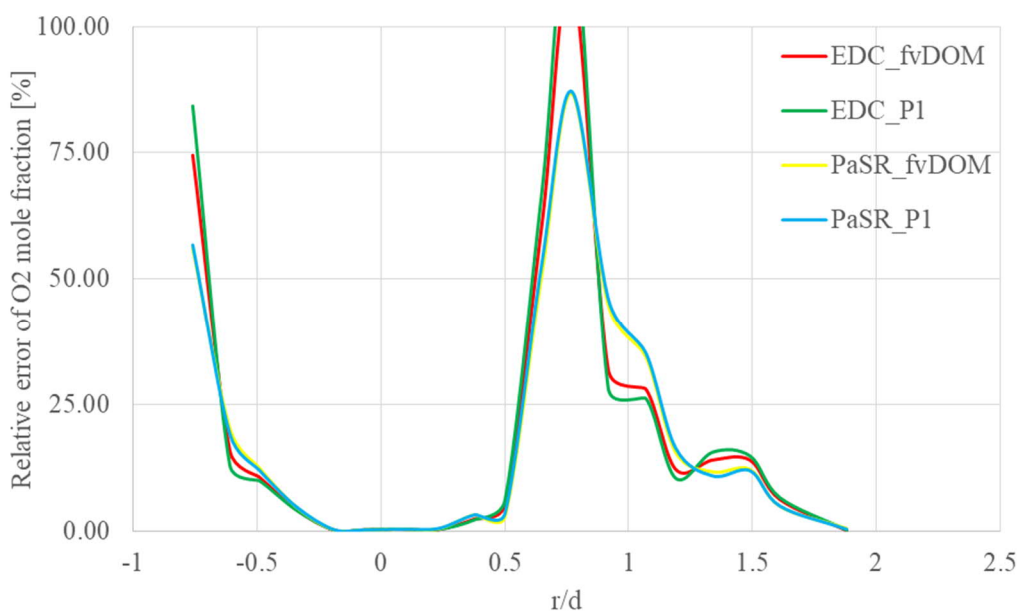


Figure 4.11. Sandia Flame D: Relative error of O₂ mole fraction at $x/d=3$.

Error between the simulation results and the measurements grows rapidly at intersection of main jet and pilot jet. At these intersections, where gradients are large are difficult to simulate accurately for the current test cases. Differences between test cases are small close to the burner and results are mainly inseparable. At the highest error spikes in Figure 4.10, PaSR cases have larger error for the temperature. For the O₂ mole fraction in Figure 4.11, PaSR cases have smaller error than EDC cases. Errors at $x/d = 15$ are presented in Figure 4.12 and Figure 4.13 for temperature and O₂ mole fraction.

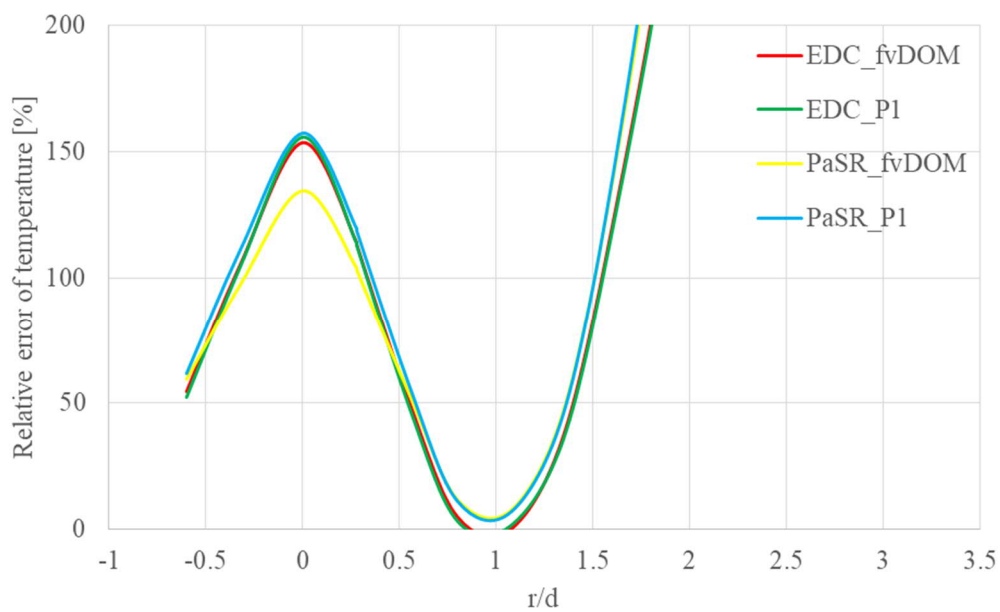


Figure 4.12. Sandia Flame D: Relative error of temperature at $x/d=15$.

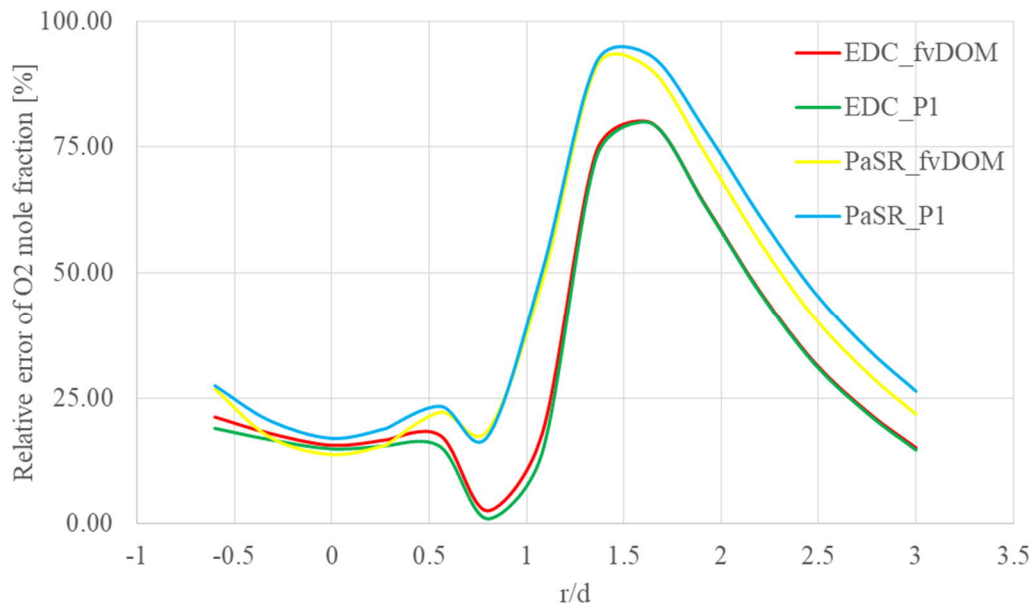


Figure 4.13. Sandia Flame D: Relative error of O₂ mole fraction at $x/d=15$.

Errors are mostly similar for temperature for all cases in Figure 4.12, but PaSR_fvDOM case has the smallest error at the center of the flame. For O₂ mole fraction, EDC cases have smaller errors than PaSR cases almost through the whole radial section. Errors at $x/d = 45$ are presented in Figure 4.14 and Figure 4.15 for temperature and O₂ mole fraction.

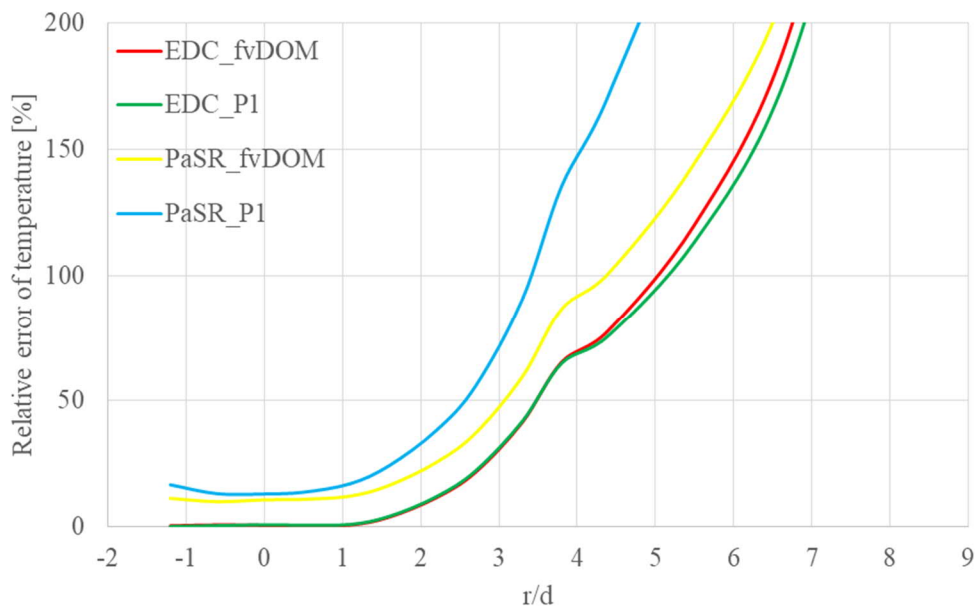


Figure 4.14. Sandia Flame D: Relative error of temperature at $x/d=45$.

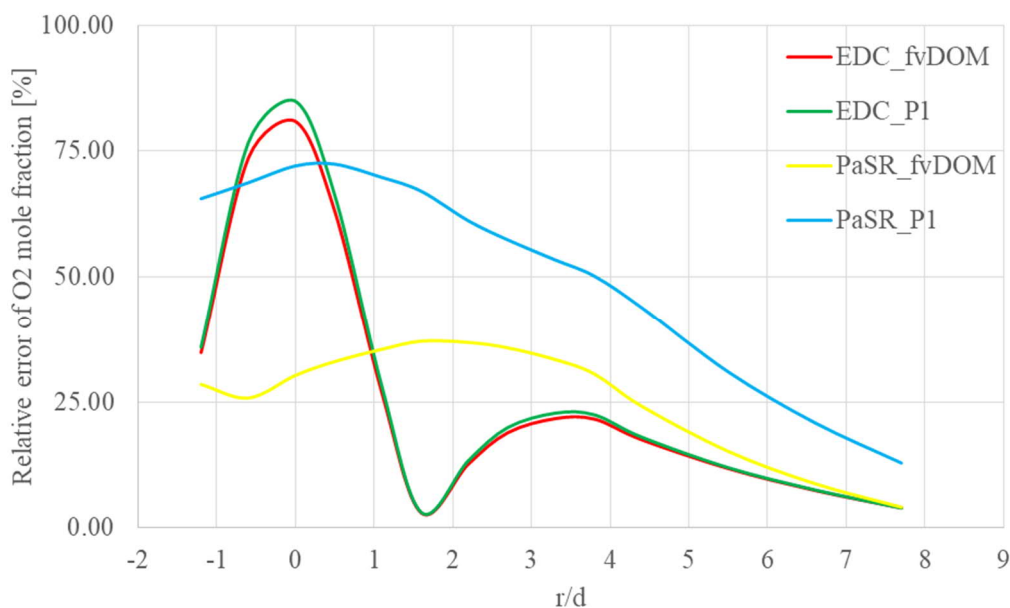


Figure 4.15. Sandia Flame D: Relative error of O₂ mole fraction at x/d=45.

In Figure 4.14, EDC cases are more accurate in temperature prediction for the whole radius than PaSR cases. For O₂ mole fraction in Figure 4.15, error is higher for EDC cases at the center of the flame but radially further EDC becomes more accurate than PaSR. All things considered, EDC models give more accurate results for the Sandia Flame D case and for EDC radiation model does not have significant effect on the results. EDC and P1 are both simpler and easier to use compared to PaSR and fvDOM with few or none adjustable parameters. With simpler models simulations can faster and more robust. Therefore, EDC and P1 are chosen for combustion and radiation sub-models respectively.

To gain some perspective into the test simulations, the results are compared from another study from Lysenko et al. (2014). In Figure 4.16 and Figure 4.17, the profiles of temperature and O₂ are compared between results from Lysenko et al. and this thesis at axis of symmetry. In work of Lysenko et al. case name “ke-EDC-GRI3” has same sub-models as case “EDC_P1” in this section. Simulation results of this thesis are shown in same units as in study from Lysenko et al.

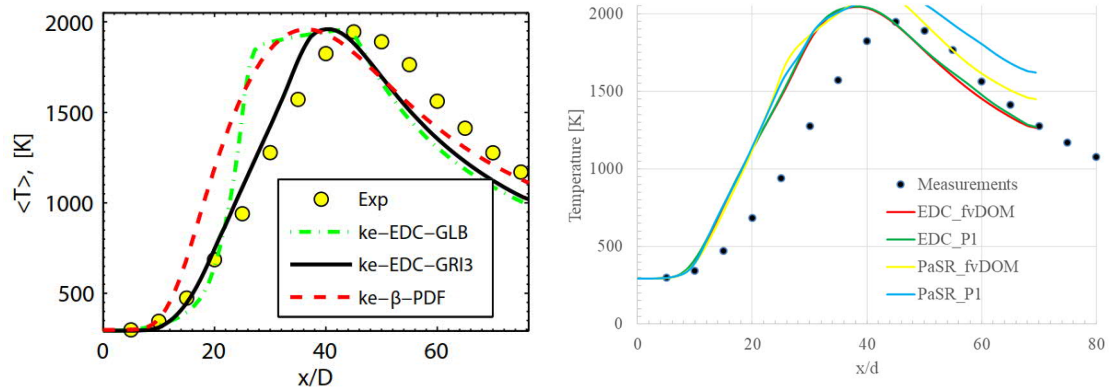


Figure 4.16. Temperature profile at axis of symmetry from Lysenko et al. (left) and simulations in this thesis (right). (Lysenko 2014, 680)

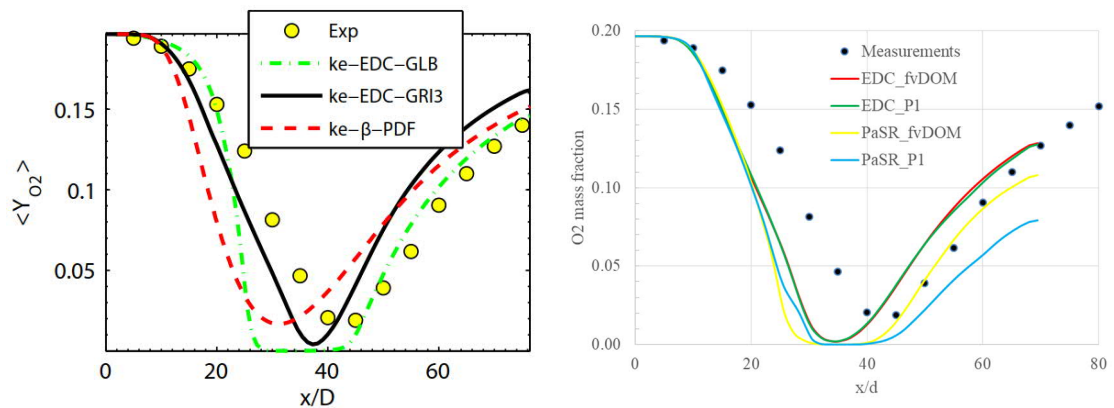


Figure 4.17. O₂ mass fraction profile at axis of symmetry from Lysenko et al. (left) and simulations in this thesis (right). (Lysenko 2014, 680)

In Figure 4.16 and Figure 4.17, left side shows the results from Lysenko and right side from simulations in this section. From figures, it can be said that simulation results seem to be closer to the experiments in study from Lysenko et al. Maximum temperature is in same level in study from Lysenko and results of this section have higher maximum temperature than measured. However, result plots from Lysenko and from this section have similar shape. Behavior of increasing and decreasing temperature and O₂ profiles is captured. Both simulations predict the maximum temperature to occur closer to the burner inlet than in the experiments. Similarly, the minimum point of O₂ mass fraction is predicted closer to the burner inlet.

Two most significant differences between work of Lysenko and results of this thesis are between mesh and GRI3.0 kinetics. Both meshes are structured type and well refined around axis of symmetry but there might still be differences that affect the results. GRI3.0

kinetics library used in this thesis neglected the reactions of nitrogen while full GRI3.0 library was used in simulations from Lysenko. Full GRI3.0 describes the combustion reactions more realistically when effect of nitrogen is also taken into account and that might increase the accuracy of the results from Lysenko compared to results from this thesis.

5 DESCRIPTION OF THE CFD MODEL FOR THE PROCESS FURNACE

This chapter describes the process furnace case in detail. Key aspects included in the process furnace geometry are shown and boundaries of the geometry are highlighted. Meshes used in this thesis are shown, creation methods are described and their different purposes in the simulation are explained. Boundary conditions specify the compositions of the inlet streams and modelling methods of different boundaries. Different steps performed during the simulation are described and all of the different cases calculated for this thesis.

5.1 Computational domain of the process furnace

The simulated process furnace has four burners attached to the floor. The furnace is cubical and it is geometrically divided into four equally sized upright rectangular compartments. Each compartment has a burner attached to the center of the floor. In between the compartments, there are tube bundles on all four sides. Therefore, around one burner there are two tube bundles near the outer walls and two bundles in between the compartments. There are no walls between the burners and therefore tube bundles between the burners see the flames from both sides. Each furnace compartment has its own exhaust pipe leading exhaust gases to the common convection section.

Computational domain in this work is limited to one burner section (compartment) of the furnace as the geometry is symmetrical between the burner sections. The burner section will be limited to inner surfaces of two outer walls of the furnace, two symmetry walls between the sections, furnace floor, and burner outlets and top of the exhaust pipe. Geometry is created with SpaceClaim 19.0. The computational domain is shown in Figure 5.1.

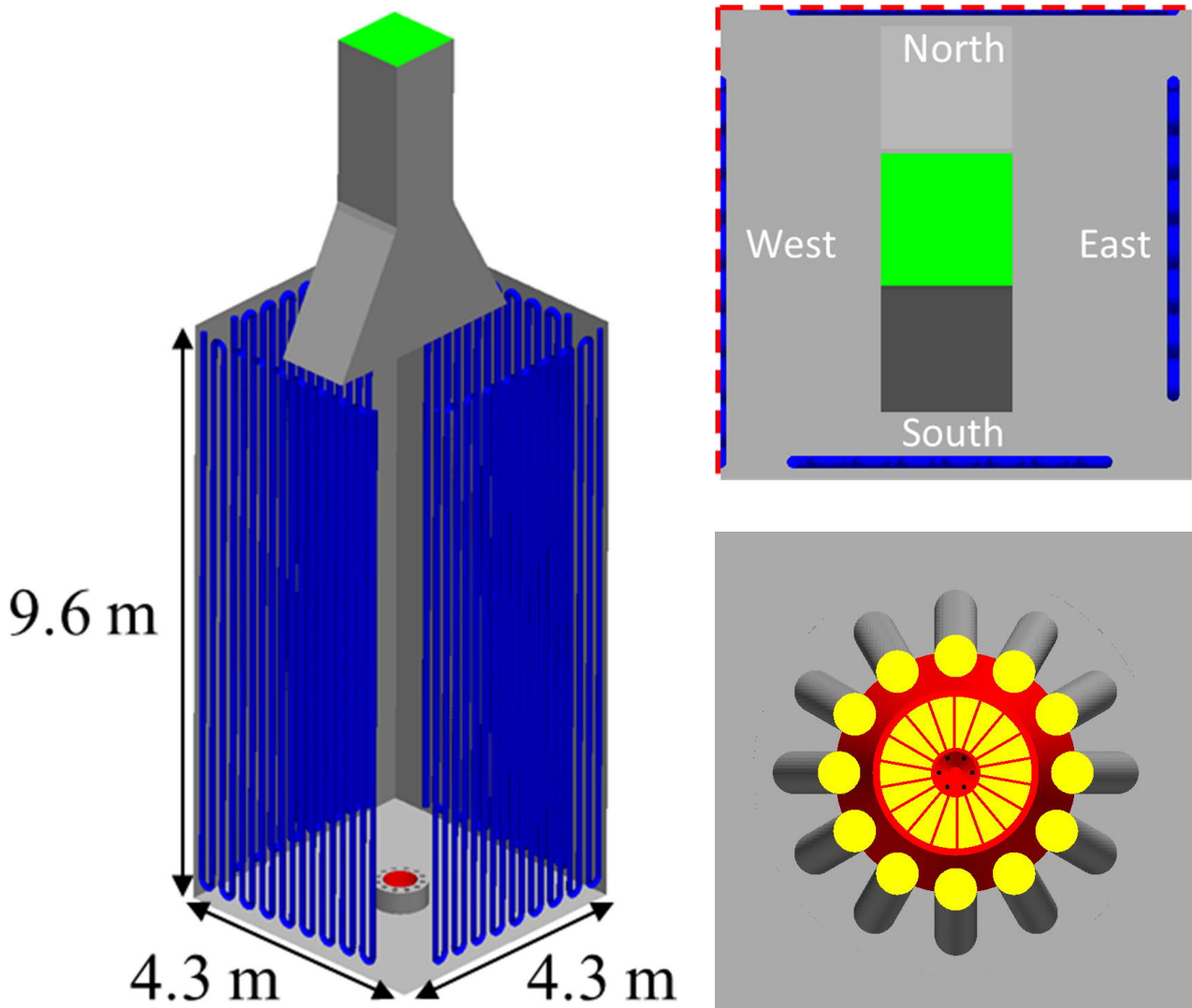


Figure 5.1. Whole computational domain (left picture), top view of the domain (right top picture) and enlargement of the burner from the bottom (right bottom picture).

In Figure 5.1, whole domain is shown at the left picture. Symmetry walls and roof of the combustion chamber has been hidden to show the insides of the furnace. Tube walls are highlighted with blue color, burner walls with red at the bottom and outlet with green at top of the exhaust pipe. At the top right corner picture is a view from above the furnace to illustrate the arrangement of the tube bundles and their naming by cardinal directions. Only half of the tube bundles are taken into consideration at symmetry walls (north and west) since other half belongs to other burner section based on symmetry. Locations of the symmetry walls are highlighted with red dashed line. At the bottom right corner is the enlargement of burner arrangement. Small black dots in the center are fuel gas inlets and primary air inlet is in yellow around them in circular sectors. In reality, the process

furnace has inlet guide vanes at primary air inlet that generate swirl to the primary air flow but in this work they were left out to reduce mesh size. Instead, velocity boundary condition is given to primary air inlet that creates swirling flow with same angle by axial and rotational velocity components. Secondary air inlets are also in yellow at the tube ends around the burner. These simplifications were also made in previous study of this process furnace with Fluent and are applied in this work as well.

5.2 Computational mesh of the furnace

Geometry of computational domain is discretized into small 3D elements called cells. This procedure is called meshing as it creates computational mesh. All of the governing equations are solved within each cell in the mesh and results affect the neighboring cells. Meshing is done with meshing program called Ansys Meshing 19.0 using the CutCell mesher. Mesh utilizes different shaped cells to fill out the geometry and capture shape of the geometry and the most common cell types are hexahedrons and tetrahedrons. Two different meshes were utilized during simulations.

- First geometry consisted only burner geometry and flat walls and symmetry surfaces without any tubes. This geometry is used to calculate initial flow conditions for cold flow and reacting radiating flow. Purpose is to decrease computational time by simulating stable flame without radiation and heat transfer to tube bundles. This flame can then be used to initialize calculations with finer mesh to reach the final result of simulations. Mesh was made simple and coarse to save computational time.
- Final solution and heat transfer is calculated with a finer mesh. Internal cuts of both meshes are shown in Figure 5.2.

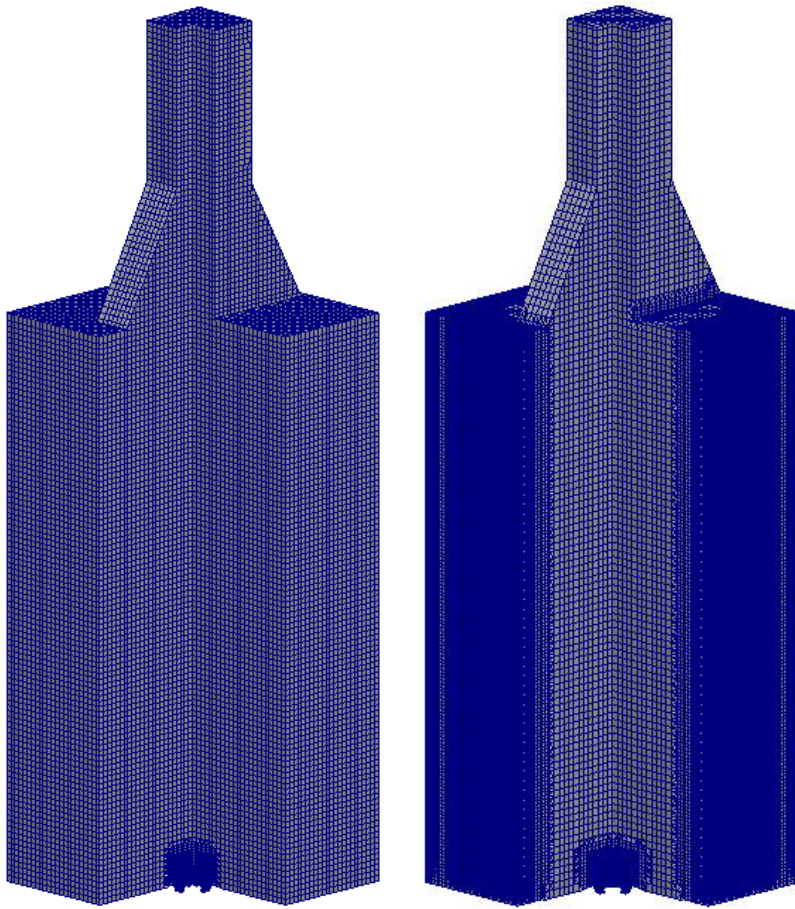


Figure 5.2. Coarse mesh (left picture) and fine mesh (right picture).

In Figure 5.2, coarse mesh has refinement only at burner region where the inlets are located. Finer mesh has refinement also on the tube surface near the walls. Total amount of elements are 328 000 in coarse mesh and 2 374 000 in fine mesh. Cell edge lengths were in the order of 10^{-3} m to 10^{-1} m with both meshes. Addition of tube surfaces to the fine mesh case increases significantly the total number of elements. Enlarged view from the bottom section of the furnace with both meshes is show in Figure 5.3.

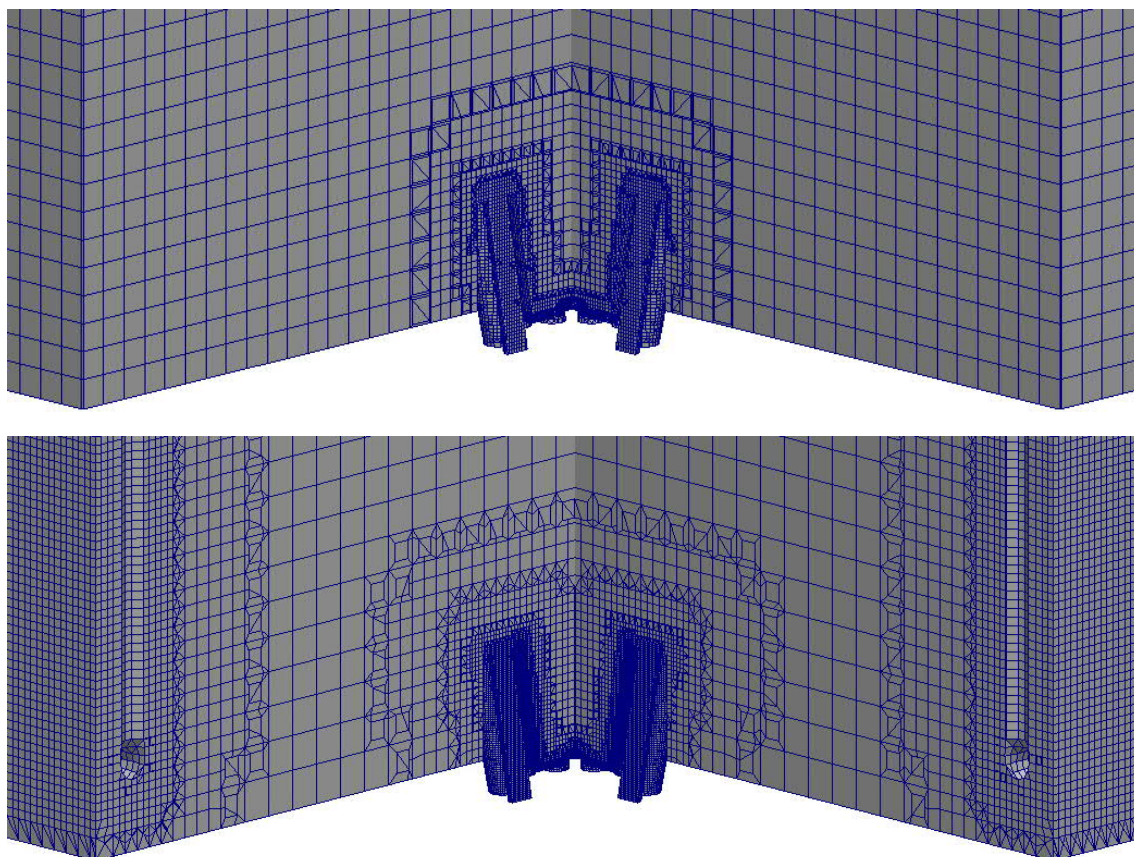


Figure 5.3. Enlarged view from the furnace mesh bottom with coarse mesh (top picture) and fine mesh (bottom picture).

It can be seen from Figure 5.3, that refinement has been increased in fine mesh at burner region and near the tube bundles.

5.3 Boundary conditions and used models in the furnace simulation

Boundary conditions define variable values on domain boundaries (inlets, outlet and walls). On the other hand, the Navier-Stokes equations require an initial state and specific constraints during calculation. All variables at every boundary and in the domain needs to be defined at begin of the simulation before the calculation can start. Fuel gas is left overs from refining process and its composition changes constantly based on process conditions in the refinery. In this work, the composition of fuel gas is simplified to combination of CH_4 and C_3H_8 . Boundary conditions for the process furnace case are the same as previous Fluent simulation done for this furnace and are listed in Table 5.1.

Table 5.1. Boundary conditions for process furnace.

Variable	U		p [kPa]	T [°C]	CH ₄ [mol-%]	C ₃ H ₈ [mol-%]	O ₂ [mol-%]	N ₂ [mol-%]
	Boundary condition type	Value						
inlet_FG	flowRate- InletVelocity	0.089 kg/s	zG	30	43.11	56.89	0	0
inlet_PA	cylindrical- InletVelocity	16.6 m/s 991 rpm	zG	293	0	0	20.7	79.3
inlet_SA	flowRate- InletVelocity	0.838 kg/s	zG	293	0	0	20.7	79.3
outlet	pressureInlet- OutletVelocity		100	zG	zG	zG	zG	zG
wall	noSlip		fixedFlux- Pressure	zG	zG	zG	zG	zG
wall_tube	noSlip		fixedFlux- Pressure	externalWallHeat- FluxTemperature	zG	zG	zG	zG

FG=fuel gas, PA=primary air and SA= secondary air

In Table 5.1, cylindricalInletVelocity at inlet_PA gives swirling velocity boundary condition. Velocity profile has axial and radial components with rotational speed which are fixed around specified axis and its origin. Purpose is to create swirling flow from the primary air inlet to mimic the actual inlet guide vanes. FlowRateInletVelocity means that velocity boundary condition is given as mass flow rate. ExternalWallHeatFluxTemperature is temperature boundary condition which allows to use heat transfer coefficient at surface with ambient temperature at other side of the boundary. This boundary conditions mimics the heat transfer from the tube surfaces to the fluid inside the tubes: in this work it fixes the temperature of the hydrocarbon stream in the tubes. FixedFluxPressure is similar to zeroGradient but it takes body forces such as gravitation into account and adjusts gradient at the boundary. Symmetry walls at north and west have boundary condition called symmetry for every variable. Symmetry means that normal gradients and normal velocity at the boundary is zero. (OpenCFD 2018.)

Tube wall boundary condition has heat transfer coefficient of 1200 W/m²K. This heat transfer coefficient represents external convective heat transfer coefficient, which simulates heat transfer from the inner tube surface to the fluid. Value of the coefficient is obtained from separate simulation with FRNC5-program. Fluid temperatures at other side of the tubes are assumed from the process data to be 350 °C for north and west, 401 °C for east and 434 °C for south tube bundle. Heat transfer resistance of the pipe metal and

possible fouling are neglected. Domain is initialized in temperature of 27 °C, pressure of 100 kPa and filled with air (79 % of N₂ and 21 % of O₂).

GRI3.0 reaction kinetics library that holds coefficients for 325 Arrhenius reactions for 53 species. Development of GRI3.0 was sponsored by Gas Research Institute until 2000 when work was discontinued. GRI3.0 is optimized for natural gas combustion and it uses thermochemical data based on NASA polynomial coefficients. GRI3.0 mainly focuses on reactions of lighter hydrocarbons (species with one or two elements of C) and heavier hydrocarbons are approximated with propane (C₃H₈) with simpler reactions that are not as realistic as methods used with lighter hydrocarbons. (Smith 2002.) Simplified version of the GRI3.0 is used in this thesis where all of the reactions of nitrogen are neglected. Therefore reaction library is reduced to 36 species and 219 reactions.

5.4 Running the simulation

Simulation is done with LTS method the same that was used with Sandia case and it aims to reach a steady state solution. Simulation is started as cold flow, meaning that chemical reactions are turned off. Flow has all of the components which are listed in boundary conditions but they are not able to react. When the cold flow field has been simulated so far that enough fuel and air has mixed in the furnace, the mixture is ignited. Ignition is done by updating a high temperature field inside the domain in the same time that the chemical reactions are turned on. Rapid increase in temperature for one iteration ignites the mixture inside the domain. Iterations are continued until the flame shape starts to stabilize. Finally radiation can be turned on to apply realistic heat transfer from the flame. Simulation is completed when solution converges with radiation on. Convergence is monitored with mass balance, temperature and O₂ values at outlet. Simulation result from the coarse mesh simulation is interpolated to finer mesh using the mapFields utility of OpenFOAM and heat transfer boundary condition is activated for tube bundles which includes convection and radiation. Simulation is ran to reach convergence and an additional convergence criteria at this stage is heat transfer to the tube bundles.

5.5 Simulation cases

The different simulation cases and their key differences are presented in this section. All of the cases which are investigated in this thesis are shown in Table 5.2. Boundary conditions described in section 5.3 apply for cases OF_{coarse} and $OF_{\text{detailed},1}$, and case specific changes are described separately.

Case OF_{coarse} is done to simulate cold flow and reacting flow profiles using the coarse mesh, which does not include the heat transfer tubes at all. The reacting flow profile is used in initialization of the detailed cases having fine mesh with radiation and heat transfer.

Case $OF_{\text{detailed},1}$ is ran as the base case where boundary conditions from Fluent simulation are tested in OpenFOAM solver and selected sub-models. It is a reacting flow simulation with heat transfer and radiation to the tubes.

Case $OF_{\text{detailed},2}$ is done to inspect the oxygen consumption of the GRI3.0 reaction library. Air mass flow is increased from 1.61 kg/s to 2.0 kg/s to see if there would be more excess oxygen left at the outlet. Air flow is divided in same proportions than in $OF_{\text{detailed},1}$ to primary and secondary inlets.

Case $OF_{\text{detailed},3}$ is done to verify the function of velocity boundary condition at primary air inlet. OpenFOAM's method to determine mass flow from inclined velocity profile is questioned based on the constant deficit in the simulation mass balance and low value of O_2 at the outlet. It is suspected that OpenFOAM calculates mass flow only from the velocity component that is normal to the boundary. This means that mass flow would be smaller than intended because velocity for the inlet boundary condition is determined as magnitude, taking into account for all of the velocity components. Axial velocity of 16.6 m/s in $OF_{\text{detailed},1}$ equals to 0.617 kg/s of mass flow when accounting only velocity normal to the boundary and difference between desired mass flow (0.769 kg/s) is 0.152 kg/s. Difference between two inlet velocity conditions is similar compared to average error in OF_{coarse} and $OF_{\text{detailed},1}$ simulations which has error of 0.154 kg/s and 0.160 kg/s respectively. In $OF_{\text{detailed},3}$ axial velocity is set as 20.7 m/s to match the desired mass flow with just axial component and rotational speed 1235 rpm to maintain the direction of the swirling flow.

Case $OF_{2\text{reactions,c}}$ is done to simulate reacting flow in coarse mesh with simplified 2 reaction equation kinetics to serve as initialization for fine mesh simulation.

Case $OF_{2\text{reactions}}$ is done to compare different reactions kinetics. In this case, only two one-step reaction equations are used to describe the combustion of two fuel species. Detailed cases use more complex library of GRI3.0 which is not necessarily available for every combustion case with different fuels. Therefore, it is of interest to compare different reaction kinetics and differences in results.

Case Fluent is done previously from this same process furnace and its results are compared to OpenFOAM results. Results are intended to give background for OpenFOAM results and not for direct comparison since some sub-models are different in the OpenFOAM simulation. It is also interesting to see how well boundary conditions in Fluent translate to OpenFOAM simulations.

Table 5.2. Simulated cases.

Case name	Mesh	Reaction kinetics	Combustion	Radiation	Description
OF _{coarse}	Coarse	GRI 3.0	EDC	-	Reacting flow simulation and initialization for other OF cases. No heat transfer or radiation
OF _{detailed,1}	Fine	GRI 3.0	EDC	P1	Reacting flow simulation with heat transfer and radiation. Boundary conditions as described before and same as in Fluent case.
OF _{detailed,2}	Fine	GRI 3.0	EDC	P1	Same case as OF detailed ₁ but total air mass flow increased to 2 kg/s. Divided with same ratio as before to primary and secondary inlets.
OF _{detailed,3}	Fine	GRI 3.0	EDC	P1	Same case as OF _{detailed,1} but primary air feed adjusted to verify the function of velocity boundary condition.
OF _{2reactions,c}	Coarse	2 global reactions	EDC	-	Same case as OF _{coarse} but GRI 3.0 reaction kinetics is replaced by two global one-step reaction equations for methane and propane combustion.
OF _{2reactions}	Fine	2 global reactions	EDC	P1	Same case as OF _{detailed,1} but GRI 3.0 reaction kinetics is replaced by two global one-step reaction equations for methane and propane combustion.
Fluent	-	2 global reactions	EDM	DOM	Previously done simulation which is used as comparison and source for boundary conditions.

6 SIMULATION RESULTS

Simulation results are presented and discussed in this chapter. Steady-state results are averaged over last 10 000 iterations with 200 step intervals. Different aspects of the simulation such as convergence, duration and accuracy compared to Fluent simulation and measurements are considered in the discussion. Convergence tells about the stability of the simulation and how trustworthy the results are. Duration helps to determine the practical feasibility of the used simulation methods and models. Comparison of the results to Fluent simulation gives perspective and background to evaluate how realistic results are. Measurements give knowledge how close the simulation results can get from the experimental data.

Figures of all of the simulation results are listed in Appendix III: Process furnace simulation results and overview of the results from all cases is shown in Table 6.1. Process data column shows the measured data that simulations aim to achieve. In the following sections, the cases listed in Table 6.1 are explained in more detail.

Table 6.1. Summary of the simulation results.

Case	Process data	OF _{coarse}	OF _{detailed,1}	OF _{detailed,2}	OF _{detailed,3}	OF _{2reactions,c}	OF _{2reactions}	Fluent
Mass flow error [%]		9.1	9.4	4.6	7.0	6.1	7.9	0.04
Flue gas temperature at outlet [°C]	778.5	2123.4	748.9	878.4	766.2	2145.6	697.5	797.2
O ₂ mole fraction at outlet [-]	0.028	0.010	0.001	0.001	0.001	0.014	0.013	0.027
Heat transfer to tubes [MW]	3.05	-	3.40	4.50	3.41	-	3.21	3.07

Simulation results are compared to experimental measurements from the process furnace. Measurement locations are at exhaust pipe and North and South side tube surfaces at heights of 3 m and 9 m from the furnace floor. Locations and values of measured variables are illustrated in Figure 6.1.

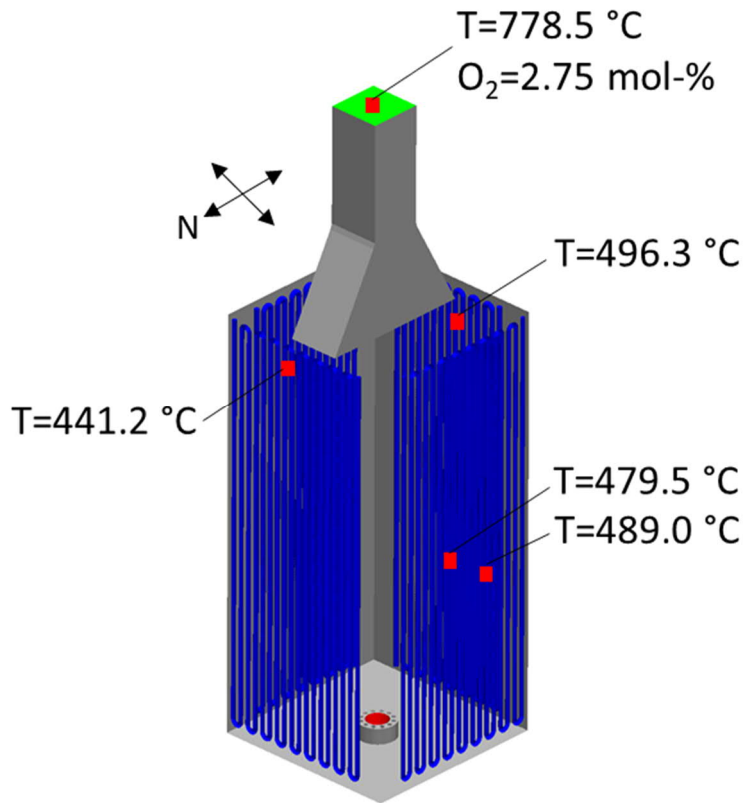


Figure 6.1. Time averaged measurement data from the process furnace for validation of simulation results.

6.1 Base case simulation results

Base case simulation includes the $\text{OF}_{\text{coarse}}$ and $\text{OF}_{\text{detailed},1}$ simulations since they are performed first with similar boundary conditions with Fluent and form the basis for further cases.

6.1.1 Convergence

Convergence was monitored in terms of mass balance, outlet temperature and flue gas composition. Mass balance was monitored at the outlet and its values compared to sum of the inlet streams. Time averaged values calculated at the outlet are show in Table 6.2.

Table 6.2. Average mass balance of simulations in coarse and fine mesh.

Case	Outlet average [kg/s]	Outlet SD [kg/s]	Input [kg/s]	Relative error [%]
OF _{coarse}	1.542	0.038	1.696	9.1
OF _{detailed,1}	1.536	0.357	1.696	9.4

SD = standard deviation

Table 6.2 shows that mass balance did not convergence during simulations and outlet mass flow is on average over 9 % smaller than the sum of input streams. Mass balance is therefore not well conserved in the simulations which should be kept in mind when reading the results. While the results are not precise they can still be studied to show the behavior of the reacting flow with different boundary conditions. Standard deviation (SD) shows that simulations in OF_{coarse} case have order of magnitude smaller deviation in outlet mass flow. Addition of heat transfer and radiation in OF_{detailed,1} case leads to higher instability at the outlet and cause larger deviations to the mass balance.

Besides the mass balance, the outlet composition is compared to results from calculations of stoichiometric reactions of methane and propane, see Table II in Appendix II. Values of CO₂, H₂O, O₂ and N₂ are used in comparison since they are available from stoichiometric calculations. Comparison is shown in Figure 6.2 and values used are listed in Table 6.3 for closer inspection.

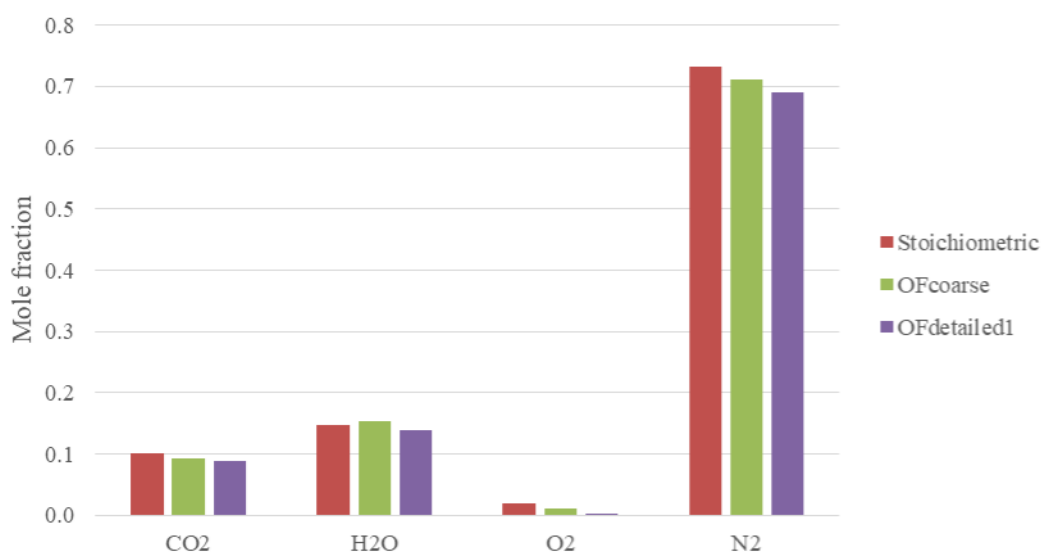
**Figure 6.2.** Average mole fractions of flue gas components for base case at outlet.

Table 6.3. Average mole fractions of flue gas components for base case at outlet.

Case	CO ₂	H ₂ O	O ₂	N ₂	Stoic. sum	Others sum	Total sum
Stoichiometric	0.100	0.147	0.020	0.732	0.999	-	0.999
OF _{coarse}	0.093	0.155	0.010	0.710	0.968	0.030	0.998
OF _{detailed,1}	0.089	0.139	0.001	0.691	0.920	0.068	0.988

In Table 6.3, stoichiometric components of the flue gas are summed up to one value which can be used to see how complete the combustion is at the end of the simulation. Share of other components that are not included in the stoichiometric combustion products are presented to illustrate the amount of intermediate combustion products in the flue gas. Total sum of flue gas components show how large portion of the different flue gas components are presented in this section.

In Table 6.3, OF_{coarse} and OF_{detailed,1} have lower CO₂ values and significantly lower O₂ fractions than stoichiometric results. The flue gas O₂ mole concentration 0.027 is based on process data which is slightly higher than stoichiometric (0.020) because of the leakages from surrounding air to the furnace which increases the air content in the combustion. OF_{coarse} case does have higher H₂O fraction than in stoichiometric results, but since absolute content of H should not change in the simulation, this is due to higher concentration of other species with lower molar content. Combustion in OpenFOAM cases consumes more oxygen but produces less CO₂ as product. This would indicate that oxygen is consumed to production of intermediate components that do not react all the way to CO₂ and H₂O.

Four components in the Table 6.3 form the total composition (within rounding error) of flue gas in stoichiometric calculations, since reaction equations are considered to be single step and complete combustion reactions. OpenFOAM simulations use GRI3.0 reaction mechanism with 36 species and 219 reactions. GRI3.0 mechanism includes both forward and backward options for reactions and includes intermediate components created during combustion. Even though four components presented here account for major species in the flue gas, there are still some other intermediate components left. Majority of mole fractions of intermediate components in flue gas belong to CO, OH and H₂ in OF_{coarse} and

OF_{detailed,1} case. There is also some CH₄ left unburnt in OF_{detailed,1} case. Significant species that account for most of the mole fractions disregarded earlier are listed in Table 6.4.

Table 6.4. Average mole fractions of species from incomplete combustion for base case at outlet.

Case	CO	H ₂	OH	CH ₄	Others sum
OF _{coarse}	0.019	0.005	0.006	-	0.030
OF _{detailed,1}	0.038	0.017	-	0.013	0.068

In Table 6.4, mole fractions are not listed for species that have values smaller than used accuracy. Most noticeable thing in OF_{coarse} and OF_{detailed,1} cases is the high content of CO compared to O₂. OF_{coarse} case has CO fraction almost double to O₂ and OF_{detailed,1} case does not have significant amounts of O₂ left in the flue gas while CO fraction is double than in OF_{coarse} case. OF_{coarse} case has higher temperature field inside the furnace because there is no heat transfer to tubes. Higher temperature helps reactions to complete combustion into CO₂ and H₂O. Lower temperature field seems to limit the reactions and more species are left unburnt as intermediate components and more CO is produced. The current amount of oxygen supplied to the furnace with the modelling methods used is not sufficient to combust all of the hydrocarbons completely.

Next, conservation of the elemental components was investigated with elemental balance. Elemental balance was calculated as a ratio of between fuel (C and H) and oxidizer (O and N) mass components and from boundary conditions ratio is 0.055. Ratio is calculated as

$$\alpha = \frac{m_C + m_H}{m_O + m_N} \quad (6.1)$$

where α is the elemental ratio. When species at outlet were divided to elemental components, the elemental ratio, result was 0.064 and 0.093 for OF_{coarse} and OF_{detailed,1} respectively. Ratios at outlet are higher than inlet conditions which would suggest, that flue gas has smaller amount of oxidizer components at the outlet than at the inlet. Therefore conservation of the flue gas species is not fully maintained in the simulations.

The flue gas temperature at the model outlet was 2123.4 °C (neglecting heat transfer to the tubes) and 748.9 °C (3.40 MW of heat transfer to the tubes) for OF_{coarse} and $OF_{\text{detailed},1}$ case respectively. Standard deviation for outlet temperature was 2.8 °C and 18.6 °C for OF_{coarse} and $OF_{\text{detailed},1}$ case respectively. Based on experimental process data, temperature of the flue gas should be 778.5 °C at the outlet and adiabatic flame temperature was defined to be 2178.4 °C. Adiabatic flame temperature was calculated in OpenFOAM with utility called `mixtureAdiabaticFlameT`. This utility uses volume fractions of reactants and products with given initial temperature and pressure to calculate adiabatic flame temperature of the flue gas. Initial temperature was same as the air inlet temperature, 293 °C, and pressure was 100 kPa. Volume fractions of species were taken from stoichiometric calculations in Table II, assuming ideal gas and therefore mole fractions and volume fractions equal.

Temperature at the outlet is somewhat lower for both OF_{coarse} and $OF_{\text{detailed},1}$ case than estimated from experiments or by calculations. Temperature levels are still on comparable level with experimental data. In OF_{coarse} case, all of the CO did not combust and temperature level might be lower due to combustion being incomplete compared to calculated ideal value. In $OF_{\text{detailed},1}$ case, combustion is not fully completed either and another factor that affects the outlet temperature is heat transfer. If heat transfer is evaluated greater in the simulation than in reality it will decrease the temperature of flue gas.

6.1.2 Duration

Total duration of the simulation steady-state was 44 days and 15.5 hours from simulations of cold flow profile in the coarse mesh to final simulation with heat transfer and radiation in the fine mesh. Cold flow profile was simulated in the coarse mesh for approximately 70 000 iterations which took 1 day and 12.5 hours to complete. After that flow was ignited in the coarse mesh and calculated for approximately 360 000 iterations which took 11 days and 13 hours. Next, data about the flow was transferred to the fine mesh and simulated with heat transfer and radiation for 250 000 iterations which took 31 days and 14 hours.

Simulations with the coarse mesh were ran on 30 computational cores and the fine mesh simulations with 70 cores. Number of cores per simulation case was decided based on the number of cells in the mesh. Number of cells per core was aimed to be in order of tens of thousands. Dividing case to larger number of cores may not be beneficial if number of cells per core is low and data transfer between cores is high. Data transfer between the processors might start to limit the calculation speed of the cores.

In hindsight, duration of the simulation could have been reduced by transferring the data from coarse mesh to fine mesh a bit later, after heat transfer had been applied. Initial idea was to wait until reacting flow profile has stabilized in the coarse mesh simulation before the data transfer to fine mesh. Addition of heat transfer to the tube in fine mesh disrupts the flow field significantly, which defeats the purpose of having stable flow field in the first place. Heat transfer decreases the temperature field inside the furnace significantly and decreases the volume of the gas mixture. Based on the ideal gas law temperature drop increases density and decreases volume of the gas. Large temperature change caused flow to circulate inside the furnace and decreased the outflow from the domain. Stabilization of flow field takes substantial amount of time in the fine mesh. This suggests that some heat transfer should be applied earlier in coarse mesh simulation to decrease the need of simulation time and iterations in the fine mesh.

6.1.3 Results

Velocity field is shown for OF_{coarse} and $OF_{\text{detailed},1}$ in Figure 6.3. Height of the flame is significantly smaller with $OF_{\text{detailed},1}$ case than in OF_{coarse} case. Height of the flame depends on the reaction speeds of the species. Combustion reactions release heat which causes gas mixture to expand and expansion increases the flow velocity. With higher temperature in the OF_{coarse} case reactions are faster and accelerate the flow more than in $OF_{\text{detailed},1}$ case.

Outlet velocity is higher in OF_{coarse} case than the others because the density of the mixture is lower in higher temperatures. To achieve same outlet mass flow in OF_{coarse} and $OF_{\text{detailed},1}$ cases, outlet velocity has to be higher with lower density.

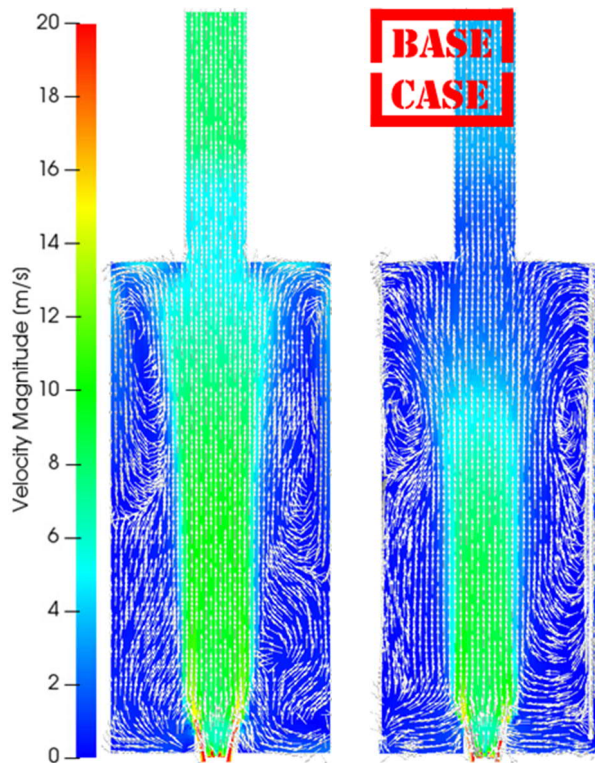


Figure 6.3. Average velocity profile at Z-normal plane for OF_{coarse} on the left, $OF_{\text{detailed},1}$ on the right.

Temperature field is shown for OF_{coarse} , and $OF_{\text{detailed},1}$ simulations in Figure 6.4. Temperature field in OF_{coarse} case is shown in different scale since the temperature levels are considerably higher because the walls are adiabatic. The size of the temperature profile of the flame is smaller in $OF_{\text{detailed},1}$ than the velocity profile, indicating that radiation transfers the heat out of the jet flame and decreases the flame length.

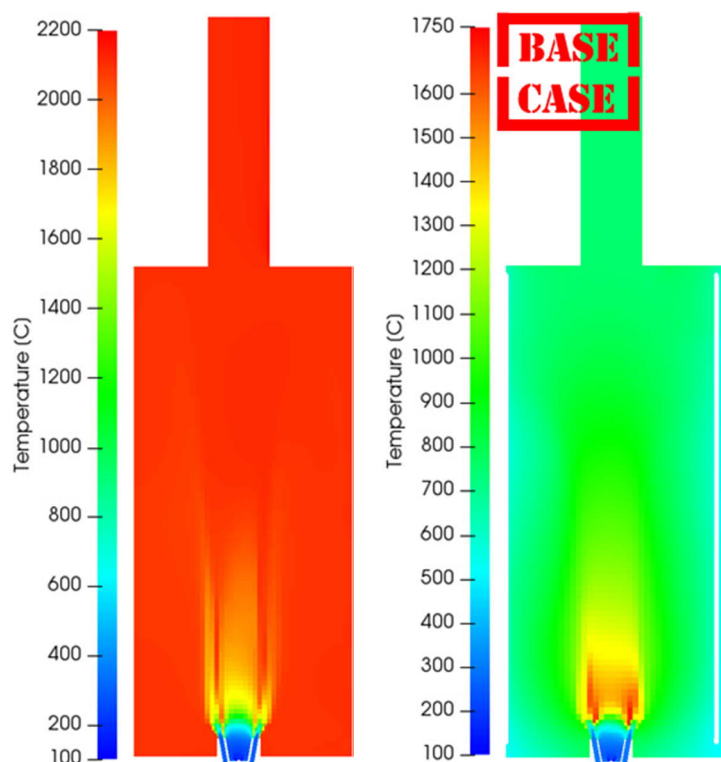


Figure 6.4. Average temperature profile at Z-normal plane for OF_{coarse} on the left, $OF_{detailed,1}$ on the right. Note the different scale for OF_{coarse} .

Oxygen field is shown for OF_{coarse} and $OF_{detailed,1}$ in Figure 6.5. Figures show that in OF_{coarse} and $OF_{detailed,1}$ cases oxygen is mostly consumed by the combustion. This affirms the earlier claims in convergence section 6.1.1, that amount of oxygen used in Fluent boundary condition is not enough for the more complex reactions of GRI3.0. In $OF_{detailed,1}$ case, oxygen is consumed faster than in OF_{coarse} case which is caused by the increase of mixing due to heat transfer to the tubes. Tubes itself change the flow patterns and temperature difference caused by the colder surface of the tubes introduces density differences inside the furnace. Fluid flow increases around the tubes as density differences cause heavier and cooler species to rotate downwards. This rotation increases the mixing inside the furnace and near the flame. Better mixing means that oxygen is consumed more effectively in combustion.

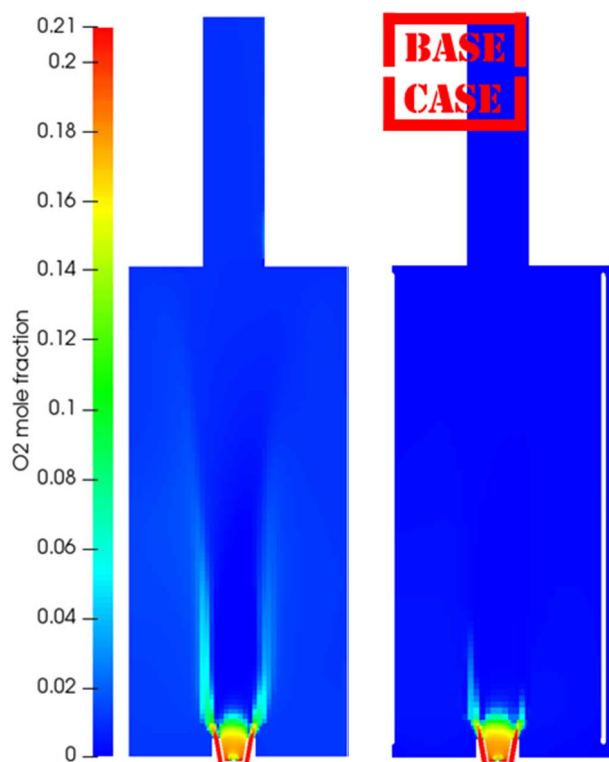


Figure 6.5. Average O_2 mole fraction field at Z-normal plane for OF_{coarse} on the left, $OF_{detailed,1}$ on the right.

6.2 Comparison of detailed reaction scheme results

In this section results of detailed reaction schemes cases $OF_{detailed,1}$, $OF_{detailed,2}$ and $OF_{detailed,3}$ are compared to each other. $OF_{detailed,1}$ acts as base case and effects of changes in air inflow are investigated with $OF_{detailed,2}$ and $OF_{detailed,3}$, see also Table 6.1.

6.2.1 Convergence

Mass balance of the detailed simulations are shown in Table 6.5. $OF_{detailed,2}$ has smaller error in the mass balance but the standard deviation is higher which means that solution is not more stable than in the base case. In $OF_{detailed,3}$ relative error in mass balance and standard deviation is in between two previous detailed cases but in this case outflow is larger from the domain than inflow. $OF_{detailed,3}$ case was done to investigate the boundary condition in primary air inlet and it can be said from the mass balance of the case that error in mass balance is not caused by the velocity boundary condition. Increase in air inflow caused outflow to increase as well and shows that error in mass balance cannot be fixed with velocity boundary condition alone.

Table 6.5. Average mass balances of detailed cases.

Case	Outlet average [kg/s]	Outlet SD [kg/s]	Input [kg/s]	Relative error [%]
OF _{detailed,1}	1.536	0.357	1.696	9.4
OF _{detailed,2}	1.992	0.406	2.089	4.6
OF _{detailed,3}	2.017	0.403	1.885	7.0

Mole fractions of species in the flue gas at outlet are shown in Figure 6.6 and detailed values in Table 6.6. When air flow is increased in OF_{detailed,2} for primary and secondary inlets, fractions of CO₂ and H₂O are closer to stoichiometric values at outlet than in other detailed cases. Increased air flow results increase in products of complete combustion. However, excess air is still minimal and has not increased compared to base case. Results from OF_{detailed,3} do not significantly differ from results of OF_{detailed,1} with flue gas composition, so increase in primary air inflow in OF_{detailed,3} does not impact the combustion products.

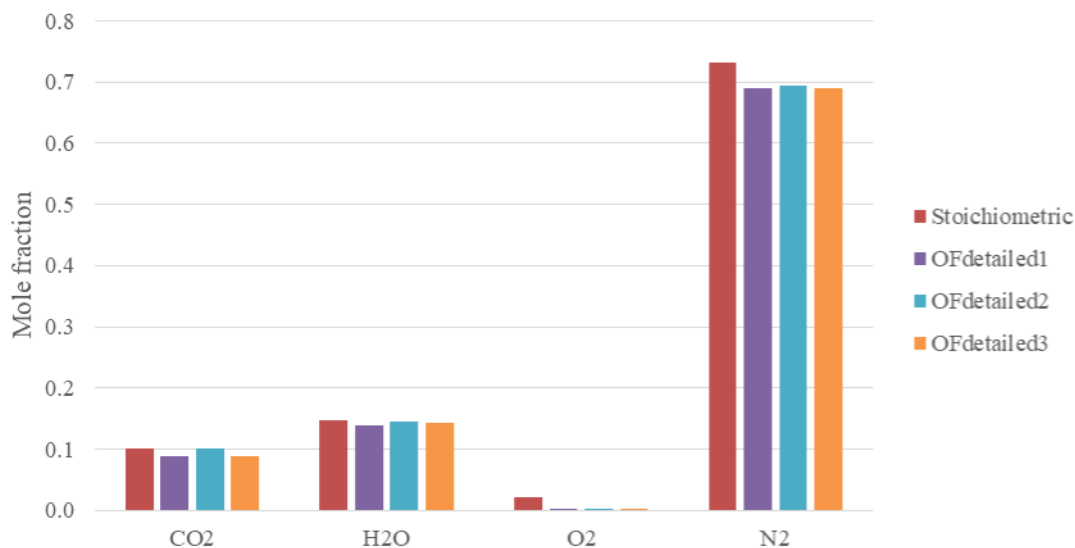
**Figure 6.6.** Average mole fractions of the flue gas components of detailed cases at outlet.

Table 6.6. Average mole fractions of flue gas components of detailed cases at outlet.

Case	CO ₂	H ₂ O	O ₂	N ₂	Stoic. sum	Others sum	Total sum
Stoichiometric	0.100	0.147	0.020	0.732	0.999	-	0.999
OF _{detailed,1}	0.089	0.139	0.001	0.691	0.920	0.068	0.988
OF _{detailed,2}	0.100	0.144	0.001	0.694	0.939	0.053	0.992
OF _{detailed,3}	0.087	0.143	0.001	0.690	0.921	0.071	0.992

Comparison of intermediate products of combustion in the detailed cases is shown in Table 6.7. Sum of intermediate components is smaller in OF_{detailed,2} than in the other cases. Fractions of CO and H₂ have decreased as they are combusted to CO₂ and H₂O due to increased combustion air flow rate. Smaller increase in primary air inflow in OF_{detailed,3} resulted in increase of intermediate component fractions. Difference between cases was that in OF_{detailed,2} air flow was also increased in secondary inlet which feeds air closer to the edge of the jet near region.

Table 6.7. Average mole fractions of species from incomplete combustion for detailed cases at outlet

Case	CO	H ₂	CH ₄	Others sum
OF _{detailed,1}	0.038	0.017	0.013	0.068
OF _{detailed,2}	0.028	0.010	0.015	0.053
OF _{detailed,3}	0.040	0.020	0.011	0.071

Elemental balance as ratio of fuel and air components is 0.097 and 0.103 for cases OF_{detailed,2} and OF_{detailed,3} respectively, which shows similar problem with conservation of species in the simulations than in the base case and large difference with reference at inlet boundary (0.055).

The outlet flue gas temperature were 878.4 °C (4.50 MW of heat transfer to the tubes) and 766.2 °C (3.41 MW of heat transfer to the tubes) for OF_{detailed,2} and OF_{detailed,3} simulations respectively. Increase in air inflow lead to increase in the flue gas outlet temperature in both cases compared to base case (748.9 °C). In OF_{detailed,2}, where increase in air flow was larger, both flue gas temperature and heat transfer increased significantly

while in $OF_{\text{detailed},3}$ changes were more minor. Results of $OF_{\text{detailed},2}$ are considerably higher when comparing them to the experimental process data of outlet flue gas temperature (778.5 °C) and heat transfer to the tubes (3.05 MW)

6.2.2 Duration

$OF_{\text{detailed},2}$ simulation was ran for 45 000 iterations with 58 cores which took 6 days and 17.5 hours of real time. $OF_{\text{detailed},3}$ simulation was ran for 29 000 iterations with 46 cores which took 9 days and 1.5 hours of real time. Result from $OF_{\text{detailed},1}$ was used as initialization for both simulations. Differences in number used cores between the different cases were caused by practical reasons when cases were distributed for different computers for calculations. Computers have varying amount of cores available and data transfer from one computer to another was not desired since it might become a bottleneck in the calculations. Results from a new case with modified boundary conditions can be can be obtained after approximately one week depending on amount of utilized computational cores.

6.2.3 Results

Velocity profiles of detailed cases can be seen in Figure 6.7. Increase in air mass flow increases flow velocity at outlet and flame height in cases $OF_{\text{detailed},2}$ and $OF_{\text{detailed},3}$. Even though increase in airflow is approximately 0,2 kg/s in $OF_{\text{detailed},3}$ and 0,4 kg/s in $OF_{\text{detailed},2}$ compared to base case, the flame height does not increase significantly in $OF_{\text{detailed},3}$ while $OF_{\text{detailed},2}$ has much taller flame. Increase in secondary air flow seems to have larger effect on flame height than primary air. Swirling air flow from primary air inlet does not create as large increase in axial velocity than inclined secondary air feeds. Swirl is used to stabilize the flame which often reduces the flame, this effect is illustrated in Figure 2.1.

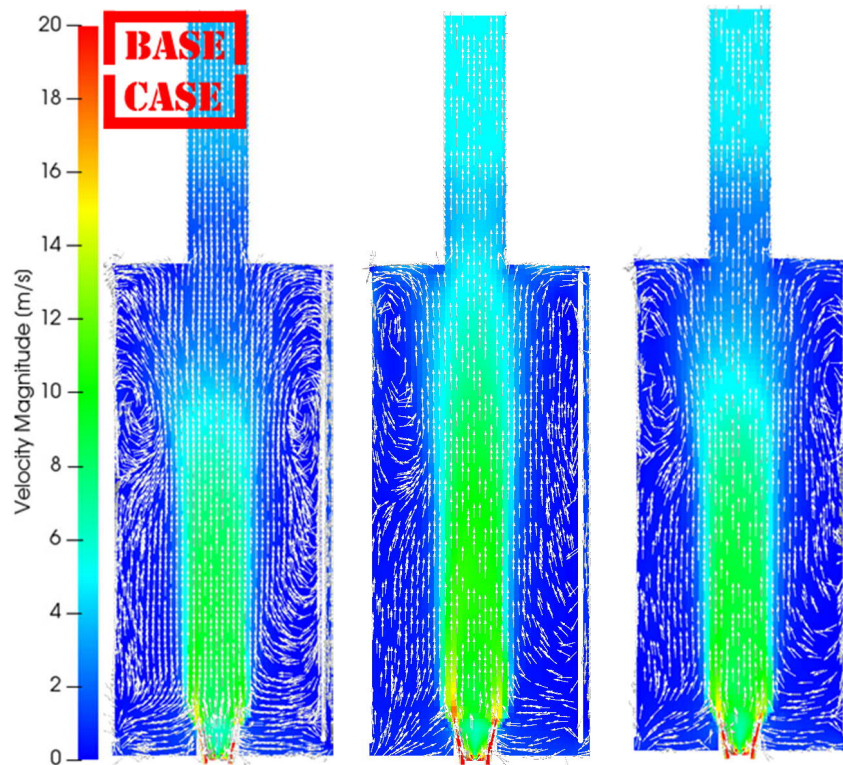


Figure 6.7. Average velocity profile at Z-normal plane for $OF_{\text{detailed},1}$ on the left, $OF_{\text{detailed},2}$ in the middle and $OF_{\text{detailed},3}$ on the right.

Temperature field inside the flame in cases $OF_{\text{detailed},2}$ and $OF_{\text{detailed},3}$ are higher than in the base case as can be seen in Figure 6.8. In $OF_{\text{detailed},2}$ height of the flame temperature field has also increased while height of the flame temperature profile is rather same $OF_{\text{detailed},3}$ as in base case. Results indicate that addition of secondary air flow increases the height of flame and addition of primary air flow increases the temperature inside the flame.

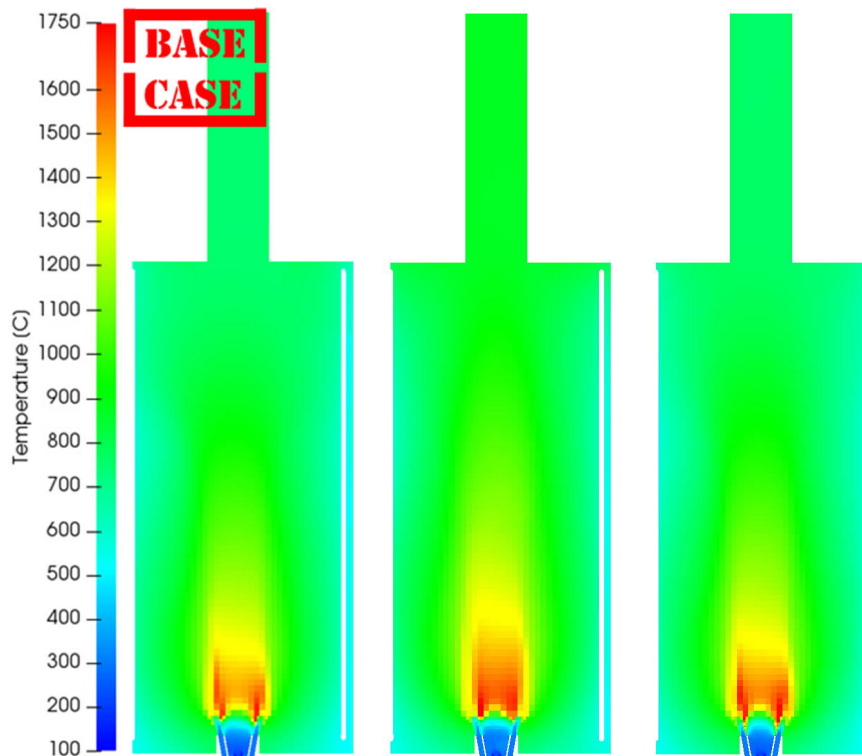


Figure 6.8. Average temperature profile at Z-normal plane for $OF_{\text{detailed},1}$ on the left, $OF_{\text{detailed},2}$ in the middle and $OF_{\text{detailed},3}$ on the right.

Oxygen fields in Figure 6.9 for cases $OF_{\text{detailed},2}$ and $OF_{\text{detailed},3}$ are similar to the base case. Only with $OF_{\text{detailed},2}$ trails of higher oxygen concentration reach higher from the secondary air inlets than in other cases. There is constant asymmetry in the oxygen profiles of all detailed cases where trails of higher oxygen concentration are higher on the symmetry wall sides (North and West) than on the other sides (East and South) of the furnace. Velocity profiles in Figure 6.7 show that on the symmetry wall side (left side of the furnace in the pictures) velocity vectors are pointing upwards uniformly near the flame while on the opposite side vectors show circulation between the flame and tubes. This circulation increases the mixing of oxygen and shortens the trail of higher concentration compared to symmetry side of the furnace. It should be noted that symmetry boundary condition sets normal component of the velocity to zero on the symmetry surface and can affect the circulation on the symmetry walls of the furnace.

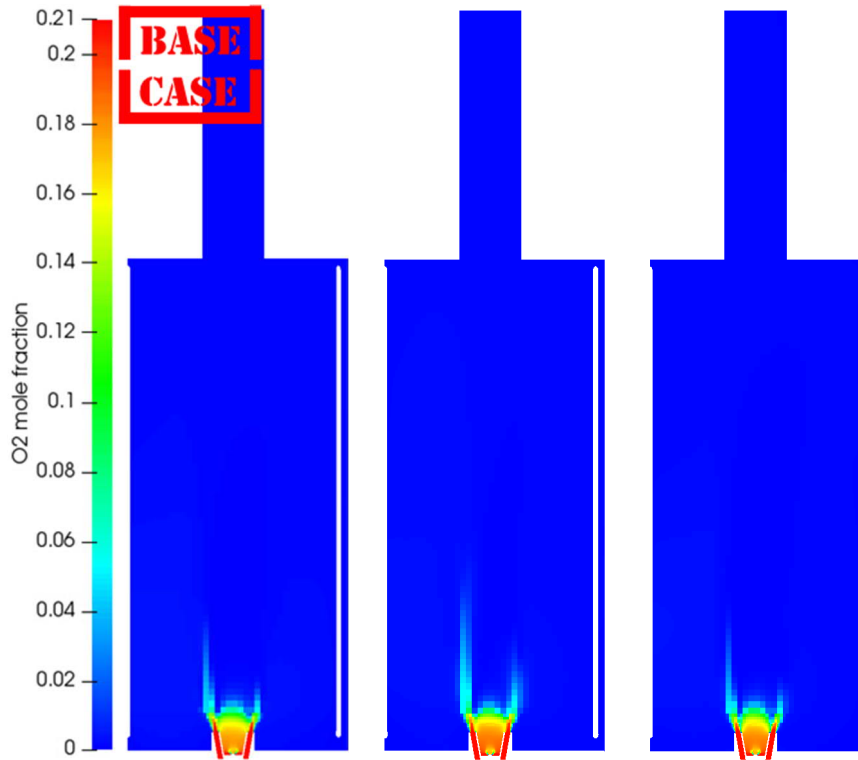


Figure 6.9. Average O₂ mole fraction field at Z-normal plane for OF_{detailed,1} on the left, OF_{detailed,2} in the middle and OF_{detailed,3} on the right.

6.3 Simplified reaction scheme results

Simplified reaction kinetics used in case OF_{2reactions} include only two reaction equations. Reactions for methane and propane combustion were modeled as one-step reactions with following equations



Reaction rates were modeled with Arrhenius equation

$$k = AT^n e^{-E_a/RT} \quad (6.4)$$

where k is the rate constant, A is the constant pre-exponential factor, n accounts for temperature dependence of A and E_a is the activation energy. Reaction rate is calculated as

$$r = k[Z]^a[X]^b \quad (6.5)$$

where r is the reaction rate, Z and X are mole concentrations of reactive substances (fuel and oxidizer respectively), a and b are constant experimentally defined reaction orders.

Reaction order relates concentration of reactant to the reaction rate. Reaction coefficients used in this thesis are shown in Table 6.8.

Table 6.8. Coefficients for Arrhenius reactions used for 2 stoichiometric reactions. (Oksanen 1995, 114)

Fuel specie	A	E_a/R	a	b
CH ₄	1.30e8	24 000	-0.3	1.3
C ₃ H ₈	4.84e9	15 000	0.1	1.65

6.3.1 Convergence

Mass balance of global reaction kinetics OF_{2reactions,c} and OF_{2reactions} cases is compared with base case OF_{detailed,1} in Table 6.9. OF_{2reactions,c} mass balance error and standard deviation is smaller than in the base case and even smaller than errors with OF_{coarse} case which did not have radiation or heat transfer either. OF_{2reactions} has also smaller errors in mass balance and standard deviation but now outflow is larger than inflow. Simplified reaction schemes seems to be more accurate and stable in mass balance wise compared to complex GRI3.0 kinetics.

Table 6.9. Average mass balances of 2 global reaction case.

Case	Outlet average [kg/s]	Outlet SD [kg/s]	Input [kg/s]	Relative error [%]
OF _{detailed,1}	1.536	0.357	1.696	9.4
OF _{2reactions,c}	1.592	0.029	1.696	6.1
OF _{2reactions}	1.561	0.012	1.696	7.9

Mole fractions of species in the flue gas at outlet are shown in Figure 6.10 and detailed values in Table 6.10. Overall, both cases with simplified reaction scheme cases seem to match better with stoichiometric results than base case, since reaction equations are the same with simplified cases and stoichiometric calculations. In both 2 reaction cases fractions of CO₂ and H₂O are over predicted slightly but values are close to stoichiometric ones. Fraction of O₂ is smaller than stoichiometric and process data reference but is still in right order of magnitude and much higher than in the base case.

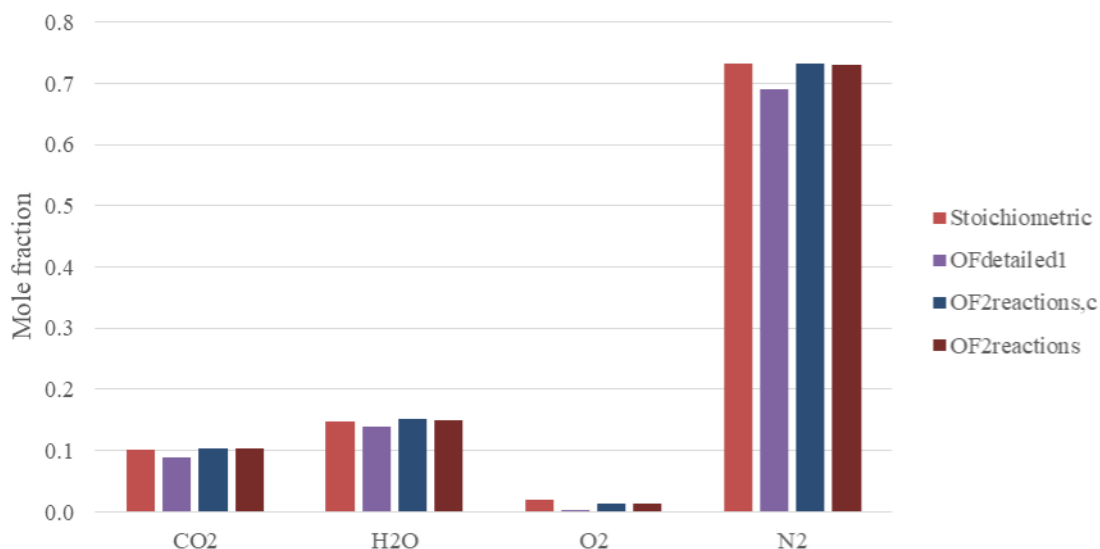


Figure 6.10. Average mole fractions of flue gas components of 2 global reaction cases at outlet.

Table 6.10. Average mole fractions of flue gas components of 2 global reaction cases at outlet.

Case	CO ₂	H ₂ O	O ₂	N ₂	Stoic. sum
Stoichiometric	0.100	0.147	0.020	0.732	0.999
OF _{detailed,1}	0.089	0.139	0.001	0.691	0.920
OF _{2reactions,c}	0.103	0.151	0.014	0.733	1.001
OF _{2reactions}	0.103	0.150	0.013	0.731	0.997

Ratio of elemental components of C and H to O and N is 0.058 for OF_{2reactions,c} and 0.059 for OF_{2reactions} which are close to value at inlet boundary (0.055) and indicate better conservation of elemental components than detailed reaction scheme cases.

Outlet temperature of OF_{2reactions,c} was 2145.6 °C (neglecting heat transfer to the tubes) which is lower than adiabatic flame temperature (2178.4 °C) but higher than temperature in the OFcoarse case (2123.4 °C). In OF_{2reactions} outlet temperature was 697.5 °C (3.21 MW of heat transfer to the tubes) which is considerably lower than in the base case (748.9 °C) or the reference value from process data (778.5 °C). Without radiation model, simplified reaction scheme seems to work well with comparison to ideal values but when heat transfer is involved temperature levels are not same as the experimental values.

6.3.2 Duration

OF_{2reactions,c} case was ran for approximately 310 000 iterations for 8 days and 22,5 hours with 20 computational cores. Simulation was started from cold flow profile from OF_{coarse} simulation to avoid problems with large variety of combustion products from GRI3.0 library with simplified reaction model. OF_{2reactions} was simulated for 35 000 iterations for 4 days and 13.5 hours with 58 computational cores. Result from OF_{2reactions,c} was used as initialization.

6.3.3 Results

Velocity profiles of simplified reaction scheme cases can be seen in Figure 6.11. Flow field in the OF_{2reactions} did not converge to similar shape flame than in the other OF cases and large vortex remained at the top of the furnace when the convergence criteria had stabilized. Velocity profile of the flame is very high in OF_{2reactions,c}, almost continuous stream from burner to chimney. Velocity profile of the jet in OF_{2reactions} has similar flame height than base case. Both of the simplified reaction scheme cases show higher velocity regions (vertical yellow lines near the outer edges of the jet) starting from secondary air inlets, indicating that reaction speed increases with secondary air flow at these regions.

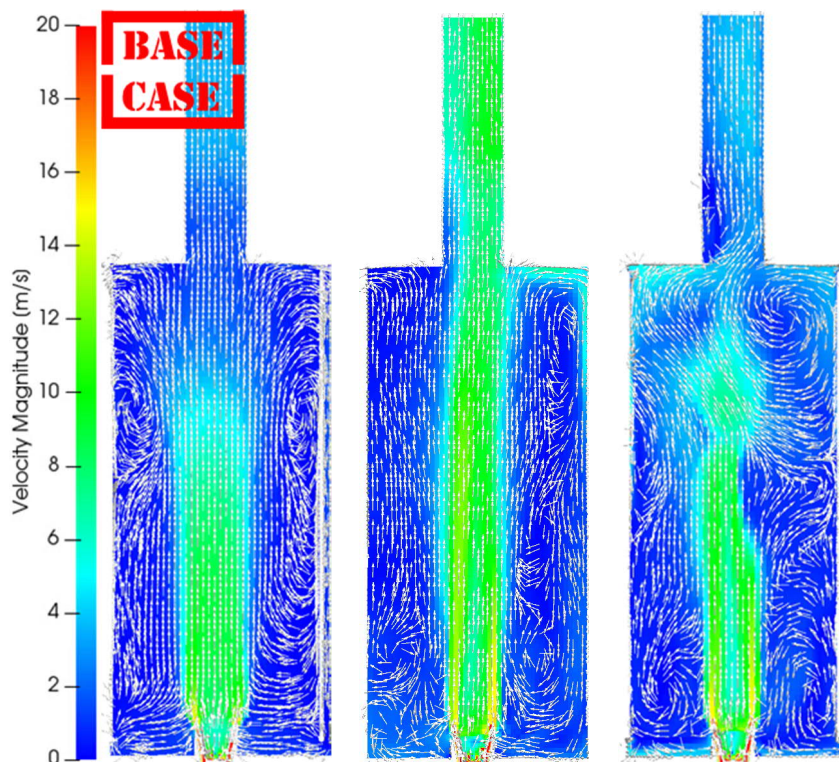


Figure 6.11. Average velocity profile at Z-normal plane for OF_{detailed,1} on the left, OF_{2reactions,c} in the middle and OF_{2reactions} on the right.

Temperature fields of simplified reaction schemes are shown in Figure 6.12. Temperature profile of $OF_{2\text{reactions}}$ is narrower than in the base case and shows higher temperatures near the burner and inside the flame. Height of the profiles are roughly the same. Temperature profile of the flame in $OF_{\text{detailed},1}$ has clear gap between the cold inlet gases and hot combustion region where the fuel-air mixture heats up before combustion. This region is very narrow in $OF_{2\text{reactions}}$, almost nonexistent and combustion occurs closer to the burner than in $OF_{\text{detailed},1}$. This shows that simpler 2 reaction mechanism has faster reactions than more complex GRI3.0 kinetics. Lack of different reaction paths in stoichiometric reactions results more rapid combustion without intermediate components. Higher temperature inside the flame in $OF_{2\text{reactions}}$ comes from the simpler reaction kinetics where all of the heat from the combustion is released all at once from single oxidation reaction. In $OF_{\text{detailed},1}$ energy release happens in multiple steps through various reactions and is therefore spread out for different reactions more evenly. Faster kinetics also minimizes the spreading of the flame when fuel air mixture reacts faster and the fuel does not have time to spread radially.

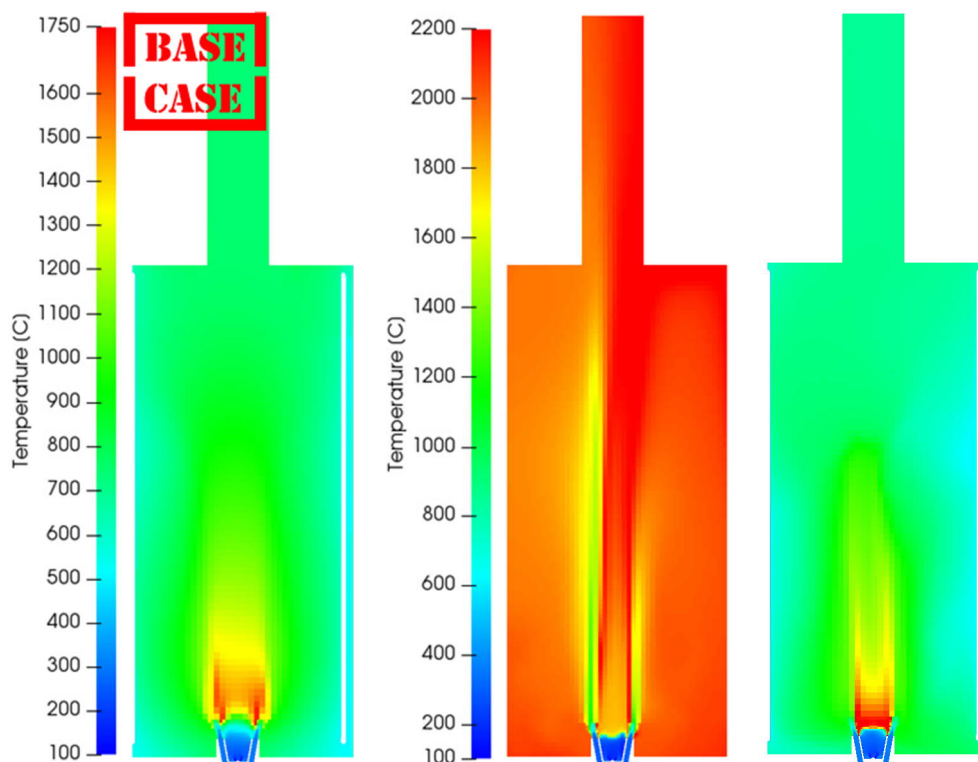


Figure 6.12. Average temperature profile at Z-normal plane for $OF_{\text{detailed},1}$ on the left, $OF_{2\text{reactions},c}$ in the middle and $OF_{2\text{reactions}}$ on the right. Note the different scale for $OF_{2\text{reactions},c}$.

It can be seen from the oxygen profiles in Figure 6.13 that simplified reaction schemes do not consume oxygen as fast near the burner and trails of the oxygen profiles are higher compared to base case.

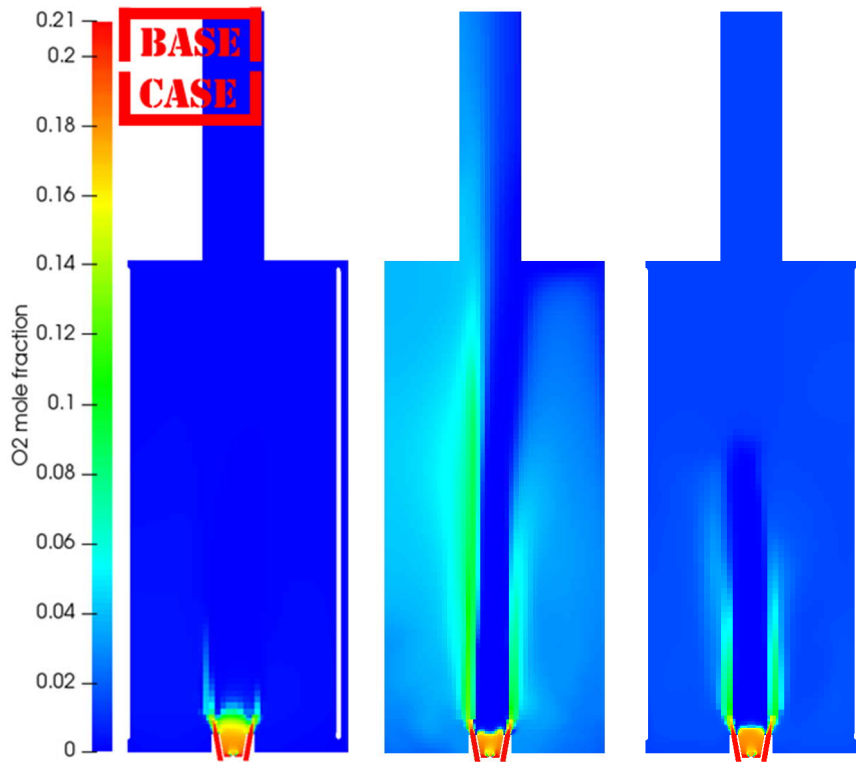


Figure 6.13. Average O_2 mole fraction field at Z-normal plane for $OF_{\text{detailed},1}$ on the left, $OF_{2\text{reactions},c}$ in the middle and $OF_{2\text{reactions}}$ on the right.

6.4 Comparison with Fluent results and measurements

Next the OpenFOAM results from $OF_{2\text{reactions}}$ are compared to Fluent simulation done previously in a separate study for this process furnace. $OF_{2\text{reactions}}$ is chosen because the conservation of the mass and elemental balance is better than the base case and boundary conditions used in case $OF_{2\text{reactions}}$ are the same as in the Fluent simulations, see Table 6.1. Fluent used realizable $k - \epsilon$ turbulence model, EDM for combustion modelling and DOM for radiation modelling. Result contours from Fluent simulations are taken as snapshot from transient simulation data. Small changes in the flame shape and size are presented in the transient simulation but overall characteristics and measured convergence criteria (heat transfer to tubes, flue gas temperature and oxygen concentration at outlet) are stable.

Some experimental data was obtained from the DCS (Distributed Control System) of the process furnace unit. Temperature and O₂ mole percentage of the flue gas are continuously measured at the flue gas duct and tube outer surface temperatures at four locations with 3 m and 9 m heights from the furnace floor.

Mass balance of OF_{2reactions} and Fluent cases are shown in Table 6.11. Fluent mass balance has converged well and error is minimal compared to results from OpenFOAM simulations.

Table 6.11. Average mass balance of OF_{2reactions} and Fluent case.

Case	Outlet average [kg/s]	Outlet SD [kg/s]	Input [kg/s]	Relative error [%]
Fluent	1.697	0.005	1.696	0.04
OF _{2reactions}	1.561	0.012	1.696	7.9

Mole fractions of the flue gas at outlet are shown in Figure 6.14 and detailed values in Table 6.12. Outlet compositions are close to each other but OF_{2reactions} tends to slightly over predict the production of CO₂ and H₂O while Fluent results are similar compared to stoichiometric values. Mole fractions of combustion products higher than stoichiometric is unrealistic in OF_{2reactions} but results are still rather closet to stoichiometric. Oxygen fraction changes in response of generation of products and Fluent with smaller fractions of end products has higher O₂ fraction than OF_{2reactions}.

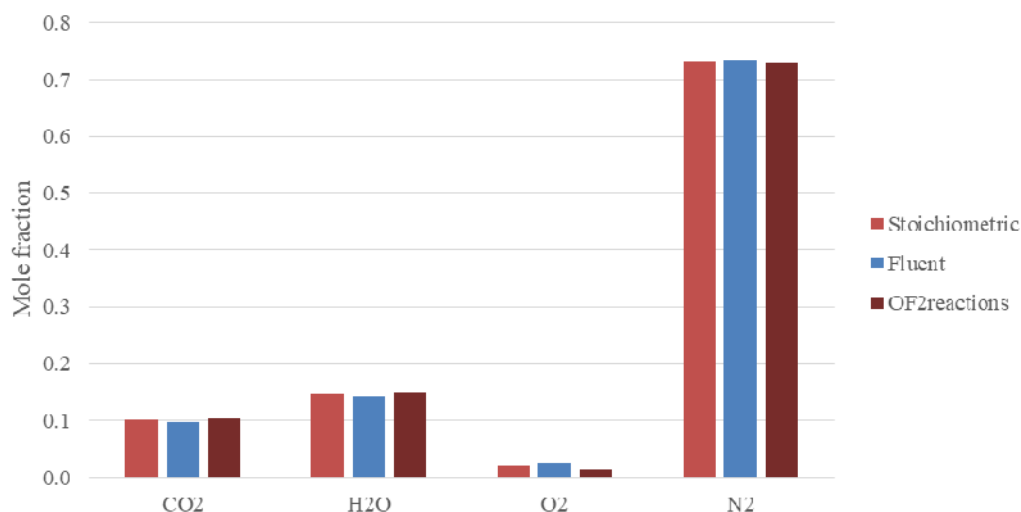


Figure 6.14. Average mole fractions of flue gas component of OF_{2reactions} and Fluent case at outlet.

Table 6.12. Average mole fractions of flue gas components of OF_{2reactions} and Fluent case at outlet.

Case	CO ₂	H ₂ O	O ₂	N ₂	Stoic. sum
Stoichiometric	0.100	0.147	0.020	0.732	0.999
Fluent	0.097	0.143	0.026	0.734	1.000
OF _{2reactions}	0.103	0.150	0.013	0.731	0.997

Elemental balance with ratio of fuel and oxidizer components in Fluent is 0.054 which is very close to value at inlets (0.055) and indicates well conserved elemental balance. OF_{2reactions} had the best accuracy (0.059) of the cases with heat transfer and radiation which is in right order of magnitude but not as close as in the Fluent case.

Outlet temperature is the largest difference between Fluent and OF_{2reactions} results. Outlet temperature in Fluent case was 797.9 °C which higher than estimated from process data (778.5 °C). OF_{2reactions} has outlet temperature of 697.5°C which is significantly lower than in the previous OpenFOAM cases or process data value.

6.4.1 Velocity field

Velocity field is shown for OF_{2reactions} and Fluent simulations for Z-plane in Figure 6.15. In OF_{2reactions} case, height of the jet is smaller than in Fluent case. Reaction rates are calculated with similar two reaction equation schemes both in OpenFOAM and in Fluent but they seem to produce slightly different results.

At the burner inlet Fluent case shows higher velocities at outer border of the flame, in the same direction as the secondary air inlet pipes. Injection of secondary air corresponds higher jet velocities in Fluent case than in OF_{2reactions}. Reactions in Fluent case respond faster to additional air supplied to the mixture, react faster and achieve higher velocities.

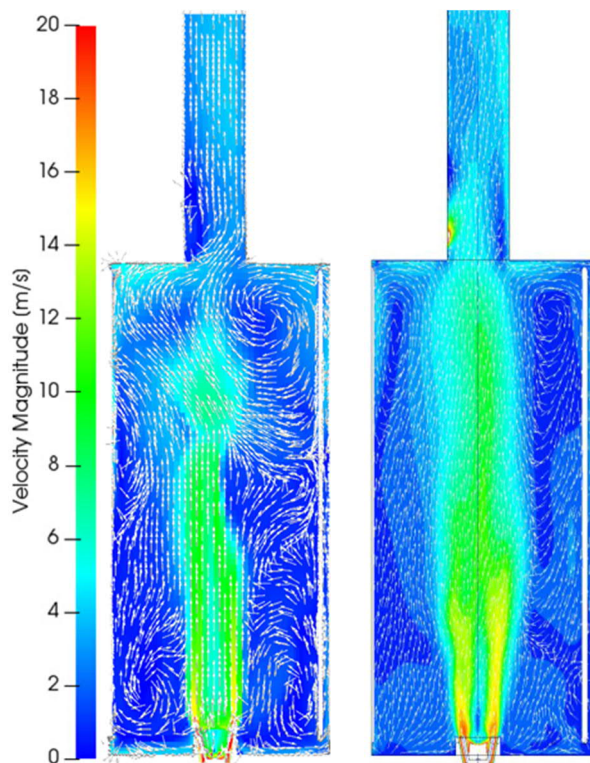


Figure 6.15. Average velocity profile at Z-normal plane for OF_{2reactions} on the left and transient profile for Fluent on the right.

6.4.2 Temperature field and heat transfer

Temperature field is shown for OF_{2reactions} and Fluent simulations for Z-plane in Figure 6.16. Temperature profile of the flame is significantly shorter in OF_{2reactions} case than in Fluent. This is caused by the differences in radiation models when P1 model in OF_{2reactions} case calculates radiation to be more intense at the hottest region near the burner and DOM spreads out the radiation more evenly throughout the flame in the Fluent case. Heat is then radiated faster out of the flame in the OF_{2reactions} case than in Fluent case which causes the temperature field to diminish faster in OF_{2reactions} case. More intense radiation early on at the jet flame also rises the temperature of the whole furnace to higher level in OF_{2reactions} case than in Fluent case.

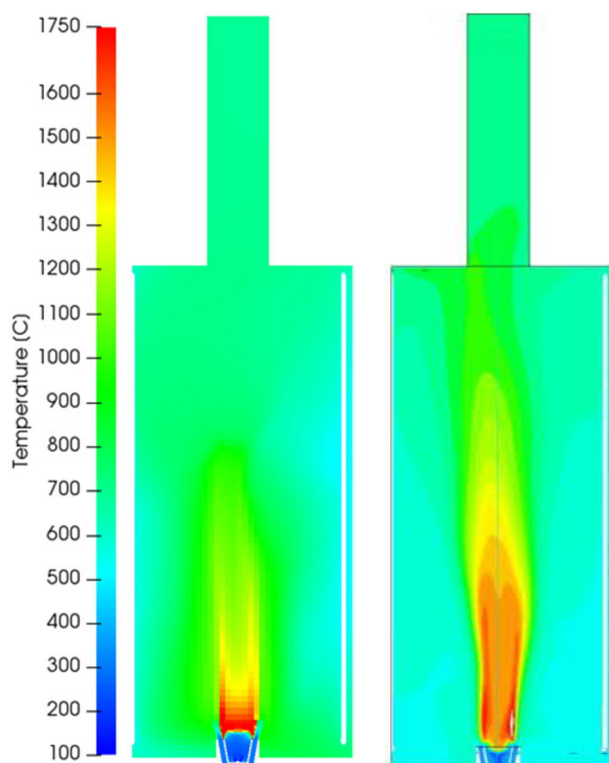


Figure 6.16. Average temperature profile at Z-normal plane for $OF_{2\text{reactions}}$ on the left and transient profile for Fluent on the right.

Temperature profile of the tube outer surface temperature for $OF_{2\text{reactions}}$ and Fluent cases are shown in Figure 6.17 and Figure 6.18. Tube surface temperatures are generally higher with $OF_{2\text{reactions}}$ case than in Fluent. Temperature fields are also more uniform in Fluent case while $OF_{2\text{reactions}}$ case shows hotter and colder regions on tube surfaces. DOM radiation model in Fluent case results in more evenly distributed and lower temperature field than P1 in $OF_{2\text{reactions}}$ case. In $OF_{2\text{reactions}}$ case, hotter regions can be observed most clearly in Figure 6.17 with West and North side tube bundles. Contact with circulating high temperature flue gases raises the surface temperatures of the tubes. Higher overall temperature inside the furnace in $OF_{2\text{reactions}}$ case increases also the temperature of the tubes.

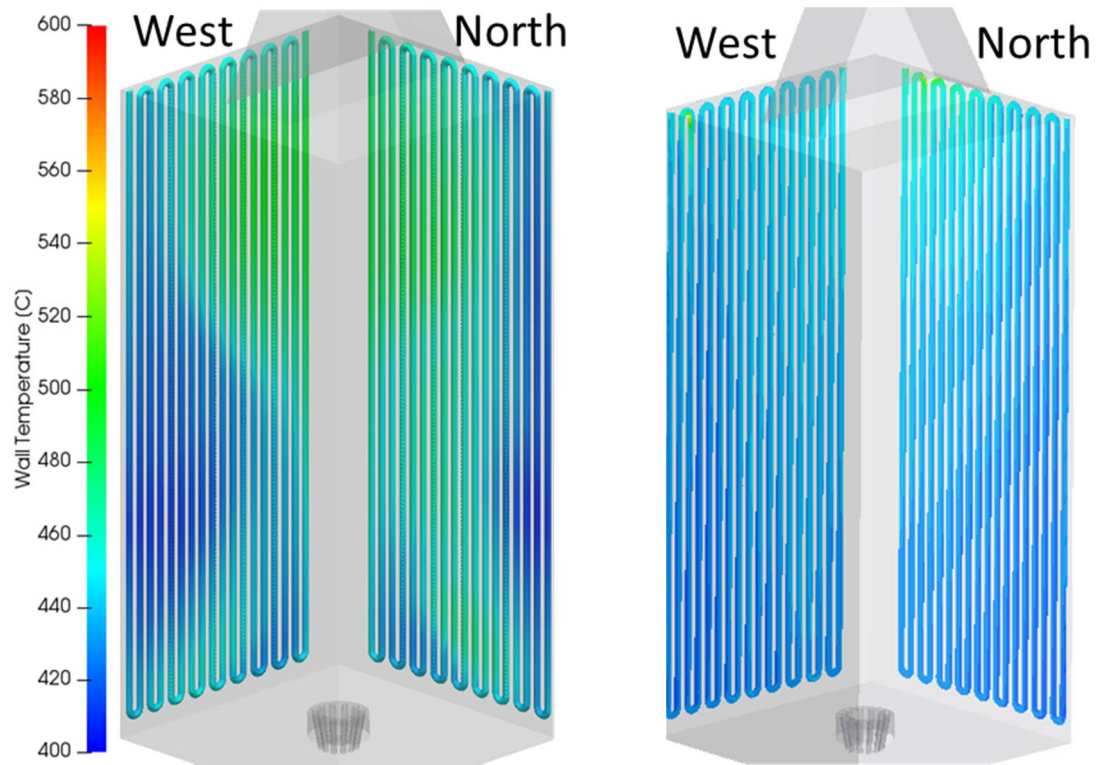


Figure 6.17. Average temperature profile at North and West tube bundles for $OF_{2\text{reactions}}$ on the left and transient profile for Fluent on the right.

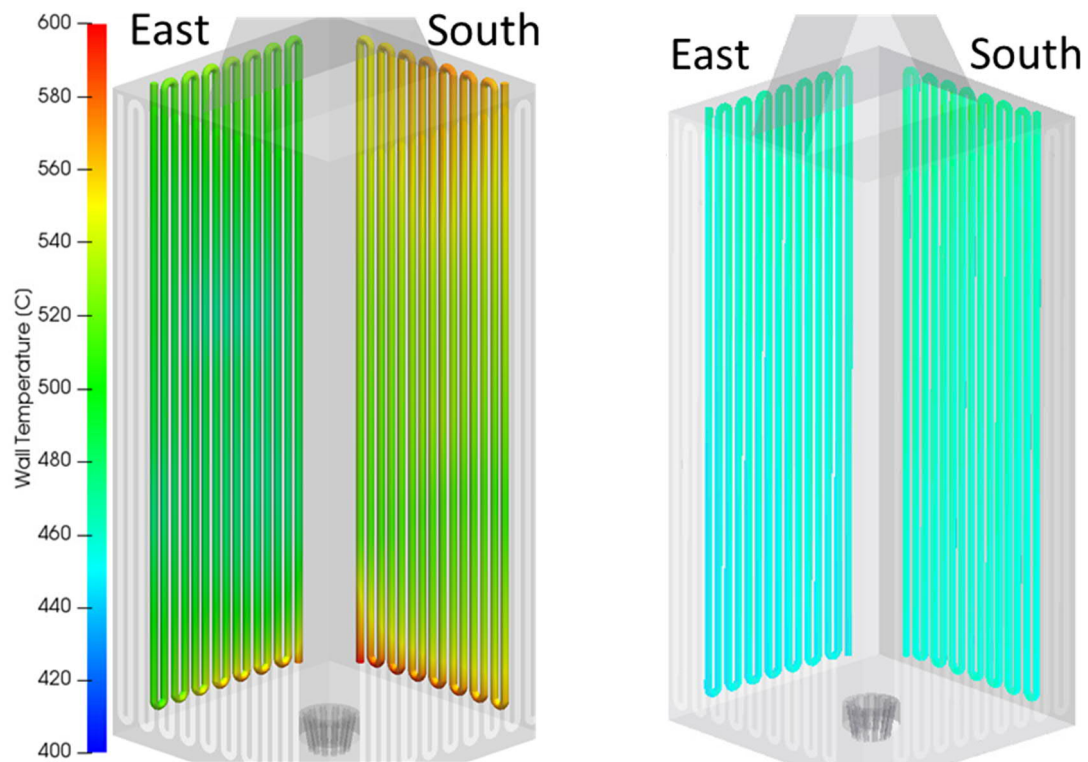


Figure 6.18. Average temperature profile at South and East tube bundles for $OF_{2\text{reactions}}$ on the left and transient profile for Fluent on the right.

The results of the tube surface temperatures are quantified and compared with measurement data, by area averaging tube surface temperatures and extracting them on various heights in the furnace, as shown in Figure 6.19. In Figure 6.19, average temperature at certain elevation for specific tube bundle is shown and compared with the maximum design temperature of tube material (560 °C). Tube surface temperature measurements are marked as squares and their color is the same as their tube section. From four measurement points, three are at South tube bundle and one at North bundle. Measurements are at height of 3 or 9 meters.

In Figure 6.19, it is clear that $OF_{2\text{reactions}}$ case has higher tube surface temperatures than in Fluent, especially at higher fluid temperatures in East and South regions. Effect of more intense radiation from the flame at low elevations with P1 model can be seen as a curve in the temperature profile in $OF_{2\text{reactions}}$ case. At higher elevation North and West tubes have similar temperature levels in both $OF_{2\text{reactions}}$ and Fluent cases and quite close to measured value at North side. Higher temperature inside the furnace affects especially the East and South side tubes which have higher fluid temperatures.

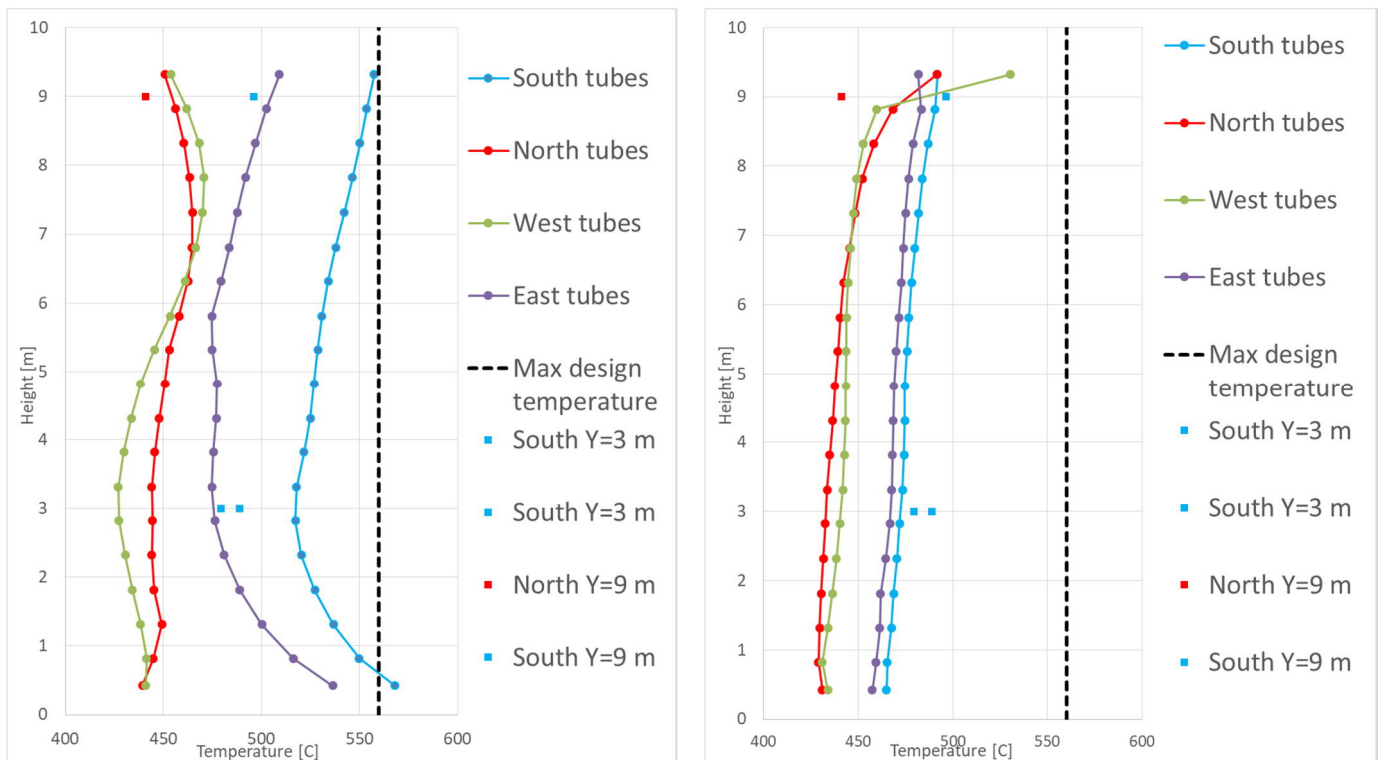


Figure 6.19. Average tube temperatures for $OF_{2\text{reactions}}$ case on the left and transient data Fluent case on the right.

Heat duty for tube sections is shown in Table 6.13 for OF_{2reactions} and Fluent cases. Differences in tube surface areas are caused by meshing the curved surface and the mesh conversion from Ansys Meshing to OpenFOAM. Heat flux values follow the same pattern in both cases. North and West sides have higher fluxes since their whole surface area is visible to the radiation from the flame and their fluid temperature is lower, so they have higher potential to transfer the heat. South and East sides have the back side facing the furnace walls instead of the flame, which decreases the heat flux. In Fluent case, heat transfer is divided rather equally between all of the tube regions. In OF_{2reactions} case, there is more variation in heat transferred by the tubes and especially South side tubes have significantly lower heat transfer than other regions. South tube bundle has the highest hydrocarbon temperature to transfer the heat which limits the possible heat transfer.

Table 6.13. Average heat transfer to the tubes for OF_{2reactions} and transient data for Fluent.

Tube section	Area [m ²]		Heat flux [W/m ²]		Heat transfer [MW]	
	OF _{2reactions}	Fluent	OF _{2reactions}	Fluent	OF _{2reactions}	Fluent
South	49.5	50.0	13 127	15 293	0.65	0.76
North	29.7	30.0	31 558	25 320	0.94	0.76
East	49.5	50.0	15 236	15 996	0.75	0.80
West	29.7	30.0	29 381	25 034	0.87	0.75
Total	158.4	160			3.21	3.07

6.4.3 Oxygen field

Oxygen field is shown for OF_{2reactions} and Fluent simulations in Figure 6.20. Figures show that in OF_{2reactions} case more of the oxygen is consumed by the combustion while in Fluent case some excess oxygen remains, see Table 6.1. In Fluent case oxygen spreads from secondary air streams around the furnace but in OF_{2reactions} secondary air streams stay attached to the flame. Higher temperature around the flame in OF_{2reactions} compared to Fluent increases the reaction rates and accelerates the consumption of oxygen in the combustion.

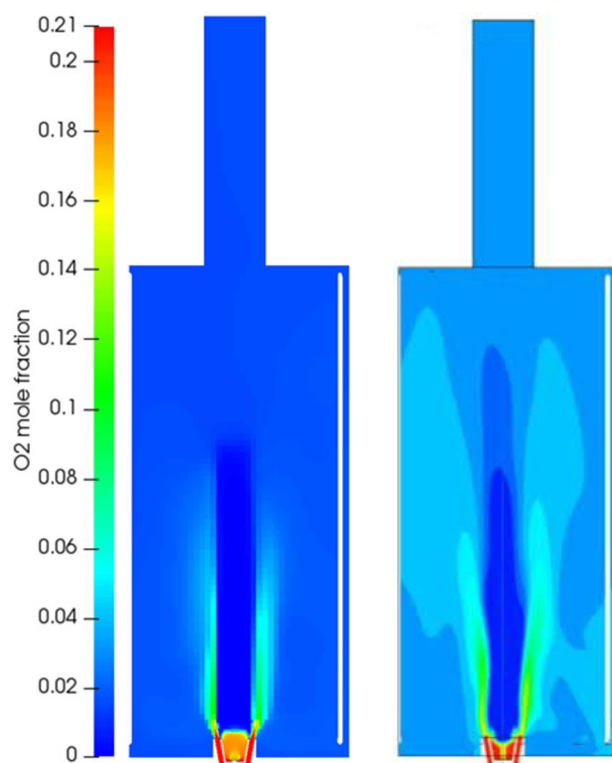


Figure 6.20. Average O₂ mole fraction field at Z-normal plane for OF₂ reactions on the left and transient field for Fluent on the right.

7 CONCLUSIONS

The purpose of this work was to simulate non-premixed turbulent combustion in industrial scale process furnace with open source software OpenFOAM. The aim was to test the capabilities of OpenFOAM in combustion simulation in terms of simulation time and accuracy. Results were compared to simulation results from Fluent and a few measurement points.

Objective of the thesis was reached and simulation of the process furnace was completed with OpenFOAM. Evaluation of the performance was done by running multiple different cases with different boundary conditions and reaction kinetics. Accuracy requirements were only partially fulfilled when heat duty and outlet flue gas temperature were not met with used modelling methods. Mass balance was not fully conserved in the simulations which showed also as conservation issues with elemental balance.

7.1 Mass balance

Simulation results showed that reactingFoam solver couldn't maintain accurate mass balance during simulation and average error between inflow and outflow is between 5-10 %. Error was significant and it should be considered when evaluating the results. Mass balance error in Fluent was less than 1 % which tells that Fluent had better conservation of mass.

7.2 Flue gas composition and elemental balance

Flue gas composition at the outlet was similar between Fluent case and stoichiometric calculation, since they use same one-step global reaction equations. In OF_{coarse} and OF_{detailed,1} case with GRI3.0 reaction schemes produced less CO₂ but more CO in combustion. Combustion was not completed fully in OpenFOAM detailed simulations even when more oxygen was consumed in the combustion compared to Fluent results. More complex reaction scheme therefore requires more oxygen than simpler reactions. Oxygen is consumed in production of intermediate components during combustion such as CO and OH. Simplified reaction schemes in OF_{2reaction,c} and OF_{2reactions} produced results closest to stoichiometric and Fluent values while fractions of CO₂ and H₂O were over predicted. More oxygen were consumed in OF_{2reaction,c} and OF_{2reactions} compared to

stoichiometric and Fluent values but all in all simplified reaction schemes produced results closer to reference values.

Elemental balances were not conserved in $OF_{\text{detailed},1}$, $OF_{\text{detailed},2}$ and $OF_{\text{detailed},3}$ while Fluent and simpler reaction scheme simulations had elemental ratio of fuel and oxidizer components close to the inlet value. This indicates that simpler reaction kinetics were more capable to conserve elemental balance in the simulations.

7.3 Flame size and shape

Fluent simulation had longer flame height than other simulations with same boundary conditions. Applying the radiation and heat transfer to the simulation shortens the jet height for OpenFOAM cases. Velocity profile of $OF_{\text{detailed},1}$ case was significantly shorter than Fluent which indicated that GRI3.0 kinetics in OpenFOAM are slower than kinetics with two global reaction equations in Fluent simulations. Higher reaction speeds accelerate the flow faster and produce higher velocity jet. Flame height increased in cases where air mass flow was increased and secondary air flow seemed to have larger impact on flame height than primary air. Temperature profile in 2 reaction cases is narrower and higher than in the GRI3.0 cases.

7.4 Heat duty and flue gas outlet temperature

All of the OpenFOAM cases had higher heat duty to the tubes than Fluent or the process data suggests which the cause of the radiation model P1. P1 over estimates the radiation from the flame and causes the heat transfer to the tubes to increase. Therefore, flue gas temperatures go the opposite when radiation cools down the flue gases more in OpenFOAM cases resulting lower outlet temperatures than in Fluent with same boundary conditions in $OF_{\text{detailed},1}$ and $OF_{2\text{reactions}}$.

7.5 Simulation duration

Comparison of simulation duration is shown in Table 7.1. Values in the table are calculated by dividing the number of iterations done per case with total time used in seconds and the number of used cores. Practical comparison is made in next column which tells the number of iterations that are completed in 24 hours with 30 computational

cores for all of the cases. That calculation speed can be compared with total number of iterations used per case in this thesis.

Table 7.1. Comparison of simulation time in OpenFOAM cases.

Case	iter/s/core	iter/24 h/30 cores	Total iterations
OF _{coarse}	0.0148	38 257	430 000
OF _{detailed,1}	0.0013	3393	250 000
OF _{detailed,2}	0.0013	3479	45 000
OF _{detailed,3}	0.0008	2087	29 000
OF _{2reaction,c}	0.0202	52 410	310 000
OF _{2reaction}	0.0017	4328	35 000

It can be seen from Table 7.1, that cases with coarse mesh are order of magnitude faster to compute when they have much smaller mesh size. Results have some inaccuracy due to the fact that not all of the cases were ran on the similar computational cores due to parallel computing of the cases which was distributed to several different computers. It can be said that OF_{2reaction,c} and OF_{2reaction} cases are faster to simulate due to their simplified reaction kinetics.

7.6 Recommendations

OpenFOAM was able to simulate similar scale combustion systems as Fluent but had still some issues in terms of accuracy and simulation time. Methods that were investigated in this thesis that can be used in large scale combustion simulations but more research has to be done to achieve same level of accuracy and usability than Fluent in the future.

Recommendations for the future work is to apply heat transfer earlier on in the coarse mesh simulations to achieve realistic temperature field at a phase where calculations are faster and save computational time with fine mesh simulations. P1 radiation model overestimated the radiation and applying other radiation models such as DOM should be investigated to see if results match better with measurements. Error in the mass balance is another major concern and should be tested with different combustion solvers and meshes to find out the cause of the error.

REFERENCES

- Barlow Robert and Frank Jonathan. 2007. Piloted CH₄/Air Flames C, D, E and F – Release 2.1. Sandia National Laboratories. pp. 12. Available: <https://www.sandia.gov/TNF/DataArch/FlameD.html>
- Bender Edward A. 1978. An Introduction to Mathematical Modeling. United States of America. John Wiley & Sons Inc. pp. 256. ISBN 0-471-02951-3.
- Bhatti Muhammad R. et al. 2017. Numerical Study of Hydrogen Peroxide Thermal Decomposition in a Shock Tube. Journal of Thermal Science, vol. 26, pp. 235-244. Available: <https://doi.org/10.1007/s11630-017-0935-6>.
- Biswas G., Eswaran V. 2002. Turbulent Flows: Fundamentals, Experiments and Modeling. India. Alpha Science International Ltd. pp. 456. ISBN 1-84265-067-X.
- Borman Gary, Ragland Kenneth. 1998. Combustion Engineering. United States of America. McGraw-Hill Companies Inc. pp. 613. ISBN 0-07-006567-5.
- CDF Direct. 2018. OpenFOAM User Guide. [www-page] [cited 8.11.2018] Available: <https://cfd.direct/openfoam/user-guide/>
- Chen Zhibin, et al. 2014. Extension of the eddy dissipation concept and smoke point soot model to the LES frame for fire simulations. Fire Safety Journal, vol. 64, pp. 12-26. Available: <https://doi.org/10.1016/j.firesaf.2014.01.001>.
- Endres A., Sattelmayer T. 2018. Large Eddy simulation of confined turbulent boundary layer flashback of premixed hydrogen-air flames. International Journal of Heat and Fluid Flow, vol. 72, pp. 151-160. Available: <https://doi.org/10.1016/j.ijheatfluidflow.2018.06.002>.
- Ferziger Joel, Peric Milovan. 1997. Computational Methods for Fluid Dynamics. Germany. Springer. pp. 364. ISBN 3-540-59434-5.
- Fukumoto Kazui, Wang Changjian, Wen Jennifer. 2018. Large eddy simulation of upward flame spread on PMMA walls with a fully coupled fluid-solid approach. Combustion and Flame, vol. 160, pp. 365-387. Available: <https://doi.org/10.1016/j.combustflame.2017.11.012>.
- Garten B. et al. 2015. Detailed radiation modeling of a partial-oxidation flame. International Journal of Thermal Sciences, vol. 87, pp. 68-84. Available: <https://doi.org/10.1016/j.ijthermalsci.2014.07.022>
- Halouane Y., Dehbi A. 2017. CFD simulations of premixed hydrogen combustion using the Eddy Dissipation and the Turbulent Flame Closure models. International Journal of

Hydrogen Energy, vol. 42, pp. 21990-22004. Available: <https://doi.org/10.1016/j.ijhydene.2017.07.075>.

Han Xingsi, Li Jingxuan, Morgans Aimee S. 2015. Prediction of combustion instability limit cycle oscillations by combining flame describing function simulations with a thermo acoustic network model. Combustion and Flame, vol. 162, pp. 3632-3647. Available: <https://doi.org/10.1016/j.combustflame.2015.06.020>.

Han Xingsi, Yang Junfeng, Mao Junkui. 2016. LES investigation of two frequency effects on acoustically forced premixed flame. Fuel, vol. 185, pp. 449-459. Available: <https://doi.org/10.1016/j.fuel.2016.08.005>.

Holtmann Tobias. 2016. Mathematics, Numerics, Derivations and OpenFOAM. Holtmann CFD. Fourth edition. Available: https://www.researchgate.net/publication/307546712_Mathematics_Numerics_Derivations_and_OpenFOAMR

Hsu Chang S., Robinson Paul R. 2017. Handbook of Petroleum Technology. Switzerland. Springer International Publishing. pp. 1238. ISBN 978-3-319-49347-3.

Incropera Frank et al. 2007. Fundamentals of Heat and Mass Transfer. Sixth Edition. United States of America. John Wiley & Sons Inc. pp. 997. ISBN 978-0-471-45728-2.

Kadar Ali Hussain. 2015. Modelling Turbulent Non-Premixed Combustion in Industrial Furnaces. Master's Thesis. Delft University of Technology. Faculty of Electrical Engineering, Mathematics and Computer Science. Department of Applied mathematics. pp. 142. Available: <http://resolver.tudelft.nl/uuid:8f3235ea-6efa-466e-9e48-9eda89bb04e7>.

Kjälldman Lars. 1995. Polton aerodynamiikka. Poltto ja palaminen: Raiko et al. Jyväskylä. International Flame Research Foundation – Suomen kansallinen osasto. pp. 323-343. ISBN 951-666-448-2.

Li Jingxuan, et al. 2017. Numerical prediction of combustion instability limit cycle oscillations for a combustor with a long flame. Combustion and Flame, vol. 185, pp. 28-43. Available: <https://doi.org/10.1016/j.combustflame.2017.06.018>.

Li Zhiyi et al. 2018. Finite-rate chemistry modelling of non-conventional combustion regimes using a Partially-Stirred Reactor closure: Combustion model formulation and implementation details. Applied Energy, vol. 225, pp. 637-655. Available: <https://doi.org/10.1016/j.apenergy.2018.04.085>

Lysenko Dmitry, Ertesvåg Ivar, Rian Kjell. 2014. Numerical Simulations of the Sandia Flame D Using the Eddy Dissipation Concept. Flow Turbulence Combust, vol. 93, pp. 665-687. Available: <https://doi.org/10.1007/s10494-014-9561-5>

Marzouk Osama A., Huckaby David E. 2010. Simulation of a Swirling Gas-Particle Flow Using Different k-epsilon Models and Particle-Parcel Relationships. Engineering Letters 18. Available:

https://www.researchgate.net/publication/41668039_Simulation_of_a_Swirling_Gas-Particle_Flow_Using_Different_k-epsilon_Models_and_Particle-Parcel_Relationships

Modest Michael F. 2013. Radiative Heat Transfer. Third edition. United States of America. Elsevier Inc. ISBN 978-0-12-386944-9.

Moilanen Antero, Nieminen Matti ja Alén Raimo. 1995. Polttoaineiden ominaisuudet ja luokittelu. Poltto ja palaminen: Raiko et al. Jyväskylä. International Flame Research Foundation – Suomen kansallinen osasto. pp. 87-108. ISBN 951-666-448-2.

Mullinger Peter, Jenkins Barrie. 2014. Industrial and Process Furnaces: Principles, Design and Operation. Second Edition. United States of America. Elsevier Ltd. 639. ISBN 978-0-08-099377-5.

Oksanen Antti. 1995. Kaasun ja öljyn palaminen. Poltto ja palaminen: Raiko et al. Jyväskylä. International Flame Research Foundation – Suomen kansallinen osasto. pp. 109-138. ISBN 951-666-448-2.

OpenCFD. 2018. Standard boundary conditions. OpenCFD Ltd. [online page] [Referred 27.11.2018] Available: <https://www.openfoam.com/documentation/user-guide/standard-boundaryconditions.php>

Pang Kar Mun et al. 2013. Development and validation of a local time stepping-based PaSR solver for combustion and radiation modeling. Proceedings of 8th International OpenFOAM Workshop. Available: http://orbit.dtu.dk/files/92578251/Development_and_validation_of_a_local_time.pdf

Rajika J. K., Narayana Mahinsasa. 2016. Modelling and simulation of wood chip combustion in a hot air generator system. SpringerPlus, vol. 5, article 1166. Available: <https://doi.org/10.1186/s40064-016-2817-x>.

Ren Ning, et al. 2016. Large eddy simulation of turbulent vertical wall fires supplied with gaseous fuel through porous burners. Combustion and Flame, vol. 169, pp. 194-208. Available: <https://doi.org/10.1016/j.combustflame.2015.12.008>.

Ren Ning, et al. 2017. Large-scale fire suppression modeling of corrugated cardboard boxes on wood pallets in rack-storage configurations. Fire Safety Journal, vol. 91, pp. 695-704. Available: <https://doi.org/10.1016/j.firesaf.2017.04.008>.

Ren Ning, Wang Yi, Trouve Arnauld. 2013. Large Eddy Simulation of Vertical Turbulent Wall Fires. Procedia Engineering, vol. 62, pp. 443-452. Available: <https://doi.org/10.1016/j.proeng.2013.08.086>.

Sedano Camilo, et al. 2017. Prediction of a small scale pool fire with FireFoam. International Journal of Chemical Engineering, vol. 2017, pp. 1-12. Available: <https://doi.org/10.1155/2017/4934956>.

Shekarian Ali A., Tabejamaat Sadegh, Shoraka Yashar. 2014. Effects of incident shock wave on mixing and flame holding of hydrogen in supersonic air flow. International Journal of Hydrogen Energy, vol. 39, pp. 10284-10292. Available: <https://doi.org/10.1016/j.ijhydene.2014.04.154>.

Shih Tsan-Hsing et al. 1995. A new $k-\epsilon$ eddy viscosity model for high Reynolds number turbulent flows. Computer Fluids, vol. 24, pp.227-238. Available: [https://doi.org/10.1016/0045-7930\(94\)00032-T](https://doi.org/10.1016/0045-7930(94)00032-T)

Smith Gregory P. et al. 2002. GRI-Mech. [www-page] [cited 10.2.2019] Available: <http://combustion.berkeley.edu/gri-mech/>

Trambouze Pierre. 2000. Petroleum Refining V.4: Materials and Equipment. Paris. Editions Technips. pp. 740. ISBN 2-710807831.

Treese Steven A., Pujado Peter R., Jones David S. 2015. Handbook of Petroleum Processing. Second Edition. Switzerland. Springer International Publishing. pp. 1913. ISBN 78-3-319-14529-7.

Vilfayeau S. et al. 2017. Large eddy simulation of suppression of turbulent line fires by base-injected water mist. Proceedings of the Combustion Institute, vol. 36, pp. 3287-3295. Available: <https://doi.org/10.1016/j.proci.2016.06.058>.

Vilfayeau S., et al. 2016. Large eddy simulation of flame extinction in a turbulent line fire exposed to air-nitrogen co-flow. Fire Safety Journal, vol. 86, pp. 16-31. Available: <https://doi.org/10.1016/j.firesaf.2016.09.003>.

Wang C.J., et al. 2014. Predicting radiative characteristics of hydrogen and hydrogen/methane jet fires using FireFOAM. International Journal of Hydrogen Energy, vol. 39, pp. 20560-20569. Available: <https://doi.org/10.1016/j.ijhydene.2014.04.062>.

Wang Y, et al. Numerical Simulation of Sprinkler Suppression of Rack Storage Fires. Fire Safety Science, vol. 11, pp. 1170-1183. Available: <http://dx.doi.org/10.3801/IAFSS.FSS.11-1170>.

Wang Yi, Chatterjee Prateep, de Ris John L. 2011. Large eddy simulation of fire plumes. Proceeding of the Combustion Institute, vol. 33, pp. 2473-2480. Available: <https://doi.org/10.1016/j.proci.2010.07.031>.

White James P., et al. 2017. Water mist suppression of a turbulent line fire. Fire Safety Journal, vol. 91, pp. 705-713. Available: <https://doi.org/10.1016/j.firesaf.2017.03.014>.

Wu Y. 2010. The Critical Velocity and the Fire Development. Fourth International Symposium on Tunnel Safety and Security. Frankfurt Germany. pp. 407-417. Available: http://www.hemmingfire.com/news/get_file.php3/id/158/file/408-418_Critical+Velocity.pdf

Xia Yu, et al. 2017. Dispersion of Entropy Perturbations Transporting through an Industrial Gas Turbine Combustor. Flow Turbulence Combust, vol. 100, pp. 481-502. Available: <https://doi.org/10.1007/s10494-017-9854-6>.

APPENDIX I: COMBUSTION STUDIES WITH OPENFOAM IN THE LITERATURE

Table I. List of combustion studies with OpenFOAM found from the literature.

Authors	Year	Case Description	Combustion Solver	Pressure-velocity coupling	Turbulence Model	Radiation Model
Xia, Duran, Morgans, Han	2017	Gas turbine combustor	reactingFoam	PIMPLE	LES	
Li, Xia, Morgans Han	2017	Combustor with long flame	reactingFoam	PIMPLE	LES, SGS	
Han, Li, Morgans	2015	Combustor injector	reactingFoam	PIMPLE	LES, SGS	
Han, Yang, Mao	2016	Combustor	reactingFoam	PIMPLE	LES, SGS	
Bhatti, Sheikh, Manzoor, Khan, Al	2017	H ₂ O ₂ Decomposition in shock tube	reactingFoam	PIMPLE	k-e	
Rajika, Narayana	2016	Wood chip combustion, hot air generation	reactingFoam	SIMPLE	k-e	fvDOM Finite Volume Discrete Ordinates Method
Endres, Sattelmayer	2018	Turbulent boundary layer flashback, hydrogen-air flame	reactingFoam	PIMPLE	LES, Smagorinsky	
Shekarian, Tabejamaat, Shoraka	2014	Hydrogen flame with shock wave in supersonic flow	reactingFoam and rhoReactingFoam	PISO	SST k-w	

Sedano, Lopez, Ladino, Munoz	2017	Small-scale pool fire	fireFoam	PIMPLE	LES	fvDOM,
White, Verma, Keller, Hao, Trouve, Marshall	2017	Water mist suppression of fire	fireFoam		LES, SGS	
Ren, Vries, Zhou, Chaos, Meredith, Wang	2017	Fire suppression in large storage room with sprinklers	fireFoam		LES, SGS kinetic energy	fvDOM, equation
Fukumoto, Wang, Wen	2017	Upward flame spread on walls	fireFoam	PIMPLE	LES, SGS, WALE	fvDOM for non-scattering media, WSGGM
Ren, Wang, Vilfayeau, Trouve	2015	Vertical wall fires porous burners	fireFoam	PIMPLE	LES, SGS, WALE	fvDOM, simplified equation
Vilfayeau, White, Sunderland, Marshall, Trouve	2016	Flame extinction with air-nitrogen co-flow	fireFoam	PIMPLE	LES, SGS one equ. kinetic energy	fvDOM
Vilfayeau, Myers, Marshall, Trouve	2016	Fire suppression by base-injected water mist	fireFoam	PIMPLE	LES, SGS, one equ. kinetic energy	simplified model, global loss factor

Wang, Meredith, Zhou, Chatterjee, Xin, Chaos, Ren, Dorofeev	2014	Sprinkler suppression of rack storage fires	fireFoam		LES, SGS	fvDOM
Wang, Chatterjee, de Ris	2010	Fire plumes	fireFoam	PIMPLE	LES, SGS	simplified global loss factor
Ren, Wang, Trouve	2013	Vertical wall fires	fireFoam		LES, SGS, WALE	fvDOM
Wang, Wen, Chen, Dembele	2014	Hydrogen/methane jet fires	fireFoam	PIMPLE	LES, SGS	fvDOM, WSGGM
Chen, Wen, Xu, Dembele	2014	Smoke point soot model for fire simulations	fireFoam		LES, SGS	finite volume, absorption and emission coefficients

APPENDIX II: CALCULATIONS OF STOICHIOMETRIC REACTIONS

Fuel mass flow: 0.08914 kg/s

Air mass flow: 1.607 kg/s

Reaction equations: $\text{CH}_4 + 2\text{O}_2 = \text{CO}_2 + 2\text{H}_2\text{O}$ $\text{C}_3\text{H}_8 + 5\text{O}_2 = 3\text{CO}_2 + 4\text{H}_2\text{O}$

Table II. Stoichiometric reactions of methane and propane.

	Reactants				Flue gas			
	m [g]	M [g/mol]	n [mol]	O ₂ need [mol]	CO ₂ [mol]	H ₂ O [mol]	O ₂ [mol]	N ₂ [mol]
CH ₄	19.29	16.04	1.20	2.41	1.20	2.41		
C ₃ H ₈	69.85	44.10	1.59	7.94	4.76	6.35		
O ₂	369.61	32.00	11.55	-11.55				
N ₂	1237.39	28.01	44.25	0				
SUM	1696.14		58.59	-1.21	5.96	8.75		
Excess O ₂ (O ₂ from feed – O ₂ need)							1.21	
N ₂ from air (79.3/20.7·O ₂ feed)								44.25
Total					5.96	8.75	1.21	44.25
Mole fraction					0.100	0.147	0.020	0.732

APPENDIX III: PROCESS FURNACE SIMULATION RESULTS: CONTOUR PLOTS

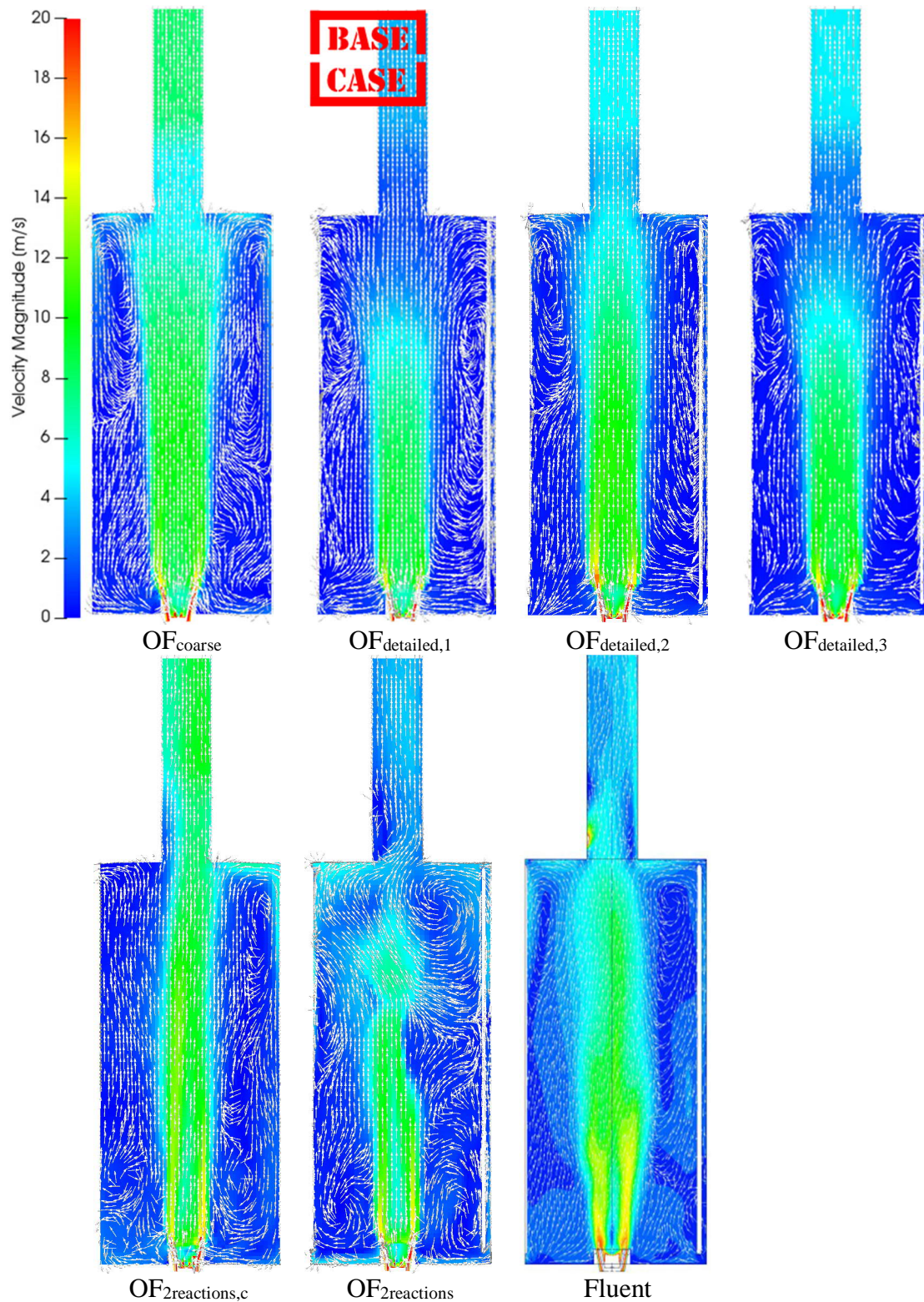


Figure 1. Average velocity (0-20 m/s) profile at Z-normal plane for OF cases and transient data for Fluent.

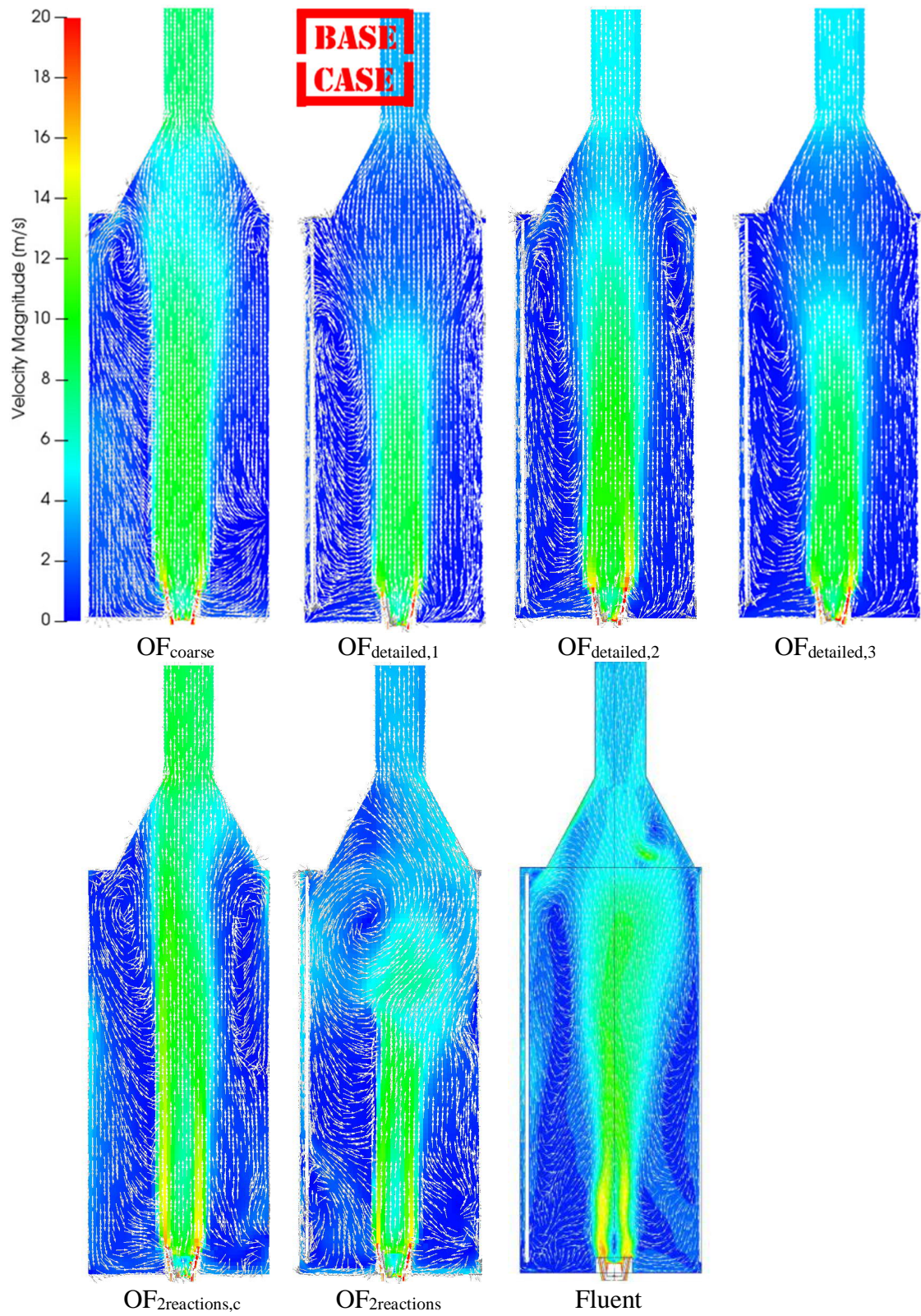


Figure 2. Average velocity (0-20 m/s) profile at X-normal plane for OF cases and transient data for Fluent.

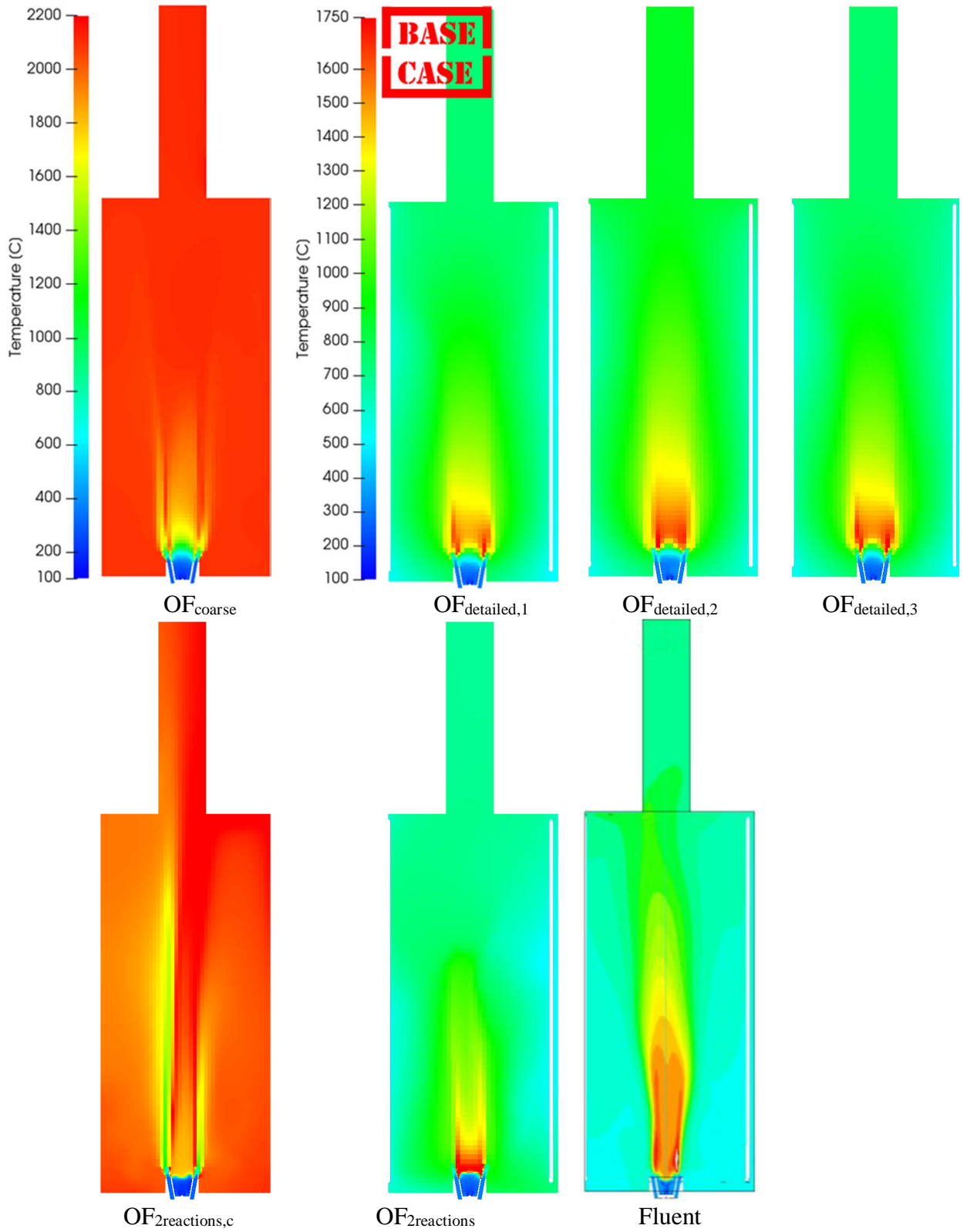


Figure 3. Average temperature (100-1750 °C) profile at Z-normal plane for OF cases and transient data for Fluent. Note the different scale for OF_{coarse} and $OF_{2reactions,c}$ (100-2200 °C).

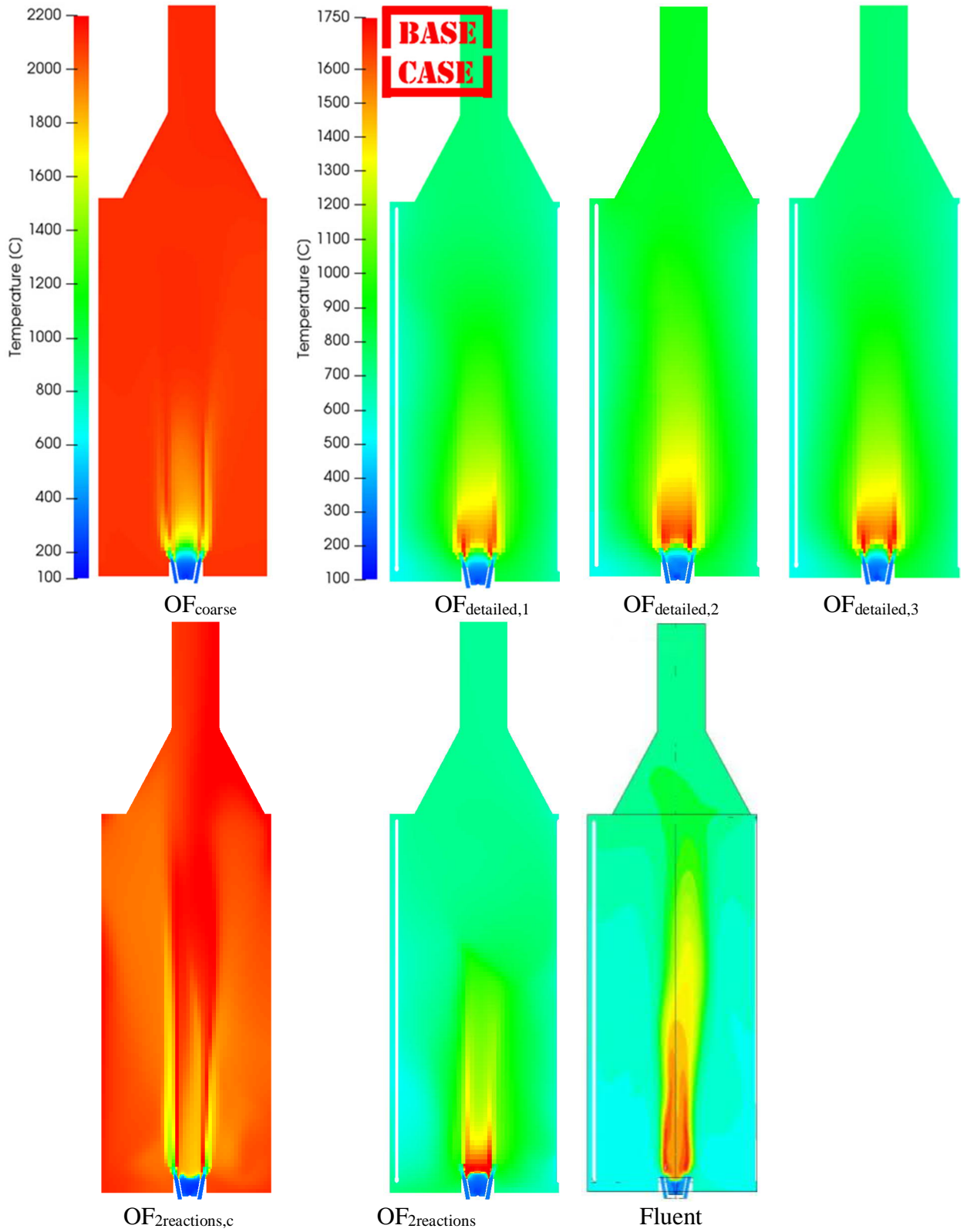


Figure 4. Average temperature (100-1750 °C) profile at X-normal plane for OF cases and transient data for Fluent. Note the different scale for OF_{coarse} and $OF_{2reactions,c}$ (100-2200 °C).

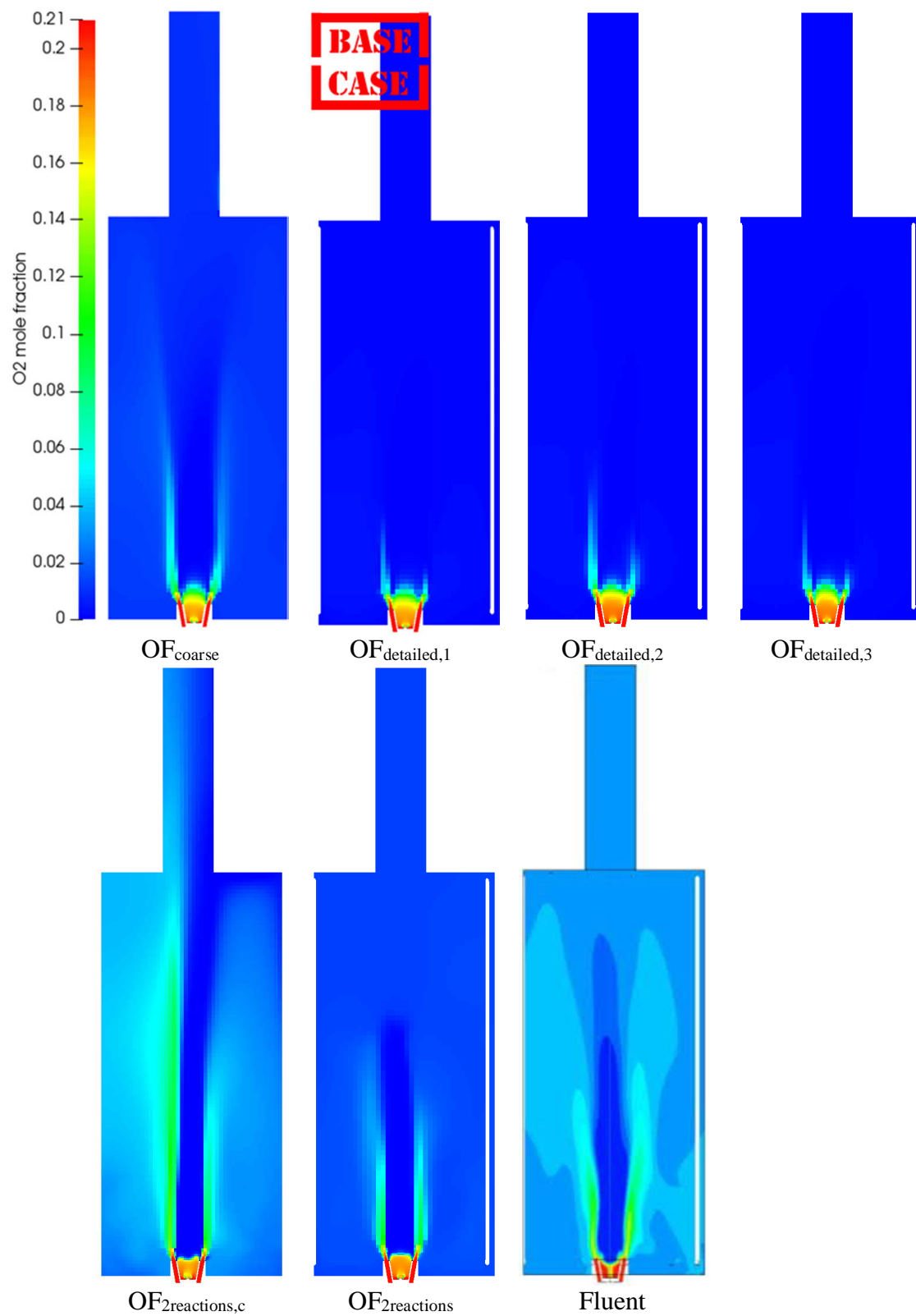


Figure 5. Average O₂ mole fraction (0-21 mol-%) field at Z-normal plane for OF cases and transient data for Fluent.

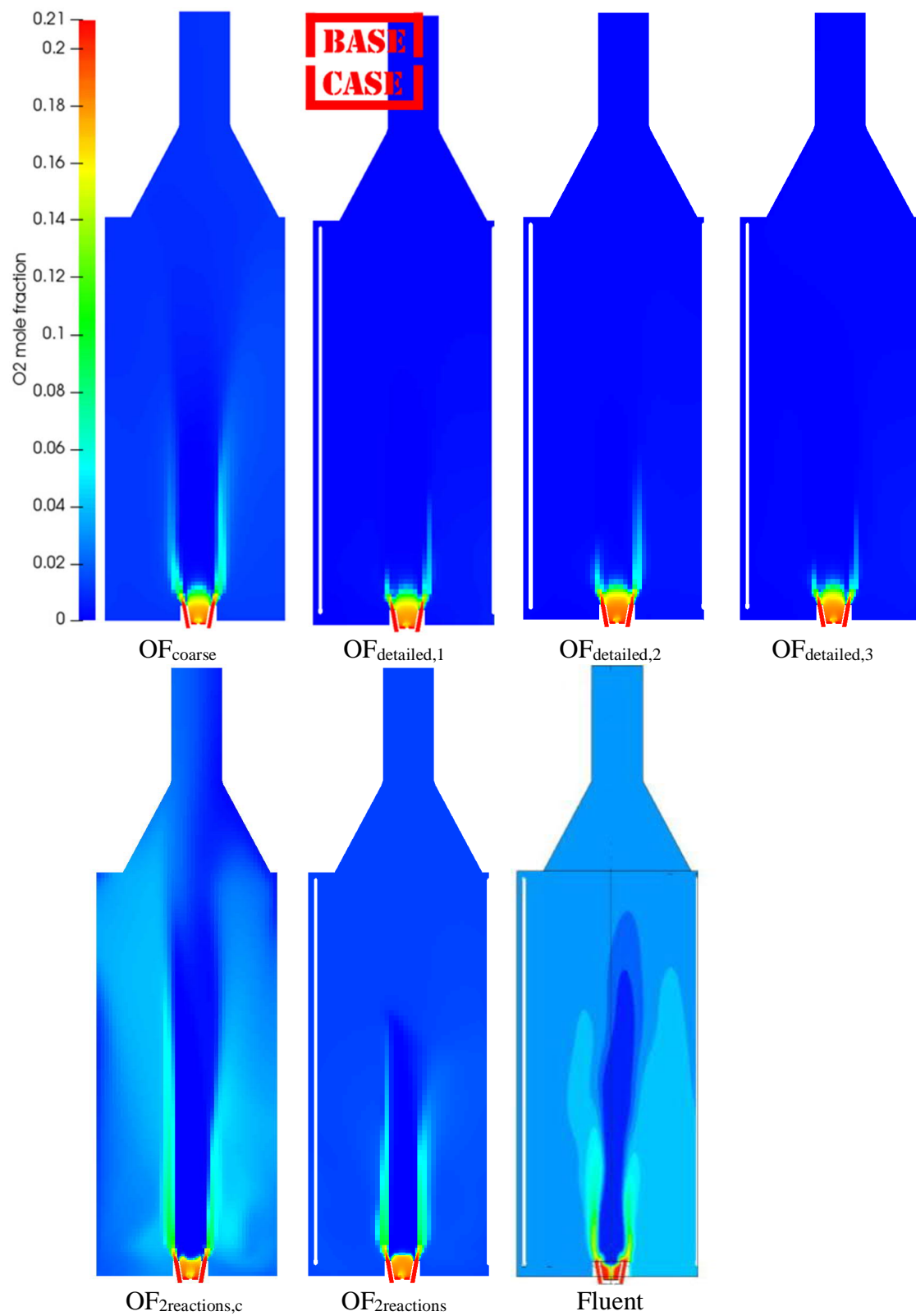


Figure 6. Average O₂ mole fraction (0-21 mol-%) field at X-normal plane for OF cases and transient data for Fluent.

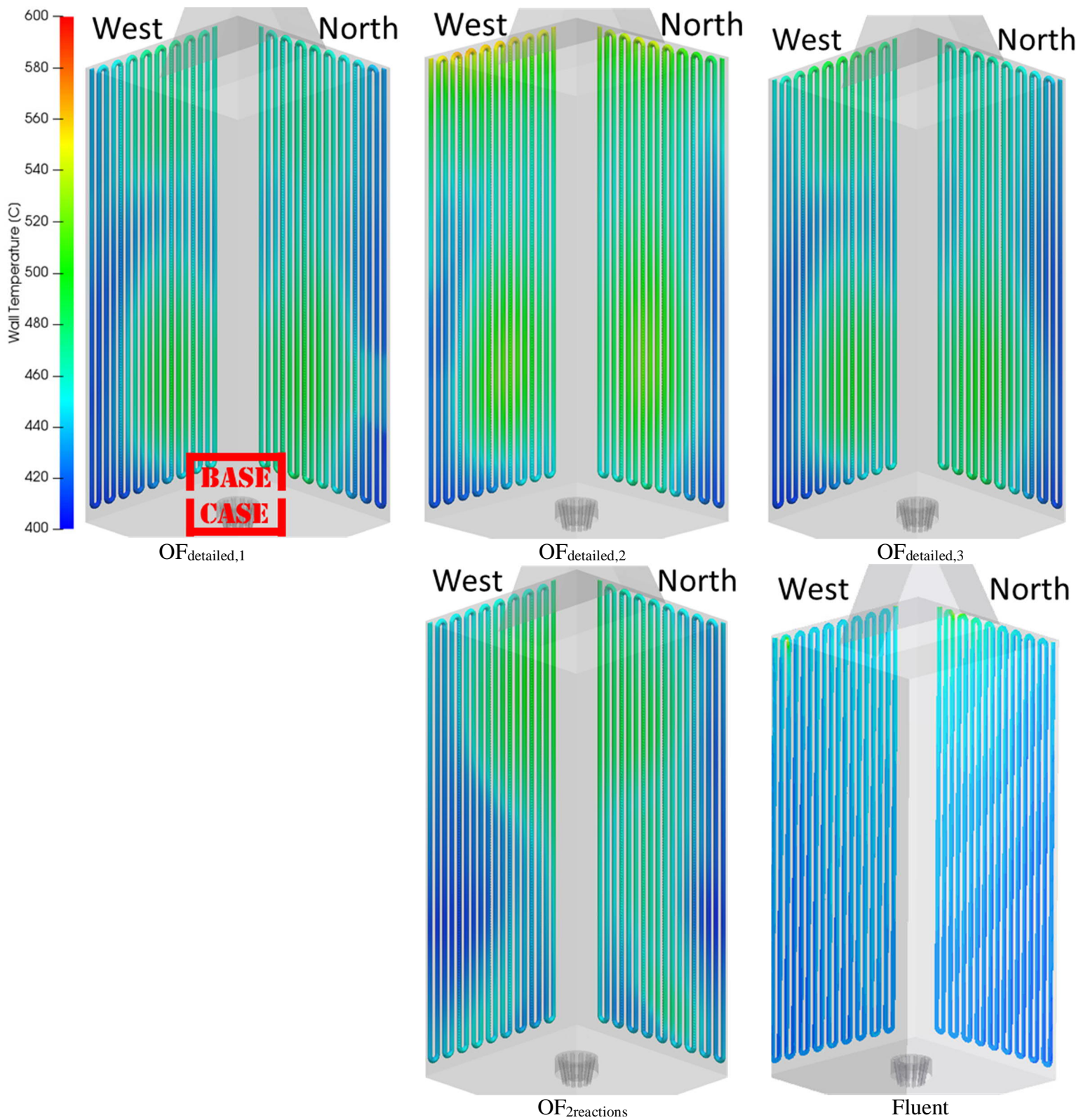


Figure 7. Average temperature (400-600 °C) profile at North and West tube bundles for OF cases and transient data for Fluent.

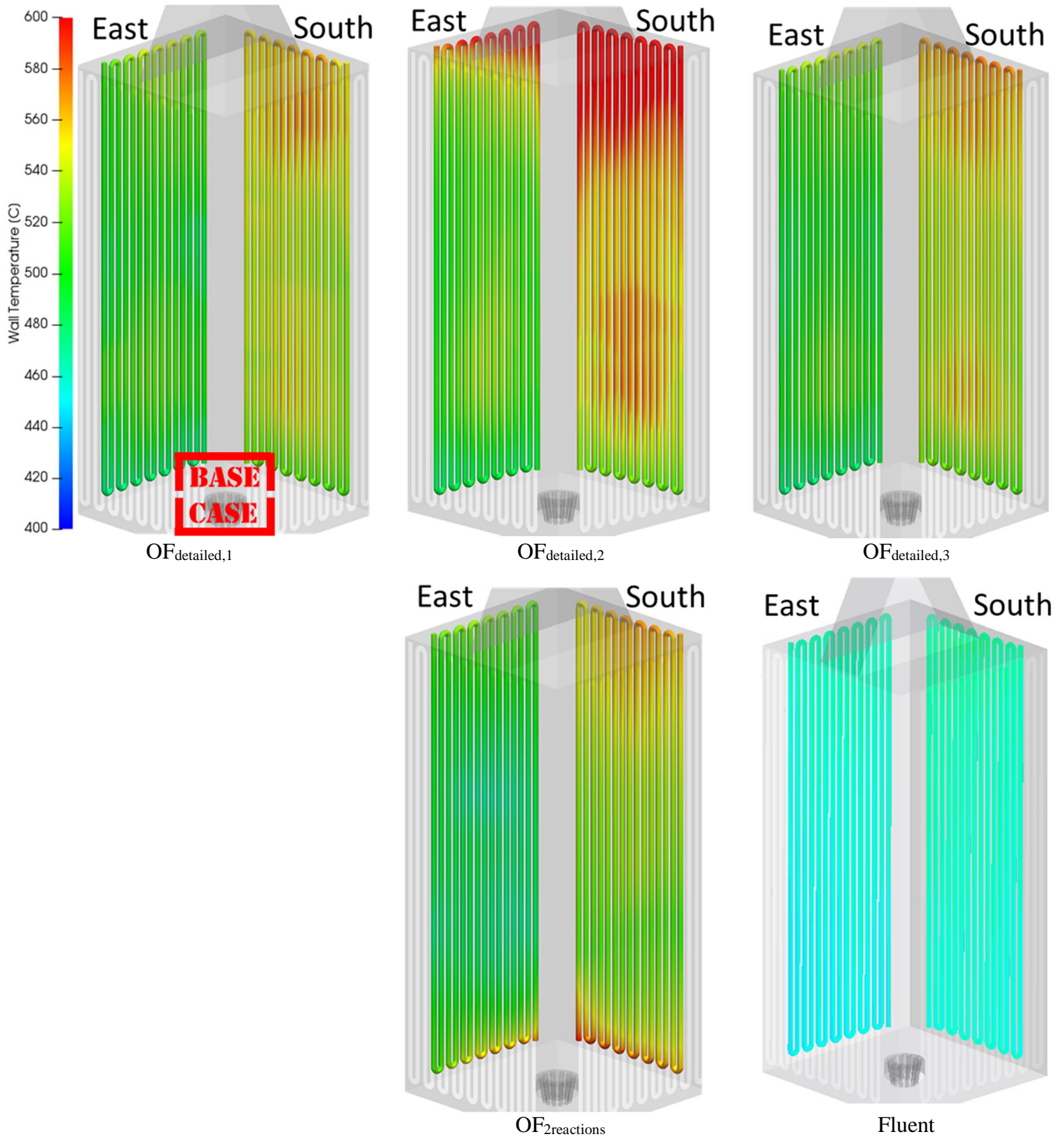


Figure 8. Average temperature (400-600 °C) profile at South and East tube bundles for OF cases and transient data for Fluent.